5-21-2004

Residual Stress Measurements of Unblasted and Sandblasted Mild Steel Specimens Using X-Ray Diffraction, Strain-Gage Hole Drilling, and Electronic Speckle Pattern Interferometry (ESPI) Hole Drilling Methods

Saskia Lestari
University of New Orleans

RESIDUAL STRESS MEASUREMENTS OF UNBLASTED AND SANDBLASTED MILD STEEL SPECIMENS USING X-RAY DIFFRACTION, STRAIN-GAGE HOLE DRILLING, AND ELECTRONIC SPECKLE PATTERN INTERFEROMETRY (ESPI) HOLE DRILLING METHODS

A Thesis

Submitted to the Graduate Faculty of the
University of New Orleans
in partial fulfillment of the
requirements for the degree of

Master of Science
in
The Department of Civil Engineering

by

Saskia Indah Lestari

B.S., University of New Orleans, 2002

May 2004

ACKNOWLEDGMENTS

I would like to express my gratitude to my thesis advisor, Dr. Norma Jean Mattei, for her continuous attention, guidance, and support during this research and the preparation of this thesis. Her confidence in my academic abilities has made this work possible. I am also very thankful for the opportunity to work with her in various projects, in addition to her constant effort in seeking financial supports for my graduate study of two years.

It would not have been possible to complete this thesis without the help and guidance of numerous people. I would like to acknowledge the advice, guidance, and assistance provided by Michael Steinzig of Hytec, Incorporated, in Los Alamos, New Mexico. Many thanks to Isaac Esparza for providing me with basic training for the strain-gage hole drilling method, as well as his assistance in my initial literature research. I wish to also thank Ryan Bright of Bartlett Engineering, in Metairie, Louisiana, for his help with specimen preparation for the strain-gage hole drilling method.

Special thanks to Dr. Paul Schilling of the Mechanical Engineering Department and his graduate assistant, Dileep Simhadri, for the use of X-ray diffractometer and their assistance in initial test setups, as well as troubleshooting of the equipment. I would also like to thank Dr. Paul Schilling, Dr. Michael Folse, and Dr. Mysore Nataraj, for their time and willingness to serve on my thesis committee.

I would like to end this by thanking those closest to me. I am grateful to all my friends in New Orleans for their continuous moral support and for their friendships. I wish to also thank my family in Vermont for their love and support throughout the years. I will never be where I am today without them. Finally, no words can express my love and greatest appreciation and gratitude to my parents and my brother, who have always put my interests before theirs. To them I dedicate this thesis.

TABLE OF CONTENTS

LIST OF TABLES

LIST OF FIGURES

ABSTRACT

The objectives of this research are to measure residual stress in both unblasted and sandblasted mild steel specimens by using three different techniques: X-ray diffraction (XRD), strain-gage hole drilling (SGHD), and electronic speckle pattern interferometry (ESPI) hole drilling, and to validate the new ESPI hole drilling method by comparing its measurement results to those produced by the SGHD method.

Both the XRD and SGHD methods were selected because they are accurate and well-verified approaches for residual stress measurements. The ESPI hole drilling technique is a new technology developed based on the SGHD technique, without the use of strain gage. This technique is incorporated into a new product referred to as the PRISM system, manufactured by Hytec, Incorporated, in Los Alamos, New Mexico.

Each method samples a different volume of material at different depths into the surface. XRD method is especially different compared to the other two methods, since XRD only measures stresses at a depth very close to the surface (virtually zero depth). For this reason, no direct comparisons can be made between XRD and SGHD, as well as between XRD and ESPI hole drilling. Therefore, direct comparisons can only be made between SGHD and ESPI hole drilling methods.

1. INTRODUCTION

Residual stresses are defined as those stresses that exist in a structural material in the absence of external forces or thermal gradients. These stresses are introduced into a component by various manufacturing and fabricating processes (i.e. casting, welding, machining, molding, heat treatment), as well as in-service repair or modification.

Residual stresses can either have beneficial or detrimental effect on a material, depending upon their magnitude, sign, and distribution. It is therefore crucial to know how much locked-in (residual) stresses exist in an object without the presence of any external loads, especially in the case where fatigue is an important concern. The total stress that exists within a body is the sum of the residual and applied load stresses [1]. Based on this knowledge, it can be concluded that compressive residual stress increases the performance capacity of a material, such as fatigue life and crack propagation, while tensile residual stress promotes fatigue failure.

Residual stress can be measured by several methods, depending on the size and material of the component to be tested, and the availability, testing speed, and cost of the equipment. Each method can be categorized as either destructive or non-destructive. Destructive methods involve the creation of a new state of stress in a material by either machining or layer removal, detection of the local change in stress by measuring the strain or displacement, and calculation of residual stress as a function of the measured strain [2]. Destructive methods include strain-gage hole drilling, ring core, bending

deflection, and sectioning. In the case of non-destructive methods, no material destruction is needed to release the energy or stress stored in it. They mainly involve the establishment of a relationship between the physical or crystallographic parameters and the residual stress. The following techniques are considered to be non-destructive: X-ray diffraction, neutron, ultrasonic, and magnetic methods.

This research compares two commonly used techniques, X-ray diffraction and strain-gage hole drilling, with one newly-developed electronic speckle pattern interferometry (ESPI) hole drilling method, to measure the residual stress in both unblasted and sandblasted mild steel specimens. The X-ray diffraction and strain-gage hole drilling methods were selected because they are industry standards, representing non-destructive and destructive techniques, respectively. The equipment used for X-ray diffraction is very expensive and many are not portable. The size of specimens to be tested by X-ray diffraction is also limited. When measuring residual stress in large quantities, the strain-gage hole drilling method is very time consuming and costly. It requires meticulous work, such as surface preparation, gage installation, and precise hole drilling. The ESPI hole drilling method can measure residual stress of a material without any surface preparation. Measurements can be done in a very short amount of time as well. Residual stress measurement results produced by the strain-gage hole drilling method are compared to those produced by the ESPI hole drilling to validate this new technology.

The first three chapters of this paper provide theoretical background and overview of each method used in this research: X-ray diffraction, strain-gage hole drilling, and electronic speckle pattern interferometry (ESPI) hole drilling. This is followed by

experimental data, which consists of equipment details and settings, as well as test parameters used in each method. The following chapter contains measurement results obtained from the three different methods, along with result comparisons. Finally, conclusions and possible future studies are presented in the last two chapters of the paper.

2. X-RAY DIFFRACTION METHOD

The X-ray diffraction method enables a nondestructive measurement of residual stress. It is applicable to crystalline materials with a relatively small (i.e. "fine") grain size. This method relies on the elastic deformations within a polycrystalline material to measure its internal stress.

2.1 BRAGG'S LAW

The fundamental equation of all X-ray diffraction measurements is Bragg's law, defined by:

$$n\lambda = 2d_{hkl}\sin\theta \qquad \text{(Eq. 2.1)}$$

where n = a whole number of the order of reflection or diffraction

λ = incident radiation wavelength

d_{hkl} = perpendicular distance between adjacent parallel crystallographic planes, defined by the Miller indices (hkl)

θ = angle of scattering usually referred to as the "Bragg angle"

A crystalline material is made up of many crystals, which are composed of atoms arranged in a three-dimensional periodic pattern. Depending on the inter-planar spacing

(d) and the incident radiation wavelength (λ), the planes of atoms can either cause constructive and/or destructive interference patterns by diffraction [3].

Incident X-ray beams must be parallel, monochromatic, and coherent (in-phase) in order for diffraction to occur. Figure 1 illustrates the diffraction of X-rays by a crystal lattice as the basic principle of the Bragg's law. An "in-phase" X-ray beam of wavelength λ is incident on the two parallel planes of atoms A-A' and B-B' at an angle θ. Rays 1 and 2 are scattered by atoms P and Q, to yield scattered rays 1' and 2' also at an angle θ to the planes. The difference in path length between the adjacent X-ray beams is some integral number (n) of radiation wavelength (λ). In other words, $\overline{SQT} = n\lambda$ for constructive interference. Further, by simple geometry,

$n\lambda = \overline{SQ} + \overline{QT} = d_{hkl}\sin\theta + d_{hkl}\sin\theta = 2d_{hkl}\sin\theta$, which yields the Bragg equation.

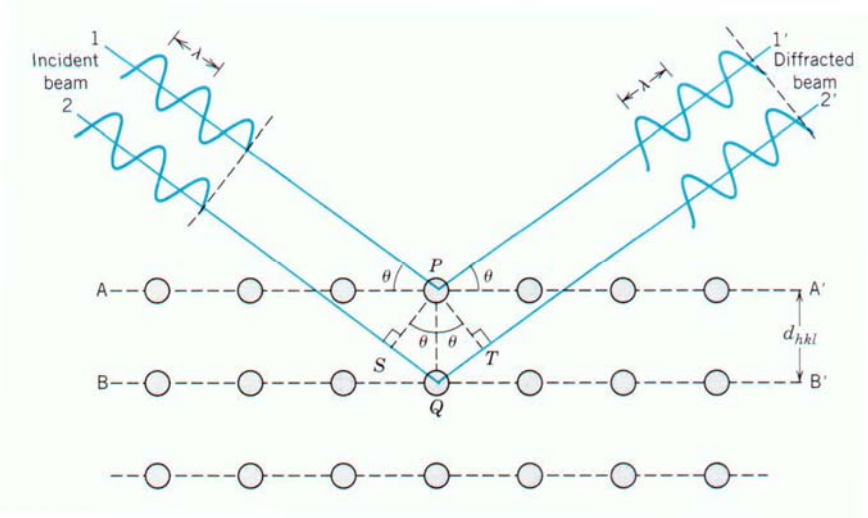

Figure 1: Diffraction of X-rays by planes of atoms A-A' and B-B' [4].

Note that the angle θ is the Bragg angle, while the angle 2θ is the diffraction angle, which is the angle measured experimentally. The relationship between the Bragg angle (θ) and the experimentally measured diffraction angle (2θ) is shown in Figure 2.

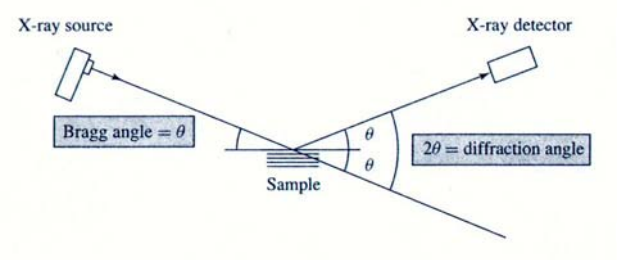

Figure 2: Relationship of θ and 2θ [5].

Destructive interference patterns occur when incident X-ray beams are not in-phase. In this case, Bragg's law is not satisfied, and therefore yields a very low-intensity diffracted beam.

Bragg's law only defines the diffraction condition for primitive unit cells, which are those space or Bravais lattices (Figure 3), with lattice points only at unit cell corners, such as simple cubic and simple tetragonal crystal structures. Nonprimitive unit cells have atoms at additional lattice sites located along a unit cell edge, within a unit cell face, or in the interior of the unit cell [5]. As a result, out-of-phase scattering may occur at certain Bragg angles and some of the diffraction predicted by the Bragg equation does not occur.

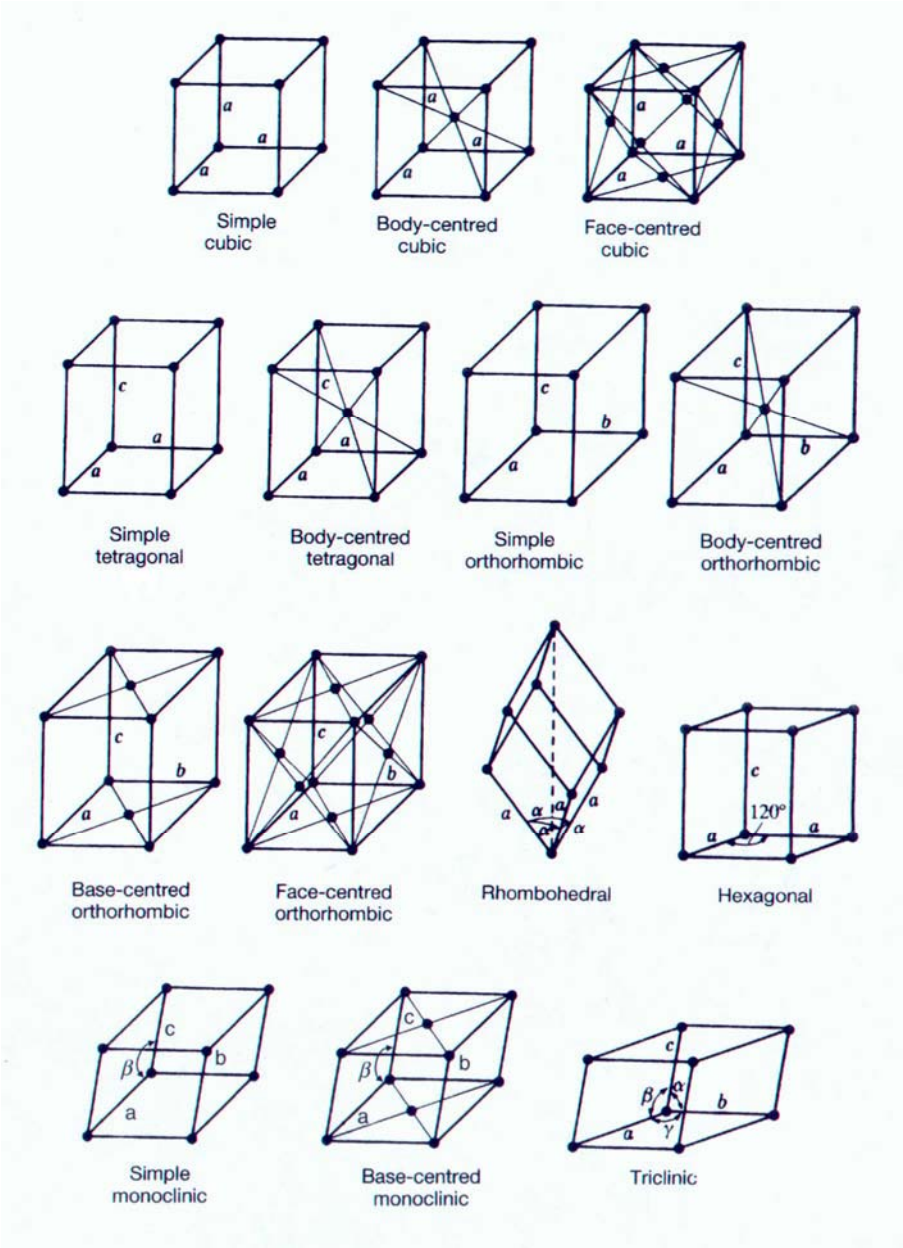

Figure 3: The fourteen Bravais lattices [6].

Table 1 lists diffraction rules for the common metal structures. It shows the Miller indices criteria for several crystal structures in order to produce diffraction, as defined by Bragg's law.

Table 1: X-ray diffraction for the common metal structures [5].

Crystal structure	Diffraction does not occur when:	Diffraction occurs when:
Body-centered cubic (bcc)	h + k + l = odd number	h + k + l = even number
Face-centered cubic (fcc)	h, k, l mixed (i.e., both even and odd numbers)	h, k, l unmixed (i.e., are all even numbers or all odd numbers)
Hexagonal close packed (hcp)	(h + 2k) = 3n, l odd (n is an integer)	all other cases

2.2 STRAIN MEASUREMENT AND STRESS DETERMINATION

Each type of strain-free material has a unique inter-planar spacing that yields a specific diffraction pattern when it is exposed to an X-ray beam. Various manufacturing and fabricating processes, as well as any external or service loads applied to a body will cause deformations within the material. These deformations alter the distance between atomic planes, which in turn cause a shift in the diffraction pattern. The X-ray diffraction technique measures this shift precisely and gives the change in spacing of the lattice planes. The strain in the crystal lattice is determined from the change in spacing.

By noting that strain ε_z and stress σ_3 are normal to the specimen surface (the z direction) and assuming that measurement is conducted within the surface (i.e. $\sigma_3 = 0$), the relationship between the inter-planar spacing and strain can be expressed mathematically as:

$$\varepsilon_z = \frac{d_n - d_0}{d_0} \qquad \text{(Eq. 2.2)}$$

If d_0 is known, the strain ε_z can be measured experimentally by determining the high angle peak 2θ and solving for d_n using the Bragg equation (Eq. 2.1). Equation 2.2 allows

strain within the surface to be measured by comparing the unstrained inter-planar spacing (d_0) to the strained inter-planar spacing (d_n), but is strictly limited to measurements taken normal to the surface.

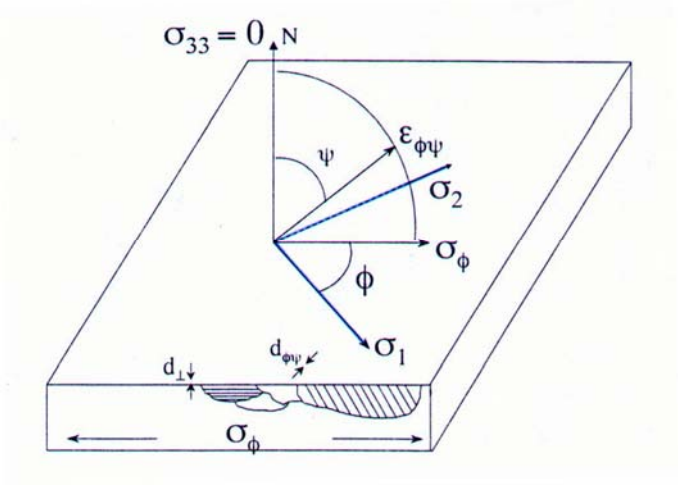

Figure 4: Diffraction planes parallel to the surface and at an angle $\phi\psi$ [3].

When a specimen is tilted at a certain angle ψ normal to the surface and/or rotated at a certain angle ϕ parallel to the surface in the X-ray diffractometer, the strains along that direction can be determined by:

$$\varepsilon_{\phi\psi} = \frac{d_\psi - d_0}{d_0} \qquad \text{(Eq. 2.3)}$$

where d_ψ is the inter-planar spacing of planes at an angle ψ to the surface. Figure 4 is a schematic showing diffraction planes parallel to the surface and at an angle $\phi\psi$, where σ_1 and σ_2 lie in the plane of the specimen surface.

Once strains within the material are known, the stresses associated with them can be determined. Based on the elasticity theory for an isotropic solid,

$$\varepsilon_{\phi\psi} = \frac{1+\upsilon}{E}\left(\sigma_1 \cos^2\phi + \sigma_2 \sin^2\phi\right)\sin^2\psi - \frac{\upsilon}{E}\left(\sigma_1 + \sigma_2\right) \qquad \text{(Eq. 2.4)}$$

where E is the Young's modulus of elasticity and υ is the Poisson's ratio of the material.

In order to calculate stress in any chosen direction from the inter-planar spacings determined in a plane normal to the surface and in the direction of the stress to be measured, strains are considered in terms of inter-planar spacing and they are used to evaluate the stresses to yield:

$$\sigma_\phi = \frac{E}{(1+\upsilon)\sin^2\psi}\left(\frac{d_\psi - d_n}{d_n}\right) \qquad \text{(Eq. 2.5)}$$

σ_ϕ is a single stress acting in a chosen direction (i.e. at an angle ϕ to σ_1).

There are several experimental methods to evaluate the stresses within a crystalline material, including:

a. Two-exposure method
b. Parallel-beam method
c. $\text{Sin}^2\psi$ method
d. Side-inclination method
e. Variant of the two-exposure method, where the inclined measurement is made at $\psi = 60°$ rather than at 45° [7].

The $\text{Sin}^2\psi$ method is the most commonly used. Using this method, measurements are made at a number of different ψ tilts. At each ψ angle tilt, the inter-planar spacing is measured. Once measurements are obtained from all ψ tilts, a curve of inter-planar spacing (d) versus $\sin^2\psi$ is then plotted. The value of stress (σ_ϕ) can then be determined

by obtaining the gradient of the line or elliptical fit, and incorporating the elastic properties of the material.

Assuming zero stress at $d = d_n$, the stress is given by:

$$\sigma_\phi = \left(\frac{E}{1+\upsilon}\right)m \qquad \text{(Eq. 2.6)}$$

where m is the gradient of the d versus $\sin^2\psi$ curve. Equation 2.6 applies only in an ideal situation, where there is no shear stress present and the stress state within the material is isotropic. Under these conditions, the curve of d versus $\sin^2\psi$ is linear.

In the case where shear stresses are present, "ψ splitting" occurs. The curve of d versus $\sin^2\psi$ becomes elliptical in shape, with two branches; one corresponds to positive values of ψ and the other to negative values of ψ. When the stress/strain state within the material is anisotropic, the curve of d versus $\sin^2\psi$ becomes oscillatory.

2.3 CHOICE OF X-RAY TUBE ANODE

The choice of an X-ray tube is critical for the measurement of residual stress. In order to precisely measure the inter-planar spacing (d) within a crystalline material, one has to select an anode material which gives a suitable Bragg reflection at a sufficiently high 2θ angle. A radiation is not suitable for a particular kind of crystalline material when the K-α_1 component of the incident beam causes the atoms in the sample to absorb that energy, and then causes it to produce its own fluorescent X-rays. Fluorescence causes a very high background and a poor peak-to-background ratio for the resultant data. If this occurs, it can be improved by using a secondary monochromator or by collecting the data over a longer period of time.

All samples tested in this research were mild steel, while the X-ray tube anode used was copper. A chromium anode would have been a better choice of X-ray tube for mild steel, but was not available for these measurements. A chromium anode has a longer wavelength compared to copper. As a result, its radiation does not have sufficient energy to cause fluorescence. The less energetic chromium anode also penetrates further into the material compared to the more energetic copper anode. In addition, the planes used for diffraction are different when a chromium anode is used instead of copper [3].

Regardless of the type of anode chosen, it is critical to measure the stress using a high 2θ angle – generally greater than 130°. This is because the changes in the *d*-spacing due to stress are very small, so the greater the value of θ, the less error in the peak positioning, as governed by the equation:

$$\frac{\Delta d}{d} = -\Delta\theta \cot\theta \qquad \text{(Eq. 2.7)}$$

Table 2 shows recommended test parameters for two common steels, as provided by Tony Fry of the National Physical Laboratory in Middlesex, UK. Note that the test parameters are not the same when using different types of anode on the same material.

Table 2: Recommended test parameters for two common steels [8].

Material	Radiation	Wavelength (Å)	Filter	Peak Plane {hkl}	Peak 2θ Angle (degrees)	Penetration Depth $\langle \sin^2\psi = 0.3 \rangle$ (μm)
b.c.c. iron, ferrite & martensite of iron base materials	Cr-Kα	2.289649	V	{211}	156.07	4.6 - 4.7
	Cu-Kα	1.540501	Monochrom.	{222}	137.13	1.5 - 1.6
f.c.c. iron, retained austenite and austenitic base materials	Cr-Kα	2.289649	V	{220}	128.84	3.9 - 4.3
	Cu-Kα	1.540501	Monochrom.	{331}	138.53	1.5 - 1.9

2.4 MEASUREMENT PARAMETERS

In order to record diffraction peak in the minimum time possible, generally the X-ray tube should be operated at its maximum recommended power output. Power settings should be kept the same for all measurements done for comparison studies. Otherwise, results will be obtained at different depths below the sample surface. Count time selected should be long enough to ensure that a well-defined peak is obtained. It is determined based on the tube and sample characteristics, surface preparation, presence of K-β filter, as well as the presence of apertures in the incoming or diffracted beam paths. According to Fitzpatrick et. al [3], doubling the count time improves the counting statistics of each point in the peak by a factor of $\sqrt{2}$.

Step size is generally selected in the range of 0.05° to 0.2°. The smaller the step size, the longer it takes to acquire the peak. However, a smaller step size will give a more accurate final peak fit. Another measurement parameter to be selected is the number of tilt angles (ψ). It is recommended to have at least 5 tilts for both positive and negative ψ angles. If a particular crystalline material does not produce intense peaks, increasing the number of ψ angle tilts will also improve the accuracy of the final stress calculation [3].

2.5 POSSIBLE SOURCES OF MEASUREMENT UNCERTAINTY

Several factors that may create uncertainty in a residual stress measurement by X-ray diffraction method include: elastic constants, instrument alignment, specimen-surface height offset, 2θ step size, number of angle ψ tilts, counting time, specimen surface

condition, and operator competence [9]. A study by François, et al. [10] also shows that the software used to localize the peaks and calculate stress is another variable which can contribute to the measurement uncertainty of X-ray diffraction.

It is important to distinguish the term “error” from the term “uncertainty”. Error is the difference between a computed or measured value and a true or theoretically correct value, while uncertainty is the estimated amount or percentage by which an observed or calculated value may differ from the true value.

2.6 ADVANTAGES AND DISADVANTAGES OF METHOD

X-ray diffraction is one of the most commonly used methods for residual stress measurement. It is a nondestructive technique to evaluate surface residual stress. However, when combined with the layer removal method in order to generate a stress profile, the method becomes destructive. The measurement time depends on the type of material of the sample, type of X-ray radiation, and the degree of accuracy required. In addition to new detector technology, appropriate selection of the X-ray anode and test settings will greatly reduce the measurement time. Other advantages also include its versatility, capability to analyze a wide range of materials, and availability of portable systems.

One of the major disadvantages of this method is that the size and geometry of the test piece are limited. The sample has to be small enough to fit into the diffractometer and has to be such that the incident beam can hit the measurement area on the sample, and still be diffracted to the detector without hitting any obstructions. Rough surface conditions also cause problems.

3. STRAIN-GAGE HOLE DRILLING METHOD

Another popular method to measure residual stress is the strain-gage hole drilling method. It involves localized removal of stressed material and measurement of strain relief in the adjacent material using strain gages. The strain-gage hole drilling method is considered to be a destructive technique because it involves the introduction of a hole into the test part. In large or thick parts, this method may be considered semi-destructive, since the small hole introduced into the sample generally will not significantly impair the structural integrity of the part being tested.

3.1 PRINCIPLES AND THEORY

The introduction of a hole into a component containing residual stresses causes the surface strains to be relieved locally. The corresponding residual stress within the material can then be calculated from these relieved strains using formulas derived from experimental and finite element analyses [7]. There are two different applications of the strain-gage hole drilling method: through-hole and blind-hole analyses. The theoretical basis for the hole drilling method applies to the through-hole analysis, which assumes that a small hole is drilled completely through a thin, wide, flat plate, subjected to uniform plane stress. However, most practical applications involve the blind-hole method, which involves drilling a hole with a depth about equal to its diameter and small

compared to the thickness of the test object. Blind hole analysis is based on the through-hole analysis [11].

3.1.1 Through-Hole Analysis

Consider a thin plate with a local area subjected to a uniform residual stress, σ_x, as shown by Figure 5a. The state of stress at any point P (expressed in polar coordinates) is:

$$\sigma_r' = \frac{\sigma_x}{2}(1+\cos 2\alpha) \qquad \text{(Eq. 3.1a)}$$

$$\sigma_\theta' = \frac{\sigma_x}{2}(1-\cos 2\alpha) \qquad \text{(Eq. 3.1b)}$$

$$\tau_{r\theta}' = -\frac{\sigma_x}{2}\sin 2\alpha \qquad \text{(Eq. 3.1c)}$$

Once a small hole is drilled through it, the state of stress at point P becomes:

$$\sigma_r'' = \frac{\sigma_x}{2}\left(1-\frac{1}{r^2}\right)+\frac{\sigma_x}{2}\left(1+\frac{3}{r^4}-\frac{4}{r^2}\right)\cos 2\alpha \qquad \text{(Eq. 3.2a)}$$

$$\sigma_\theta'' = \frac{\sigma_x}{2}\left(1+\frac{1}{r^2}\right)-\frac{\sigma_x}{2}\left(1+\frac{3}{r^4}\right)\cos 2\alpha \qquad \text{(Eq. 3.2b)}$$

$$\tau_{r\theta}'' = -\frac{\sigma_x}{2}\left(1-\frac{3}{r^4}+\frac{2}{r^2}\right)\sin 2\alpha \qquad \text{(Eq. 3.2c)}$$

where $r = \frac{R}{R_0}$ and $R \geq R_0$. R_0 is the hole radius, while R is the arbitrary radius from hole center [11].

Figure 5a and 5b are illustrations of state of stress at point P before and after the introduction of the hole.

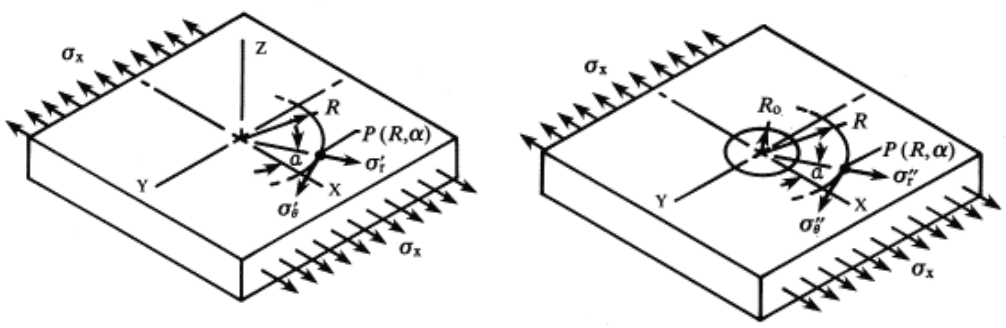

Figure 5a, b: State of stress at point P before and after the introduction of a hole [11].

The stress relaxation or change in stress at point P due to the hole drilling can be expressed as:

$$\Delta\sigma_r = \sigma_r^{''} - \sigma_r^{'} \qquad \text{(Eq. 3.3a)}$$

$$\Delta\sigma_\theta = \sigma_\theta^{''} - \sigma_\theta^{'} \qquad \text{(Eq. 3.3b)}$$

$$\Delta\tau_{r\theta} = \tau_{r\theta}^{''} - \tau_{r\theta}^{'} \qquad \text{(Eq. 3.3c)}$$

By assuming that the plate is homogeneous and isotropic, and that its stress/strain behavior is linear-elastic, the above equations can then be substituted into the biaxial Hooke's law [11] to yield the following expressions:

$$\varepsilon_r = -\frac{\sigma_x(1+\upsilon)}{2E}\left[\frac{1}{r^2} - \frac{3}{r^4}\cos 2\alpha + \frac{4}{r^2(1+\upsilon)}\cos 2\alpha\right] \qquad \text{(Eq. 3.4a)}$$

$$\varepsilon_\theta = -\frac{\sigma_x(1+\upsilon)}{2E}\left[-\frac{1}{r^2} + \frac{3}{r^4}\cos 2\alpha - \frac{4\upsilon}{r^2(1+\upsilon)}\cos 2\alpha\right] \qquad \text{(Eq. 3.4b)}$$

Further, knowing in mind that the relieved radial and tangential strains vary in a sinusoidal manner at any radius *R*, Equations 3.4 can be written in a simpler form:

$$\varepsilon_r = \sigma_x(A + B\cos 2\alpha) \qquad \text{(Eq. 3.5a)}$$

$$\varepsilon_\theta = \sigma_x(-A + C\cos 2\alpha) \qquad \text{(Eq. 3.5b)}$$

where the coefficients *A*, *B*, and *C* can be defined as:

$$A = -\frac{1+\upsilon}{2E}\left(\frac{1}{r^2}\right) \qquad \text{(Eq. 3.6a)}$$

$$B = -\frac{1+\upsilon}{2E}\left[\left(\frac{4}{1+\upsilon}\right)\frac{1}{r^2} - \frac{3}{r^4}\right] \qquad \text{(Eq. 3.6b)}$$

$$C = -\frac{1+\upsilon}{2E}\left[-\left(\frac{4\upsilon}{1+\upsilon}\right)\frac{1}{r^2} + \frac{3}{r^4}\right] \qquad \text{(Eq. 3.6c)}$$

The equations above apply to a case of uniaxial residual stress. For biaxial residual stress, one can perform the above calculations again (but this time in the Y direction), and then apply the superposition principle. Therefore, when both residual stresses are present, the relieved radial strain due to plane biaxial residual stress becomes:

$$\varepsilon_r = \sigma_x\left(A + B\cos 2\alpha\right) + \sigma_y\left(A - B\cos 2\alpha\right) = A\left(\sigma_x + \sigma_y\right) + B\left(\sigma_x - \sigma_y\right)\cos 2\alpha \qquad \text{(Eq. 3.7)}$$

To obtain the principal stresses and the angle α, three independent measurements of radial strain are acquired. As mentioned earlier, the hole drilling method uses a strain gage rosette to measure the strain relief caused by the removal of the stressed material originally in the hole. Figure 6 is an illustration of a strain gage rosette arrangement, where three radially oriented strain gages are located with their centers at the radius *R* from the center of the hole.

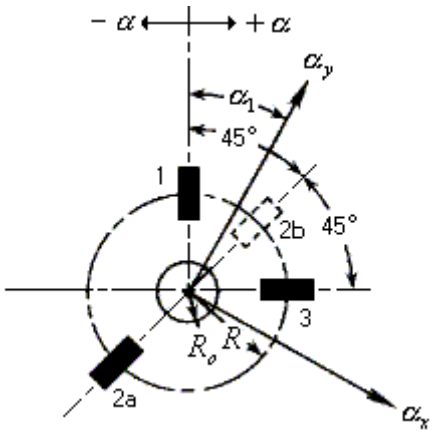

Figure 6: Strain gage rosette arrangement to determine residual stress [11].

Based on the gage orientation shown above, the strain for each gage in the rosette is:

$$\varepsilon_1 = A(\sigma_x + \sigma_y) + B(\sigma_x - \sigma_y)\cos 2\alpha \qquad \text{(Eq. 3.8a)}$$

$$\varepsilon_2 = A(\sigma_x + \sigma_y) + B(\sigma_x - \sigma_y)\cos 2(\alpha + 45^\circ) \qquad \text{(Eq. 3.8b)}$$

$$\varepsilon_3 = A(\sigma_x + \sigma_y) + B(\sigma_x - \sigma_y)\cos 2(\alpha + 90^\circ) \qquad \text{(Eq. 3.8c)}$$

The principal stresses and their direction can then be calculated using the following equations:

$$\sigma_{\max} = \frac{\varepsilon_1 + \varepsilon_3}{4A} - \frac{1}{4B}\sqrt{(\varepsilon_3 - \varepsilon_1)^2 + (\varepsilon_3 + \varepsilon_1 - 2\varepsilon_2)^2} \qquad \text{(Eq. 3.9a)}$$

$$\sigma_{\min} = \frac{\varepsilon_1 + \varepsilon_3}{4A} + \frac{1}{4B}\sqrt{(\varepsilon_3 - \varepsilon_1)^2 + (\varepsilon_3 + \varepsilon_1 - 2\varepsilon_2)^2} \qquad \text{(Eq. 3.9b)}$$

$$\tan 2\alpha = \frac{\varepsilon_1 - 2\varepsilon_2 + \varepsilon_3}{\varepsilon_3 - \varepsilon_1} \qquad \text{(Eq. 3.9c)}$$

Note that the coefficients *A* and *B* as defined in Equations 3.6, gives solution of stress distribution at points with polar coordinates *(r,α)* around a circular hole through a thin, wide plate, subjected to uniform plane stress. In reality, each gage in the rosette tends to

give results of the average strain over the grid area. To account for the finite strain gage area, more accurate *A* and *B* coefficients designated by the symbols $\overline{A}$ and $\overline{B}$, can be obtained by integrating Equations 3.4 over the areas of the respective gage grids.

3.1.2 Blind-Hole Analysis

The blind-hole analysis is an extension of the through-hole analysis. This application was developed because in practice, test objects are generally not thin, wide, flat plates subjected to uniform plane stress, as assumed by the through-hole analysis.

The main difference between the two analyses are in the definition of coefficients $\overline{A}$ and $\overline{B}$. In the blind-hole analysis, each coefficient is a function of *E*, υ, *r*, and an additional coefficient, *Z/D*. The coefficient *Z* is the depth of the shallow (blind) hole and *D* is the gage circle diameter. According to ASTM E837 [12], which is the standard for determining residual stress by the strain-gage hole drilling method, the maximum hole depth is *Z/D* = 0.4.

Based on the definition of coefficients $\overline{A}$ and $\overline{B}$ described above, it is apparent that each coefficient is materially and geometrically dependent. Schajer [13] proposed two new coefficients, $\overline{a}$ and $\overline{b}$, in order to be able to eliminate the material dependency from $\overline{A}$ and $\overline{B}$ coefficients, as defined below:

$$\overline{a} = -\frac{2E\overline{A}}{1+\upsilon} \qquad \text{(Eq. 3.10a)}$$

$$\overline{b} = -2E\overline{B} \qquad \text{(Eq. 3.10b)}$$

Thus, the coefficients $\overline{A}$ and $\overline{B}$ can be calculated if the material properties (E and υ) are known, as well as $\overline{a}$ and $\overline{b}$. The $\overline{a}$ and $\overline{b}$ coefficients for many engineering materials have been determined. Listings for these coefficients are available in Ref. 11, and are dependent on the strain gage rosette used for the measurement, as well as diameter and depth of drilled hole.

3.2 COEFFICIENTS FOR MICRO-MEASUREMENTS RESIDUAL STRESS ROSETTES

Vishay Micro-Measurements offers an extensive range of products for precision measurement of mechanical strains, including bondable strain gages, installation accessories, and instrumentation. There are three basic strain gage rosette configurations produced by Micro-Measurements: EA-XX-062RE-120, CEA-XX-062UL-120, and CEA-XX-062UM-120. Each configuration is shown respectively on Figures 7 below:

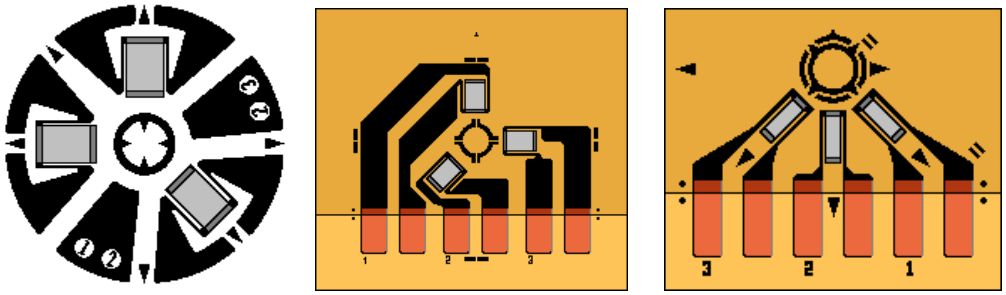

Figure 7a, b, c: Micro-Measurements residual stress strain gage rosettes [11].

The RE rosette design is the basic strain gage configuration. The prefix 'CEA' of the UL and UM rosette designs indicates the presence of copper tabs that allow easier soldering of leads. For the UM rosette design, all grids are located on one side. This geometry allows the hole to be positioned closer to welds and other irregularities. All RE and UL

rosette designs have geometrically similar grid configurations, and therefore both designs have the same material-independent coefficients $\bar{a}$ and $\bar{b}$.

3.2.1 Uniform Residual Stress Calculation

The $\bar{a}$ and $\bar{b}$ coefficients for the RE-, UL-, and UM-type rosettes can be determined graphically in Figures 8 based on the value of D_o/D, where D_o is the hole diameter and D is the is the gage circle diameter. Figure 8a is for types RE- and UL-rosette, while Figure 8b is for type UM-rosette. In each figure below, the solid lines apply to full-depth blind holes, while the dashed lines apply to through holes.

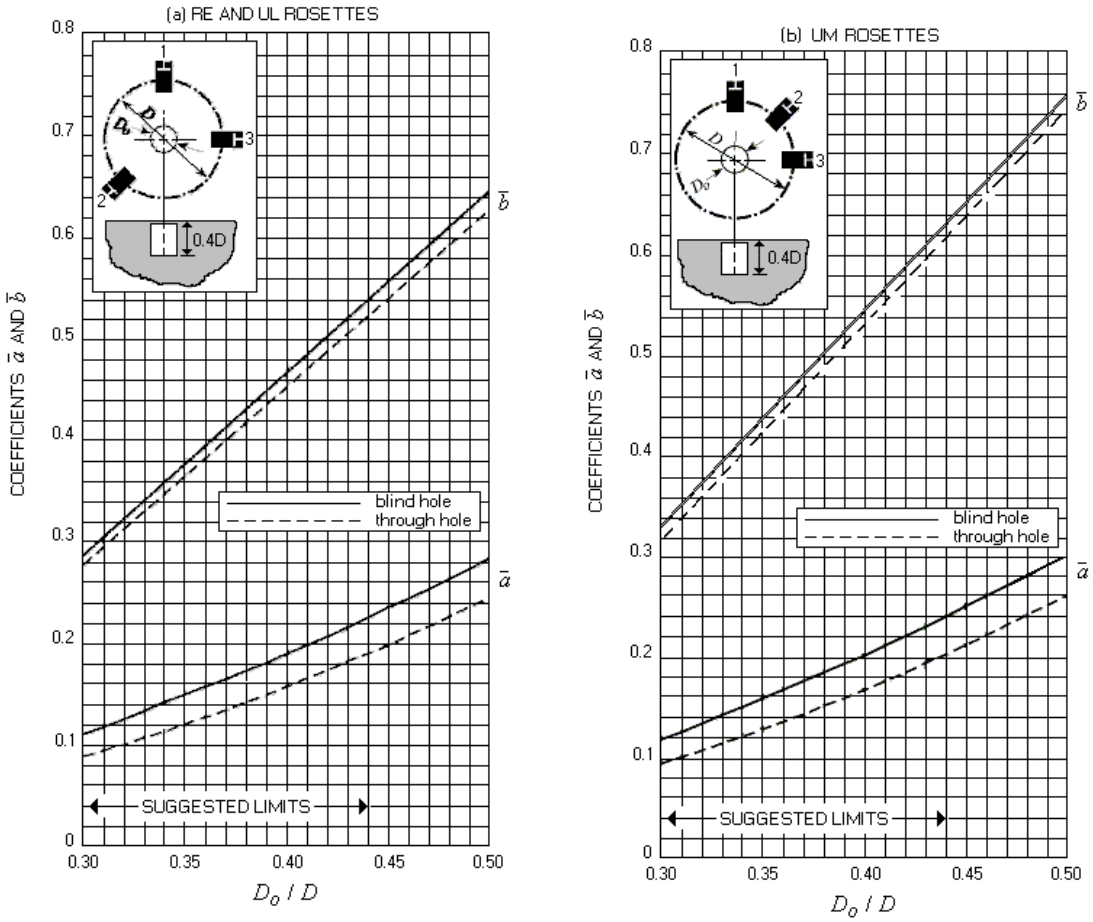

Figure 8a, b: Data-reduction coefficients $\bar{a}$ and $\bar{b}$ versus D_o/D for Measurements Group residual stress rosettes [11].

Note that Figures 8 can only be used when the initial residual stress is uniform with depth.

3.2.2 Non-Uniform Residual Stress Calculation

In the case where the residual stress varies with depth, the stresses at each partial depth can be calculated by one of the following methods:

- Integral Method
- Power Series Method
- Incremental Stress Method
- Equivalent Uniform Stress (EUS) Method

The Integral and Equivalent Uniform Stress analysis methods are within the scope of this study. The Integral method uses finite element calibrations and is recommended for highly non-uniform stress fields, such as those that exist in sandblasted specimens [14, 15, 16]. It assumes uniform stress within each hole depth increment. The EUS method uses experimental calibrations, and is an approximate. It produces the same total strain relief within the total hole depth as the actual non-uniform stress distribution [17].

For the Equivalent Uniform Stress method, the coefficients $\bar{a}$ and $\bar{b}$ can be determined from Figures 9 based on the values of Z/D and D_o/D.

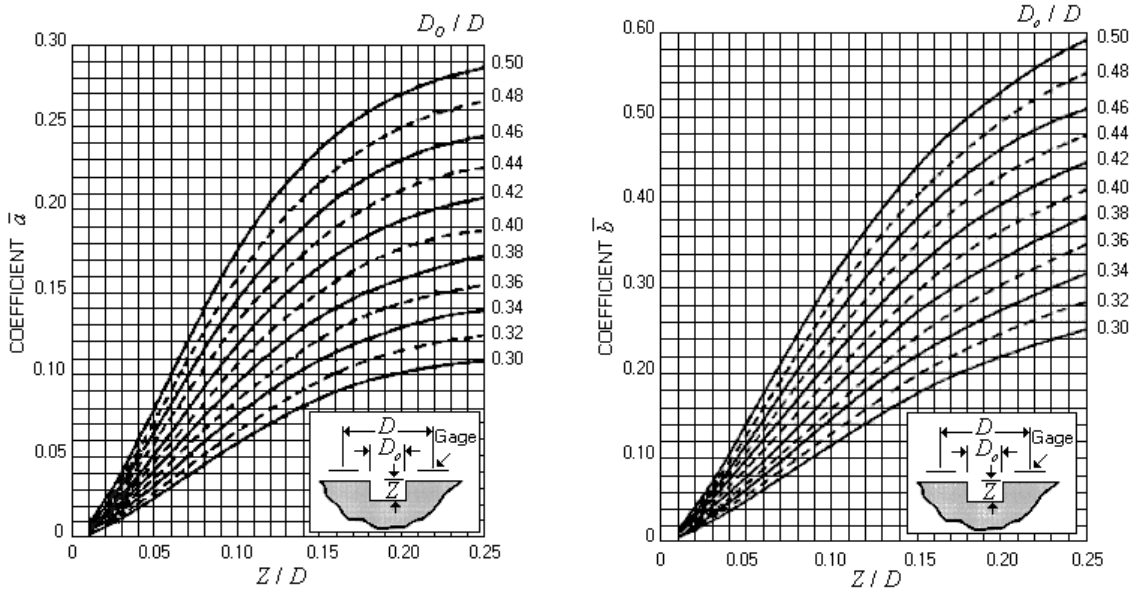

Figure 9a, b: Data-reduction coefficients $\bar{a}$ and $\bar{b}$ as functions of *Z/D* and D_o/D for RE and UL rosettes [11].

For the Integral method, the total measured strain is the sum of the relieved strains which originally exist within each of the hole depth increments, as expressed by the following equation:

$$p_i = \frac{1+\upsilon}{E}\sum_{j=1}^{j=i}\bar{a}_{ij}P_j \text{ , where } 1 \le j \le i \qquad \text{(Eq. 3.11)}$$

For an isotropic material, *p* is the "hydrostatic" component of strain measured after "*i*" hole depth increments have been drilled, defined by:

$$p = \frac{(\varepsilon_3 + \varepsilon_1)}{2} \text{ for rectangular rosette} \qquad \text{(Eq. 3.12a)}$$

$$p = \frac{(\varepsilon_1 + \varepsilon_2 - \varepsilon_3)}{3} \text{ for delta strain gage rosette} \qquad \text{(Eq. 3.12b)}$$

While *P* is the "hydrostatic" component of stress existing within hole depth increment "*j*", defined by:

$$P = \frac{(\sigma_y + \sigma_x)}{2} \qquad \text{(Eq. 3.13)}$$

The calibration constant $\bar{a}_{ij}$ that relates the stress and strain components can be determined by:

$$\bar{a}_{ij} = \hat{a}(H_j, h_i) - \hat{a}(H_{j-1}, h_i) \qquad \text{(Eq. 3.14)}$$

where h_i is the total depth of the hole, and H_{j-1} and H_j are the depths at upper and lower boundaries of that particular hole depth increment. The values of $\hat{a}(H, h)$ for the RE-, UL-, and UM-type rosettes are tabulated in Ref. 19, page 16. The required (*H, h*) combinations can then be determined using bivariate interpolation [19].

For simplification, Equation 3.11 can be expressed in matrix format as:

$$p = \frac{1+\upsilon}{E} \bar{a} P \qquad \text{(Eq. 3.15)}$$

Similar equations also exist for the other stress and strain components – shear strain 45° to gage 1 axis (q_i), shear strain along gage 1 axis (t_i), shear stress to gage 1 axis (Q_j), and shear stress along gage 1 axis (T_j), where

$$q = \frac{(\varepsilon_3 - \varepsilon_1)}{2} \text{ for rectangular rosette} \qquad \text{(Eq. 3.16a)}$$

$$q = \frac{(\varepsilon_2 + \varepsilon_3 - 2\varepsilon_1)}{3} \text{ for delta strain gage rosette} \qquad \text{(Eq. 3.16b)}$$

$$t = \frac{(\varepsilon_3 + \varepsilon_1 - 2\varepsilon_2)}{2} \text{ for rectangular rosette} \qquad \text{(Eq. 3.17a)}$$

$$t = \frac{(\varepsilon_3 - \varepsilon_2)}{\sqrt{3}} \text{ for delta strain gage rosette} \qquad \text{(Eq. 3.17b)}$$

$$Q = \frac{\left(\sigma_y - \sigma_x\right)}{2} \qquad \text{(Eq. 3.18)}$$

$$T = \frac{\tau_{xy}}{2} \qquad \text{(Eq. 3.19)}$$

Further, *q* and *t* can be expressed in matrix formats as follow:

$$q = \frac{1}{E}\bar{b}Q \qquad \text{(Eq. 3.20)}$$

$$t = \frac{1}{E}\bar{b}T \qquad \text{(Eq. 3.21)}$$

Also similar to the calibration constant $\bar{a}_{ij}$, $\bar{b}_{ij}$ can be determined by:

$$\bar{b}_{ij} = \hat{b}\left(H_j, h_i\right) - \hat{b}\left(H_{j-1}, h_i\right) \qquad \text{(Eq. 3.22)}$$

The values of $\hat{b}\left(H, h\right)$ for the RE-, UL-, and UM-type rosettes are tabulated in Ref. 19, page 16. The required (*H*, *h*) combinations can also be determined using bivariate interpolation, as described in Ref. 19. To better understand the definition of the calibration constants, Figure 10 shows a schematic representation of the coefficient $\bar{a}_{ij}$. The calibration constant $\bar{b}_{ij}$ have similar definition as the calibration constant $\bar{a}_{ij}$.

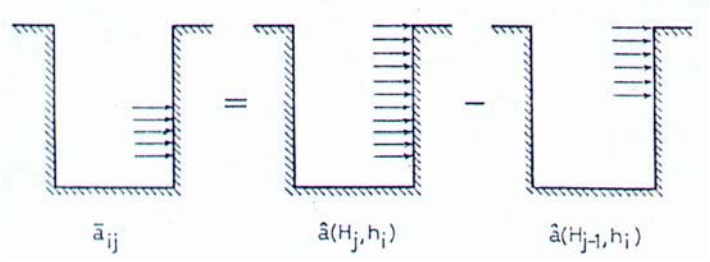

Figure 10: Schematic representation of $\bar{a}_{ij}$ [19].

Once the stresses *P*, *Q*, and *T*, are determined, the state of stress can be calculated by the following equations:

$$\sigma_{\max}, \sigma_{\min} = P \pm \sqrt{Q^2 + T^2} \qquad \text{(Eq. 3.23)}$$

$$\tau_{\max} = \sqrt{Q^2 + T^2} \qquad \text{(Eq. 3.24)}$$

$$\alpha = \frac{1}{2}\arctan\left(\frac{-T}{-Q}\right) \qquad \text{(Eq. 3.25)}$$

$$\sigma_x = P - Q \qquad \text{(Eq. 3.26)}$$

$$\sigma_y = P + Q \qquad \text{(Eq. 3.27)}$$

$$\tau_{xy} = T \qquad \text{(Eq. 3.28)}$$

3.3 INSTRUMENTATION AND SPECIMEN PREPARATION

A portable, battery-powered static strain indicator, supplemented by a precision switch-and-balance unit allows measurements in the field. The Vishay Measurements Group Model P-3500 Strain Indicator and SB-10 Switch-and-Balance Unit are ideally suited for this type of application. One can also use a computerized automatic data system when measurements are done in the laboratory. Regardless of the type of instrumentation used, ASTM E837 [12] requires that the instrumentation shall have a strain resolution of $\pm 2 \times 10^{-6}$, and stability and repeatability of the measurement shall be at least $\pm 2 \times 10^{-6}$.

Surface preparation is a very critical step in measuring residual stress by the hole drilling method, particularly incremental hole drilling. The surface of the material to be tested must be prepared for the bonding of strain gages. Use of abrasive papers or other

mechanical abrasion often generates spurious residual stresses on the surface. In one of his studies, Prevey [18] confirms that mechanical-abrasive techniques will induce residual stresses which could alter residual-stress distributions produced by machining, grinding, or shot-peening. Therefore, the use of abrasive papers should be used only if absolutely necessary. Electrolytic polishing is the preferred method of surface preparation. For this method, the prepared area must be flat [19] and a thorough cleaning and degreasing of the surface is also required.

After the surface preparation, the next step is to install the strain gage rosette. As with the surface preparation, it is important that the gage installation procedures be of the highest quality to allow accurate measurement of the small strains. A standard for surface preparation and rosette installation has been developed and is currently available in Vishay Measurements Group Instruction Bulletin B-129 [20].

3.4 MEASUREMENT PROCEDURE

Based on Measurements Group Tech Note (TN-503-5) [11], the hole drilling measurement procedure can be briefly summarized by six basic steps:

a. A three-element strain gage rosette is installed on the test part at the point where the residual stresses are to be determined. Prior to rosette installation, surface preparation is conducted at the location where rosette is to be installed.

b. The three gage grids are wired and connected to a static strain indicator, which is supplemented with a precision switch-and-balance unit.

c. A precision milling guide (Model RS-200, as shown in Figure 11) is attached to the test part and accurately centered over a drilling target on the rosette.

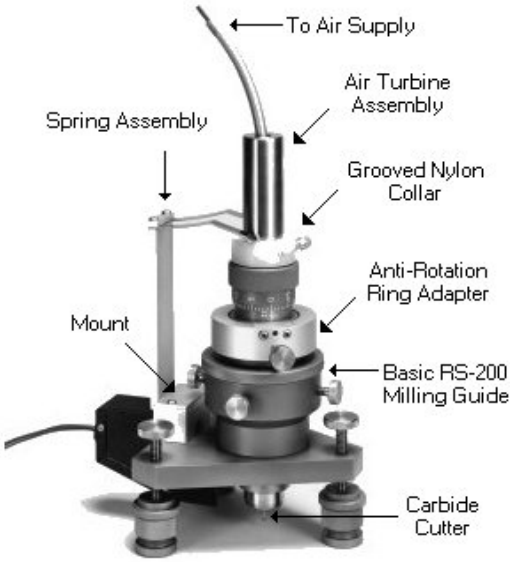

Figure 11: Model RS-200 Milling Guide [21].

d. After zero-balancing the gage circuits, a small and shallow hole is drilled through the center of the rosette.

e. Relaxed strains readings, which corresponds to the initial residual stress, are made.

f. Principal residual stresses and their angular orientation are calculated from the measured strains using the relationships described in Sections 3.1 and 3.2.

3.5 POTENTIAL ERRORS AND UNCERTAINTIES OF METHOD

The potential source of errors and uncertainties of the method [17] are as follows.

- Hole dimensions (diameter, concentricity, profile) – the center of the drilled hole has to coincide with the center of gage circle to $\pm 0.004D$ or $\pm 0.025\,\text{mm}$,

whichever is greater. More detail on the influence of hole eccentricity can be found in Ref. 22.

- Hole depth – in material whose thickness is at least 1.2*D*, the final depth of the hole should be 0.4*D* (blind-hole analysis); if material thickness is less than 1.2*D*, a hole passing through the entire thickness should be made (through-hole analysis).
- Surface roughness and flatness – should conform to the recommendations described in Section 3.3.
- Specimen (surface) preparation – should conform to the recommendations described in Section 3.3.
- Induced stresses from machining the hole – [23]
- Material properties – E and υ
- Incorrect gage selection – gage size (which is closely associated with drill size) should be considered in relation to the type of stresses present. Small size-gage should be used on specimen with steep stress gradients, since it gives a more localized measurement. However, small size-gages are more difficult to handle, only give limited depth information, and more susceptible to errors associated with misalignment or surface irregularities.
- Calibration coefficients and method of data analysis used – should conform to the recommendations described in Sections 3.1 and 3.2.
- Equipment and measurement resolution, systematic errors.

3.6 ADVANTAGES AND DISADVANTAGES OF METHOD

Strain-gage hole drilling is a simple and widely available method to measure residual stress in a material. Its instrumentation is portable, and therefore measurements can be conducted both in the laboratory and in the field. The method is also capable of testing a wide range of materials, such as metals, polymers, and ceramics. Moreover, strain-gage hole drilling is a well-established method, experimentally and theoretically. Specialized precision drilling equipment, along with well-proven experimental procedures are available for this method. Although a destructive technique, the small drilled hole on the sample generally will not significantly impair the structural integrity of the part being tested.

However, the strain-gage hole drilling method can be a tedious and long process. It requires a significant amount of time to install the rosettes and milling guide. The surface where the hole is to be drilled has to be prepared according to the standard [20] available to ensure good bonding between the rosette and the surface. In addition, it is also important that the hole be drilled exactly in the center of the rosette. These requirements make residual stress measurement using this technique difficult for field applications.

Other disadvantages of the method include interpretation of data, and limited strain sensitivity and resolution. Data interpretation is very important, and often very difficult. The data analysis method must also be appropriately chosen to match the expected stress profile of the material being tested.

Several works, including a study done by Gibmeier, et al. [24], confirm that the strain-gage hole drilling method is only capable of correctly quantifying residual stresses

in a material, if stress magnitudes are less than 60% of the material yield strength. Gibmeier, et al. claim that evaluation of residual stresses greater than this limit by the hole drilling method leads to significant overestimation. In contrast, results from an experimental study done by Nobre, et al. [25] show that residual stress results obtained from the strain-gage hole drilling method were still in good agreement with results obtained from the X-ray diffraction method, even when the magnitudes exceeded the yield strength of the bulk material.

4. ESPI HOLE DRILLING METHOD

The electronic speckle pattern interferometry (ESPI) hole drilling method was developed based on the strain-gage hole drilling method. It can measure residual stresses in a variety of materials, and does not require any surface preparation. Measurements can also be done in a very small amount of time. Images of the area around the hole are compared from before and after the hole is drilled. These images, together with properties of the material being tested and the geometry of the setup, allow determination of the state of residual stress. Since this method involves the introduction of a hole into the part being tested, it is considered to be destructive. In large or thick parts, this method may be considered semi-destructive, since the small hole introduced into the sample will not significantly impair the structural integrity of the part being tested.

4.1 PRINCIPLES

ESPI hole drilling is a technique capable of providing data on displacements (shape changes) at the surface of a material by mathematically combining deformation data, also known as the interferograms, registered digitally before and after the deformation occurs. In this case, the deformation is caused by drilling a hole in the test specimen.

Figure 12 shows the setup of a single beam ESPI system, as illustrated by Steinzig, et. al [26].

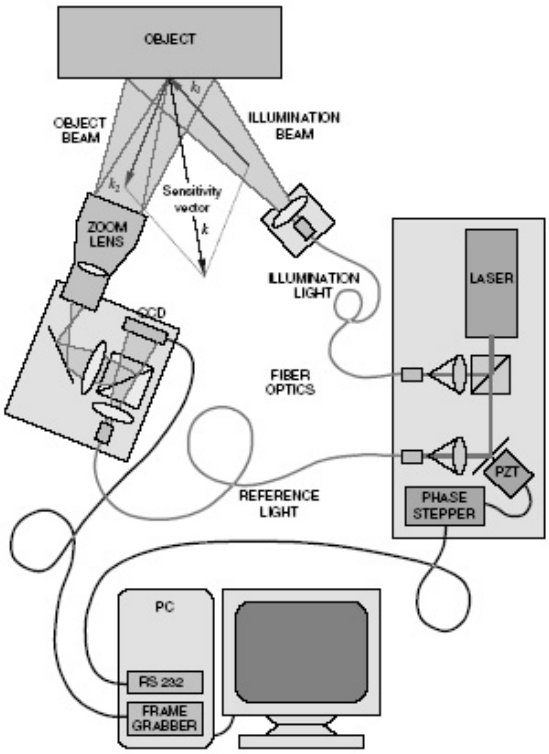

Figure 12: ESPI system setup [26].

The test specimen is exposed to a laser and viewed by a charge-coupled device (CCD) camera through a lens system and a prism that interferes the object light with a reference beam from the laser source. The CCD camera records this interference image, which is then stored in a computer for processing. The interference image illustrates a random-looking pattern of light and dark speckles, which is caused by the roughness of the sample and the optics. Images are taken several times before and after a hole is drilled. Images are stored and processed in the computer to give the corresponding interferograms on the area around a drilled hole. Figure 13 shows a speckle pattern with fringes, as a result of mathematical processing of the image data.

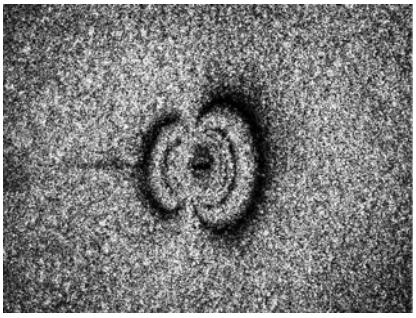

Figure 13: Speckle pattern with fringes.

The mathematical processing of the images is beyond the scope of this paper. More detailed information can be found in Ref. 26.

4.2 ANALYSIS TECHNIQUE

After deformation data is obtained, the next step is to calculate the associated residual stress. A number of techniques can be used for this purpose. In 1986, Nelson and McCrickerd [27] proposed one of the first implementations of combined holographic interferometry and blind-hole drilling to measure residual stresses in a material. They derived a method to relate radial displacements measured in three directions of illumination to the state of residual stress, similar to relations used in the conventional strain-rosette technique.

Later in 1997, Nelson, et al. [28] further developed this analysis technique, which was then adapted by Steinzig, et al. [29] in 2001, to be applied to an ESPI system. In this analysis technique, after the interferograms are acquired, they provide the change in the illumination beam's path length (ΔP). The value of ΔP corresponds to the surface displacements as a result of the stress relaxation. The relationship between change in path length (ΔP) and state of residual stress can be expressed by the following equation:

$$\begin{Bmatrix} \overline{\Delta P_1} \\ \overline{\Delta P_2} \\ \overline{\Delta P_3} \end{Bmatrix} = \begin{bmatrix} C_{11} C_{12} C_{13} \\ C_{21} C_{22} C_{23} \\ C_{31} C_{32} C_{33} \end{bmatrix} \begin{Bmatrix} \sigma_{xx} \\ \sigma_{yy} \\ \tau_{xy} \end{Bmatrix} \qquad \text{(Eq. 4.1)}$$

The C_{ij} values contain constitutive properties, geometric properties, holographic sensitivity factors, and finite element derived coefficients. $\overline{\Delta P_i}$ is the difference in path (phase) length between two surface points which are diametrically opposed to one another, but at the same radial location from the center of the hole, defined by:

$$\overline{\Delta P_i} = \Delta P(r_i, \theta_i) - \Delta P(r_i, \theta_i + \pi) \qquad \text{(Eq. 4.2)}$$

Based on the two equations above, it is apparent that three holographic pairs of data are sufficient to determine the plane state of residual stress at a particular point of interest (where the hole is drilled).

Since the CCD in an ESPI system typically consists of 256,000 pixel elements, there are thousands of data points around the hole that are available to determine the state of stress. Each phase change triad provides an independent stress calculation. The software processes thousands of these phase change triads, and then averages them to yield the reported residual stress value.

Another technique used to convert deformation data to calculate residual stress is the Full Field Least Square (FFLSQ) technique [30]. Unlike previous methods, FFLSQ is not developed from the through-hole analysis, described in Section 3.1. The deformation is modeled directly using finite elements, over the full range of each variable. Interpolation tables can then be generated based on the finite element runs to provide the best fit to the deformation maps obtained from ESPI. This technique is discussed in detail in Ref. 30.

4.3 POTENTIAL ERRORS AND UNCERTAINTIES OF METHOD

Since the ESPI hole drilling method is developed based on the strain-gage hole drilling method, several potential sources of residual stress measurement errors are identical to those of the strain-gage hole drilling method (Section 3.5). However, some of the sources of error have been eliminated or reduced. Since there is no strain gage rosette attached, surface preparation is unnecessary.

In an ESPI system, strains are derived from raw ESPI data on displacement. The stress is then calculated based on a user-provided modulus of elasticity of the material being tested. Therefore, any error in the modulus input automatically results into a relative error in the value of residual stress.

Surface displacements are linearly proportional to the hole depth. Thus, any error in the hole depth will produce errors in the stresses. Surface displacements are also linearly dependent on hole diameter. The diameter of the drilled hole depends on the following factors [31]: drill chuck wobble, machineability of the material, drilling speed and feed, cutting tool tolerance. Steinzig and Ponchione [32] found that at very low drill speeds, the resulting holes are not circular; this also contributes to error.

After the hole has been drilled to the test part, the user of an ESPI system defines the boundaries of the hole using its graphical hole-marking tool to determine the location of the hole. Numerical experiments were conducted to evaluate the effects of error in hole center location on the stress results. As described by Ponslet and Steinzig [31], errors due to X position error are greater compared to the errors due to Y position error.

As in the strain-gage hole drilling method, strains are induced as a hole is drilled into a part. These induced strains should be kept as low as possible and as limited as possible in radial extent away from the hole, so that an area can be masked out [31]. Error caused by this factor is difficult to quantify because it varies depending on the material type and drilling parameters.

Other potential sources of errors are discussed in detail by Ponslet and Steinzig [31], such as image scale, sensitivity vector, cone beams, wavelength, laser intensity fluctuations, and drill type of the corresponding ESPI system.

4.4 ADVANTAGES AND DISADVANTAGES OF METHOD

The ESPI hole drilling method eliminates several disadvantages of the strain-gage hole drilling method (Section 3.6). In addition to its capability to collect data in a short amount of time in a variety of materials, this method also eliminates the need for strain gage rosette and the required surface preparation. This method also has the ability to access smaller regions and information on the displacement field associated with the introduction of the hole [33].

An ESPI system is fairly portable, and therefore measurements can be easily and conveniently conducted both in the laboratory and in the field. Figure 14 shows a PRISM ESPI system, which was developed by Hytec, Incorporated of Los Alamos, New Mexico.

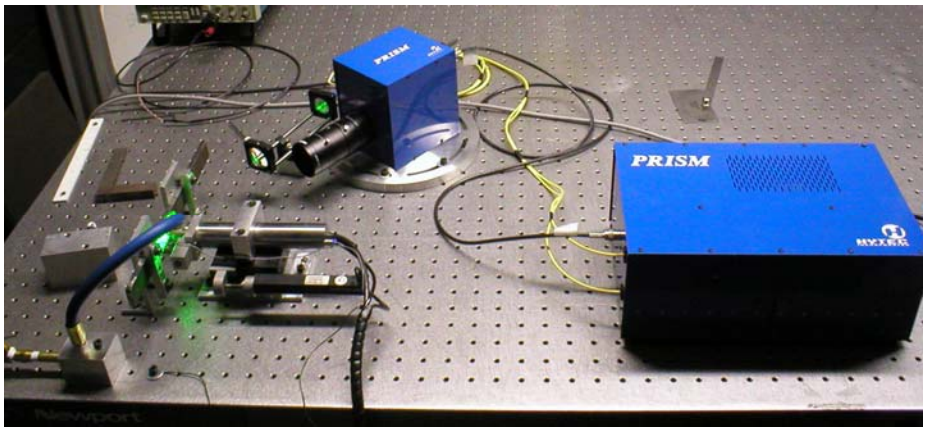

Figure 14: Hytec, Incorporated PRISM ESPI system.

However, since this is a new technology, there are no well-proven experimental procedures available. More research is required to better establish this method, both experimentally and theoretically.

Finally, similar to the strain-gage hole drilling method, the small drilled hole on the sample generally will not significantly impair the structural integrity of the part being tested.

5. EXPERIMENTAL DETAILS

5.1 MATERIAL TESTED

A total of twenty mild steel samples were used in this research. Ten samples were unblasted and the other ten were sandblasted. All samples have dimensions of 11" x 1" x ¼" (*l* x *w* x *h*), and were cut from the same plate. Therefore all twenty samples have the same mechanical properties and chemical composition. Table 3 shows the material details of the samples tested.

Table 3: Mechanical properties and chemical composition of material tested.

Material	ASTM A36(01) / A709(01A) / ASME SA36(01ED) / AASHTO M20(01)36														
Young's Modulus (E)	30,733 ksi														
Poisson's ratio (υ)	0.29														
Yield Strength (YS)	56,000 – 59,000 psi														
Ultimate Tensile Strength (UTS)	69,000 – 73,000 psi														
% Elongation	25 – 32														
Weight	490 pcf														
Chemical composition (% weight)	*C*	*Mn*	*P*	*S*	*Si*	*Al*	*Cu*	*Ni*	*Cr*	*Mo*	*Cb*	*V*	*Ti*	*B*	*N*
	0.16	0.84	0.010	0.002	0.04	0.025	0.30	0.19	0.14	0.09	0.002	0.005	0.018	0.0001	0.0114

All sandblasted samples were subjected to a white metal blast process using #4 grit silica sand, blasted at a pressure of 100 psi.

5.2 X-RAY DIFFRACTION METHOD

5.2.1 Machine Information and System Settings

All X-ray diffraction measurements were performed using Philips X'Pert PW3040 MPD (Figure 15), which was set up with a PW3011/20 proportional detector and PW3071 sample holder with clip (Figure 16).

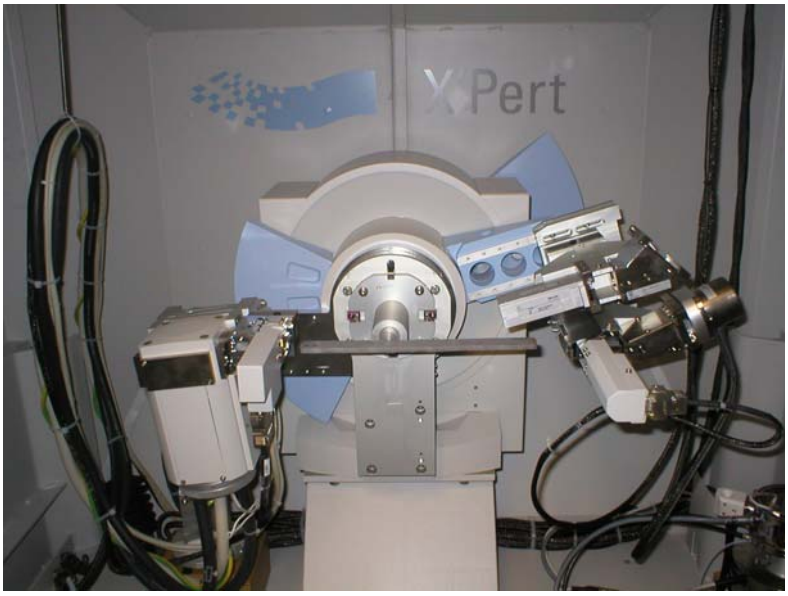

Figure 15: Philips X'Pert PW3040 MPD X-ray diffractometer.

Figure 16: Philips PW3071 sample holder with clip.

The X-ray source used was a Cu radiation source, with K-α wavelength of 1.5418740 Å. Tube voltage and current were set to 45 kV and 40 mA, respectively. Apertures used included PW3123/10 monochromator for Cu, divergence and scattering slits of ½°, receiving slit of 0.30 mm, and soller slit of 0.04 rad.

5.2.2 Test Parameters

Corresponding to the sample stage used, the stress mode was omega stress, with scan axis of 2θ-omega. Seven tilts for both positive and negative ψ angle were used, as recommended by Fitzpatrick, et al. [3]. For both types of samples, the diffraction angle step size was 0.05°, with a counting time of 20 seconds per step. This yielded a scan speed of 0.0025°/second and a total number of steps of 120. One XRD measurement typically lasted about 8-9 hours.

For omega stress, the value of maximum ψ angle depended on the start angle of the scan range (ψ max = [½ * start angle] – 1). Although both unblasted and sandblasted samples were identical in properties, one yielded a higher angle peak than the other, which was revealed after running quick scans on both types of the samples. Results show that high angle peak occurred at 138.5° at {331} plane for the unblasted samples, and 137.0° at {222} plane for the sandblasted samples. Since the high angle peak of each type of samples was different, the start angle for each type was also different. For unblasted samples, diffraction angle range was 135.5°-141.5°, which yielded a maximum ψ angle value of 66.75°. For the sandblasted samples, diffraction angle range was 134°-140° and the maximum ψ angle value was 66°. The difference in the high angle peak for unblasted and sandblasted samples most likely was caused by the very different surface conditions. The unblasted samples had smooth surface profiles when compared to the sandblasted surface, but mill scale was evident at the surface. The sandblasted samples had no mill scale at the surface, but their surface profile was uniformly uneven.

5.3 STRAIN-GAGE HOLE DRILLING METHOD

5.3.1 Specimen Preparation

Surface preparations and strain gage rosette installations of all twenty samples were completed according to Vishay Measurements Group Instruction Bulletin B-129 [20]. Strain gage rosettes CEA-06-062UL-120 from Micro-Measurements with grid centerline diameter of 0.202 in. and a gage length of 0.062 in, were chosen to be used on all samples to be tested. The gage factor for all rosettes used was 2.06.

5.3.2 Instrumentation Information and System Setup

For strain measurement readings, the Vishay Measurements Group Model P-3500 Strain Indicator and SB-10 Switch-and-Balance Unit were used. The precision milling guide model RS-200 from Measurements Group was used to accurately center the drill on the rosette and drill the target. Vishay cutters (drill bits) with diameter of 0.062 in. were selected for all incremental hole drilling done on the samples. Figure 17 shows the strain-gage hole drilling method complete setup for all samples tested.

Figure 17: Strain-gage hole drilling method setup.

As shown by Figure 18, a steel plate with a cutout of the size of the sample was used to hold each sample in place during the drilling process.

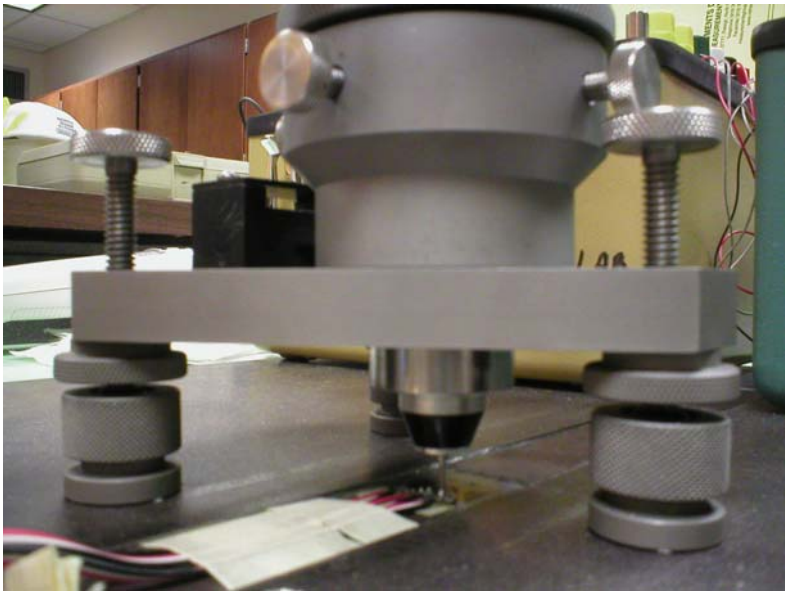

Figure 18: Sample holder used for the strain-gage hole drilling method.

5.3.3 Test Parameters

Air supply pressure for the drill was set to 40 psi. The high-speed turbine turns at hundreds of thousand of revolutions per minute. Drill feed rate is controlled by the operator, with an approximate rate of 0.00025 in./sec. Nine drilling increments were performed on each of the twenty samples. The first increment was at depth of 0.005 in. from surface, the second was at 0.010 in., the third was at 0.020 in., and so on, up to the last increment, at depth of 0.080 in. from surface.

5.4 ESPI HOLE DRILLING METHOD

5.4.1 System Information and Setup

All residual stress measurements using this method were completed using the PRISM Electronic Speckle Pattern Interferometry (ESPI) system developed by Hytec, Incorporated. The system utilizes a type IIIB laser. Two-fluted end mills with diameter

of 0.0625 in. were selected for all incremental hole drilling done on the samples, with the exception of two measurements, which used the same drill bit as the strain-gage hole drilling method (Section 5.3.2). Figure 14 shows a partial setup of the PRISM ESPI system. The connection between the video head and the computer, as well as the signal connection between the laser source and the computer are not shown in the figure. A typical complete setup of the system is shown on Figure 12.

All samples tested were clipped on two aluminum angle pieces, which were placed along the length of the bar, as shown on Figures 19a and 19b.

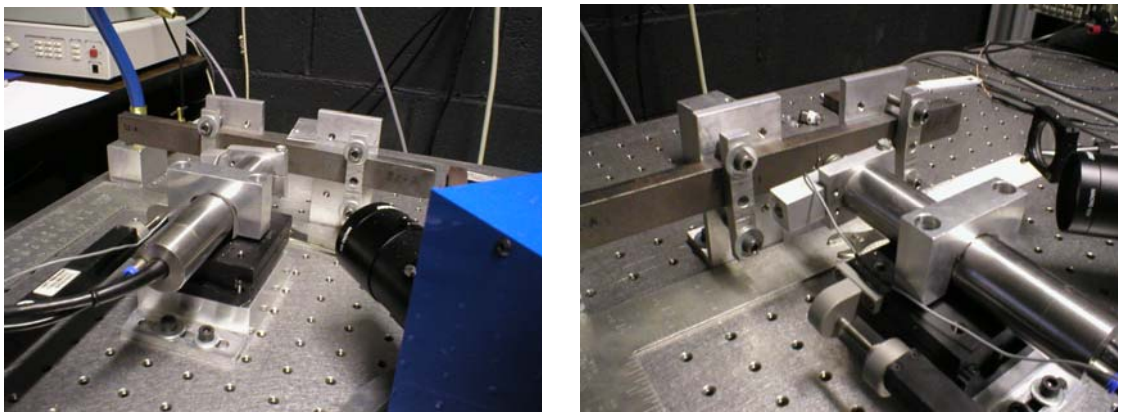

Figure 19a, b: Sample holder used for the ESPI hole drilling method.

5.4.2 Test Parameters

Since there had not been a previous study to determine the optimum test parameters to use for this particular kind of material, three different drill speed values were tested: 35,000, 20,000, and 10,000 rpm; and two different drill feed rate values were tested: 0.05 and 0.15mm/s. Six 0.12-mm drilling increments were performed on all ESPI hole drilling measurements.

6. RESULTS

6.1 X-RAY DIFFRACTION METHOD

For each sample tested, two X-ray diffraction measurements at different locations were taken along the centerline. The first location was a distance of 3.250 in. from one end of the sample and the second was at a distance of 4.125 in. from the same end, with each point labeled as A and B, respectively, as shown by Figure 20. The residual stress at point A would also be measured using the strain-gage hole drilling method, and stress at point B would be measured using the ESPI hole drilling method. All unblasted samples start with the prefix 'US', and all sandblasted samples start with the prefix 'SS'. The X-ray diffractometer used in this research (Figure 15) is only capable of performing uniaxial stress analysis. Therefore, all XRD measurements were taken in one direction, at $\phi = 0°$ (along the x-axis or longitudinal axis).

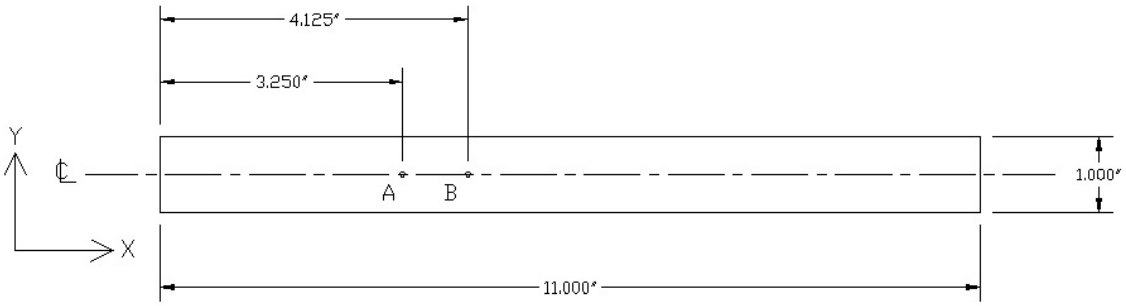

Figure 20: Measurement locations on sample with coordinate system.

Stresses were analyzed using the $Sin^2\psi$ method and the X'Pert Stress software developed by Philips Analytical. Each ψ tilt yielded a point with coordinates of ($\sin^2\psi$, d), which was plotted on the d versus $\sin^2\psi$ curve. By elliptical fitting, and incorporating the elastic properties of the material, the stress value σ_ϕ, or in this case referred to as σ_{xx}, was determined. For most of the samples tested, the ordinates of several data points were either too low or too high with respect to the trend behavior of other data points. These conditions caused the stress results to have high standard deviation values. Because of this, three stress analyses were performed for each point measured: one with all data points analyzed, one neglecting the two end points on the curve, and one neglecting the four end points on the curve. The graphs of each stress analysis, along with its corresponding stress value were then plotted. All stress results were then summarized in two separate tables, one for the unblasted samples and the other for the sandblasted samples. Some reasons for the high variability in the results include the use of a copper anode instead of chromium, as well as the differences in surface conditions of the unblasted and sandblasted samples.

6.1.1 Unblasted Samples

Figure 21 shows three- d vs. $\sin^2\psi$ curves for each X-ray diffraction measurement of the unblasted samples.

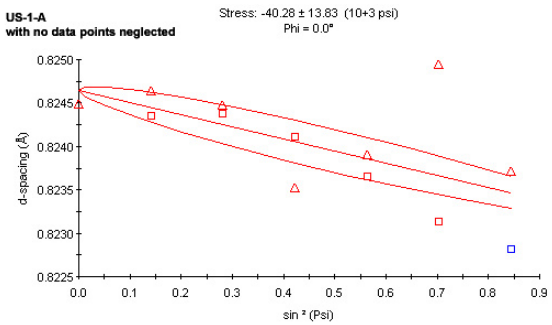
US-1-A
with no data points neglected
Stress: -40.28 ± 13.83 (10+3 psi)
Phi = 0.0°
d-spacing (Å)
sin ² (Psi)

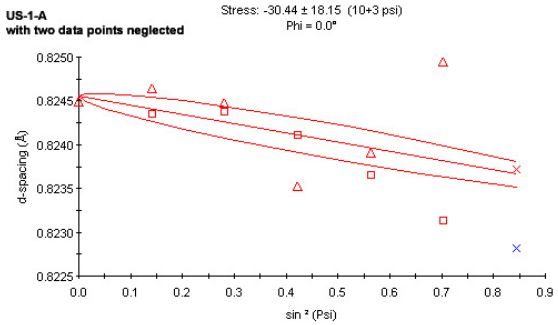
US-1-A
with two data points neglected
Stress: -30.44 ± 18.15 (10+3 psi)
Phi = 0.0°
d-spacing (Å)
sin ² (Psi)

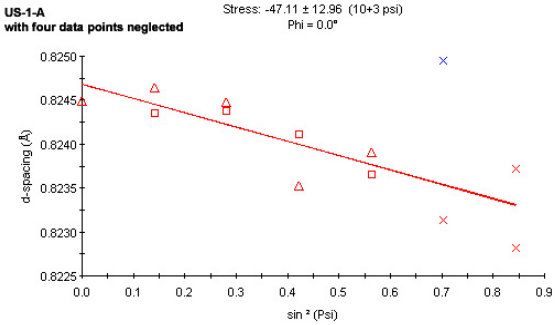
US-1-A
with four data points neglected
Stress: -47.11 ± 12.96 (10+3 psi)
Phi = 0.0°
d-spacing (Å)
sin ² (Psi)

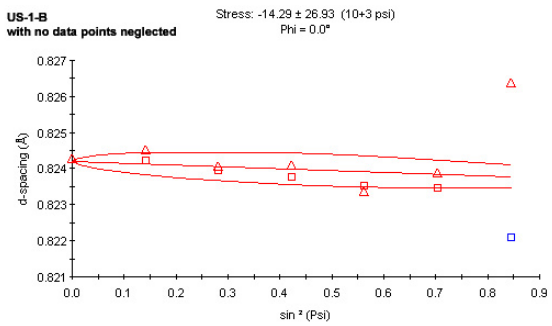
US-1-B
with no data points neglected
Stress: -14.29 ± 26.93 (10+3 psi)
Phi = 0.0°
d-spacing (Å)
sin ² (Psi)

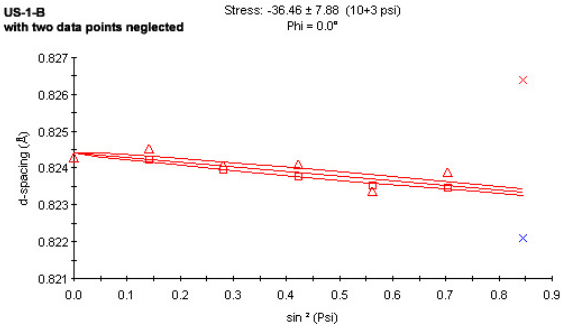
US-1-B
with two data points neglected
Stress: -36.46 ± 7.88 (10+3 psi)
Phi = 0.0°
d-spacing (Å)
sin ² (Psi)

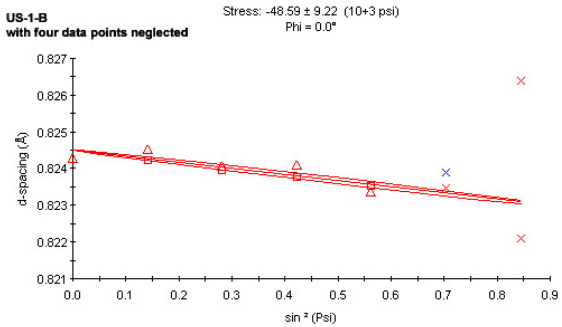
US-1-B
with four data points neglected
Stress: -48.59 ± 9.22 (10+3 psi)
Phi = 0.0°
d-spacing (Å)
sin ² (Psi)

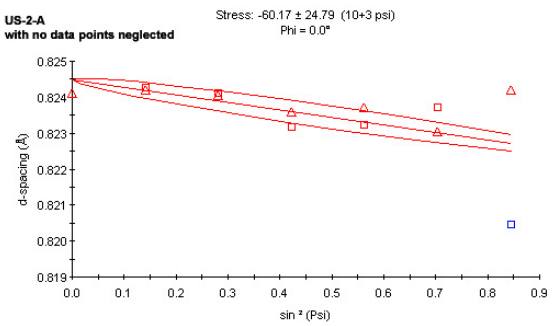
US-2-A
with no data points neglected
Stress: -60.17 ± 24.79 (10+3 psi)
Phi = 0.0°
d-spacing (Å)
sin ² (Psi)

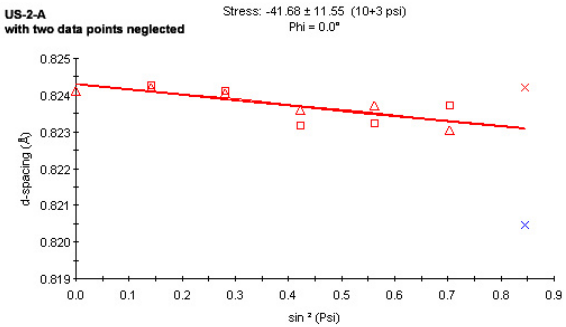
US-2-A
with two data points neglected
Stress: -41.68 ± 11.55 (10+3 psi)
Phi = 0.0°
d-spacing (Å)
sin ² (Psi)

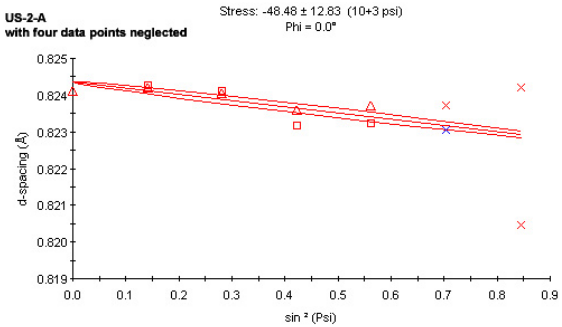
US-2-A
with four data points neglected
Stress: -48.48 ± 12.83 (10+3 psi)
Phi = 0.0°
d-spacing (Å)
sin ² (Psi)

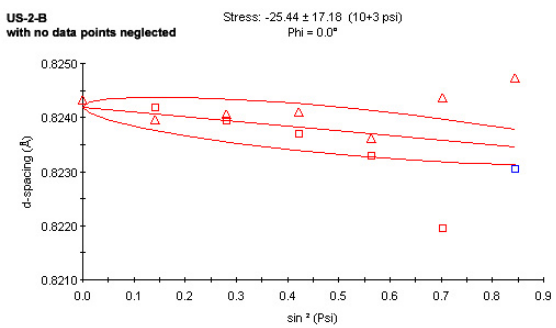
US-2-B
with no data points neglected
Stress: -25.44 ± 17.18 (10+3 psi)
Phi = 0.0°
d-spacing (Å)
sin ² (Psi)

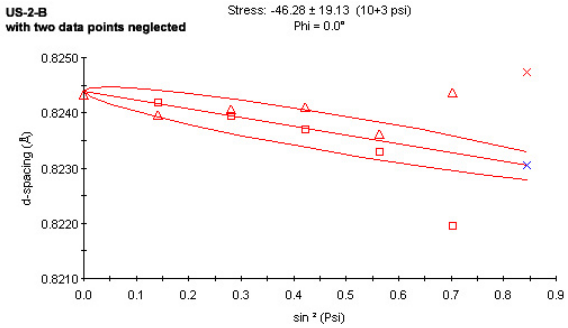
US-2-B
with two data points neglected
Stress: -46.28 ± 19.13 (10+3 psi)
Phi = 0.0°
d-spacing (Å)
sin ² (Psi)

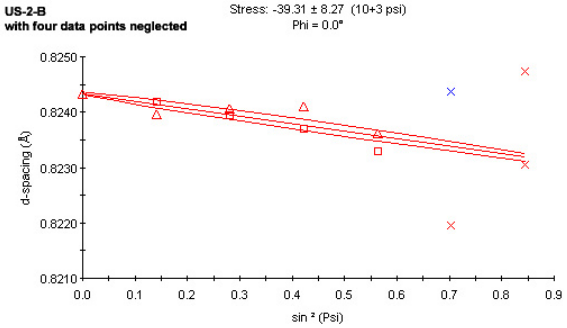
US-2-B
with four data points neglected
Stress: -39.31 ± 8.27 (10+3 psi)
Phi = 0.0°
d-spacing (Å)
sin ² (Psi)

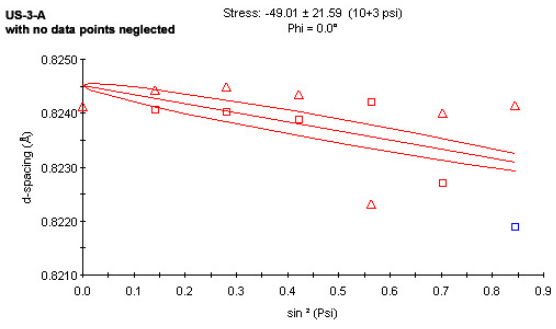
US-3-A
with no data points neglected
Stress: -49.01 ± 21.59 (10+3 psi)
Phi = 0.0°
d-spacing (Å)
sin ² (Psi)

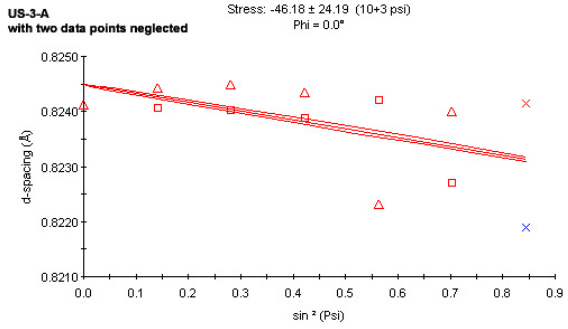
US-3-A
with two data points neglected
Stress: -46.18 ± 24.19 (10+3 psi)
Phi = 0.0°
d-spacing (Å)
sin ² (Psi)

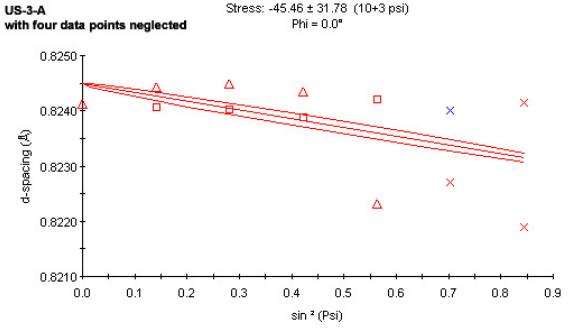
US-3-A
with four data points neglected
Stress: -45.46 ± 31.78 (10+3 psi)
Phi = 0.0°
d-spacing (Å)
sin ² (Psi)

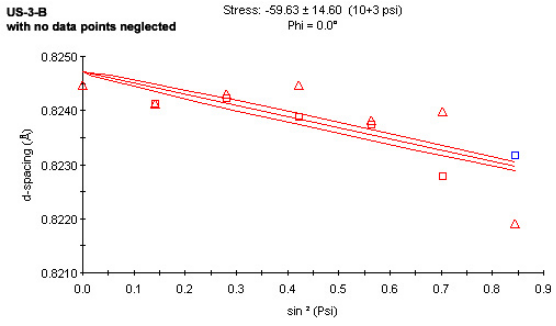
US-3-B
with no data points neglected
Stress: -59.63 ± 14.60 (10+3 psi)
Phi = 0.0°
d-spacing (Å)
sin ² (Psi)

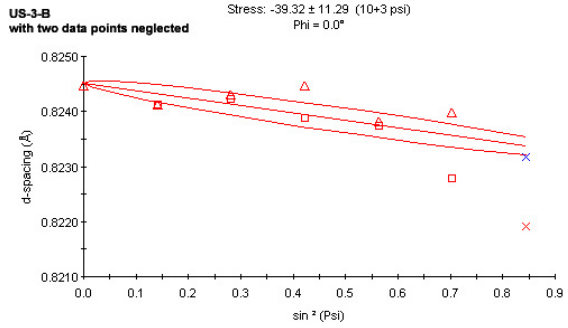
US-3-B
with two data points neglected
Stress: -39.32 ± 11.29 (10+3 psi)
Phi = 0.0°
d-spacing (Å)
sin ² (Psi)

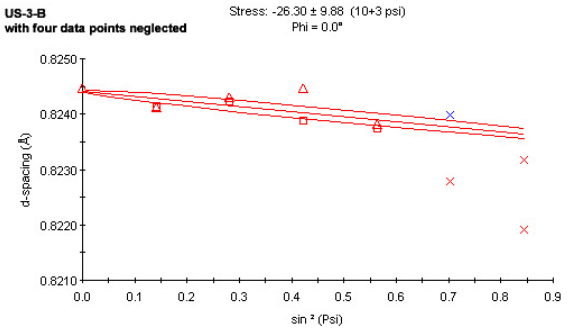
US-3-B
with four data points neglected
Stress: -26.30 ± 9.88 (10+3 psi)
Phi = 0.0°
d-spacing (Å)
sin ² (Psi)

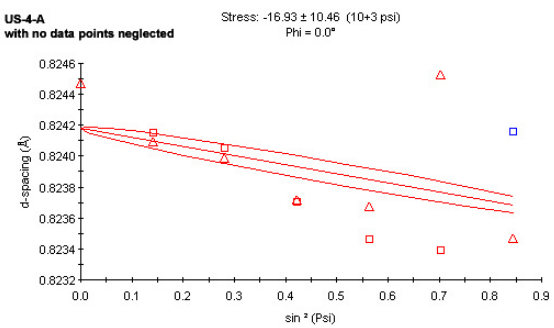
US-4-A
with no data points neglected
Stress: -16.93 ± 10.46 (10+3 psi)
Phi = 0.0°
d-spacing (Å)
sin ² (Psi)

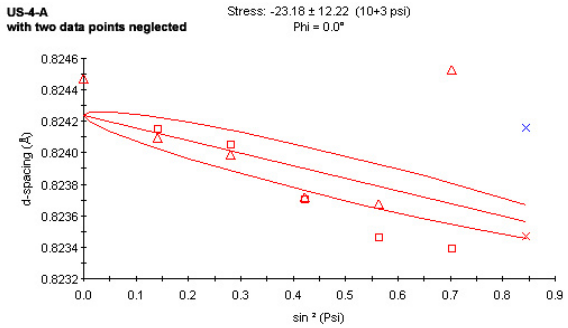
US-4-A
with two data points neglected
Stress: -23.18 ± 12.22 (10+3 psi)
Phi = 0.0°
d-spacing (Å)
sin ² (Psi)

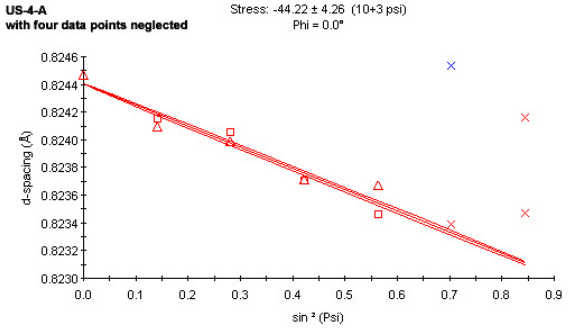
US-4-A
with four data points neglected
Stress: -44.22 ± 4.26 (10+3 psi)
Phi = 0.0°
d-spacing (Å)
sin ² (Psi)

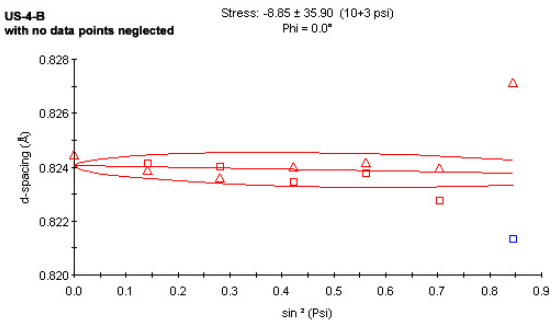
US-4-B
with no data points neglected
Stress: -8.85 ± 35.90 (10+3 psi)
Phi = 0.0°
d-spacing (Å)
sin ² (Psi)

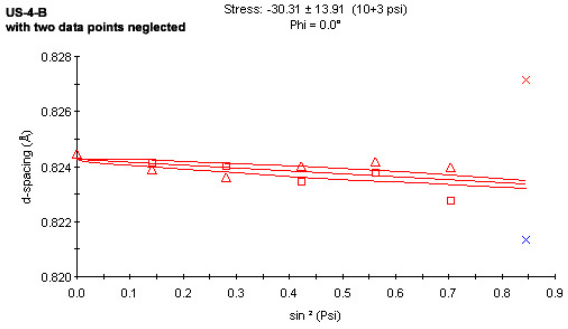
US-4-B
with two data points neglected
Stress: -30.31 ± 13.91 (10+3 psi)
Phi = 0.0°
d-spacing (Å)
sin ² (Psi)

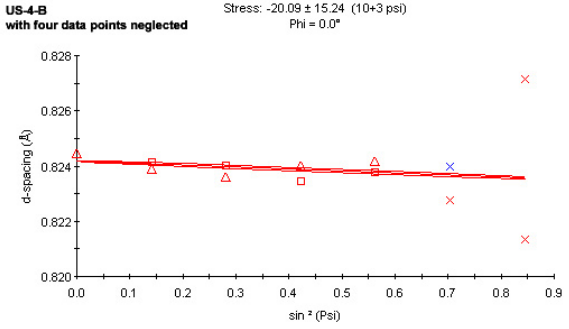
US-4-B
with four data points neglected
Stress: -20.09 ± 15.24 (10+3 psi)
Phi = 0.0°
d-spacing (Å)
sin ² (Psi)

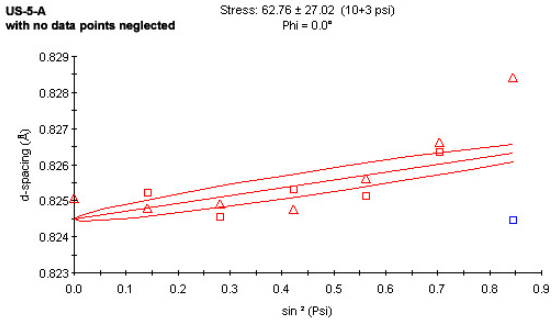
US-5-A
with no data points neglected
Stress: 62.76 ± 27.02 (10+3 psi)
Phi = 0.0°
d-spacing (Å)
sin ² (Psi)

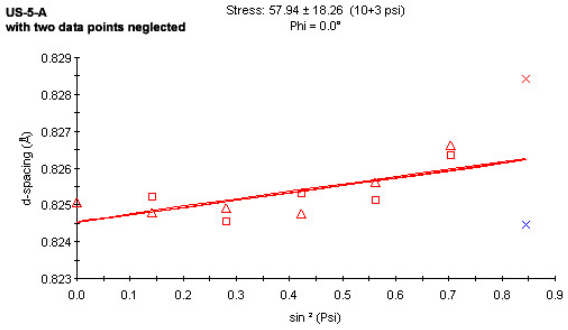
US-5-A
with two data points neglected
Stress: 57.94 ± 18.26 (10+3 psi)
Phi = 0.0°
d-spacing (Å)
sin ² (Psi)

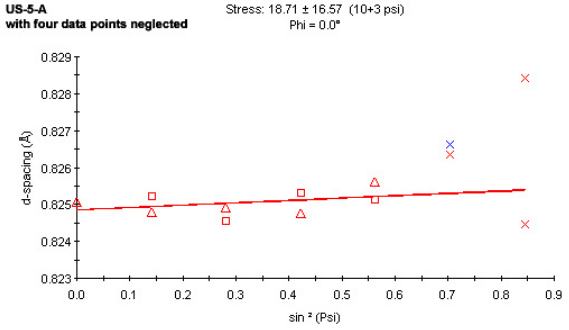
US-5-A
with four data points neglected
Stress: 18.71 ± 16.57 (10+3 psi)
Phi = 0.0°
d-spacing (Å)
sin ² (Psi)

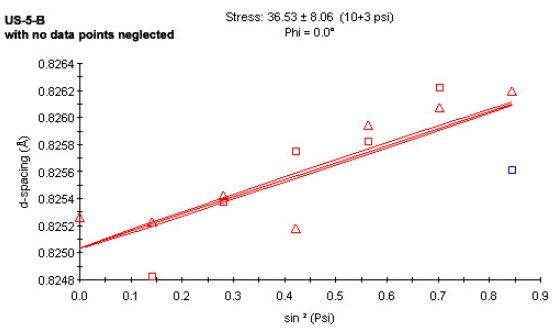
US-5-B
with no data points neglected
Stress: 36.53 ± 8.06 (10+3 psi)
Phi = 0.0°
d-spacing (Å)
sin ² (Psi)

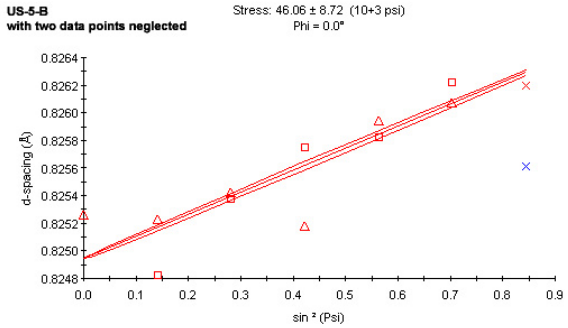
US-5-B
with two data points neglected
Stress: 46.06 ± 8.72 (10+3 psi)
Phi = 0.0°
d-spacing (Å)
sin ² (Psi)

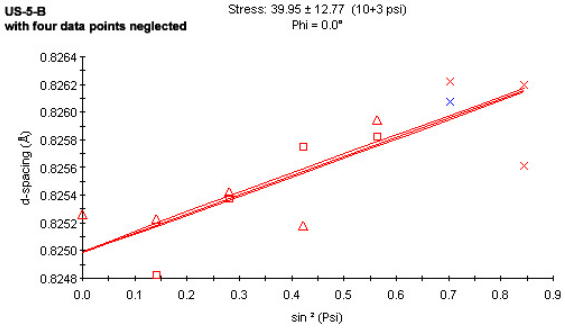
US-5-B
with four data points neglected
Stress: 39.95 ± 12.77 (10+3 psi)
Phi = 0.0°
d-spacing (Å)
sin ² (Psi)

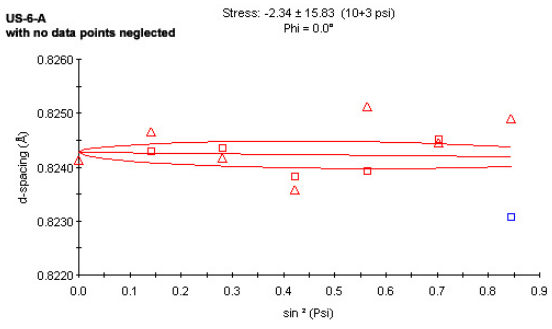
US-6-A
with no data points neglected
Stress: -2.34 ± 15.83 (10+3 psi)
Phi = 0.0°
d-spacing (Å)
sin ² (Psi)

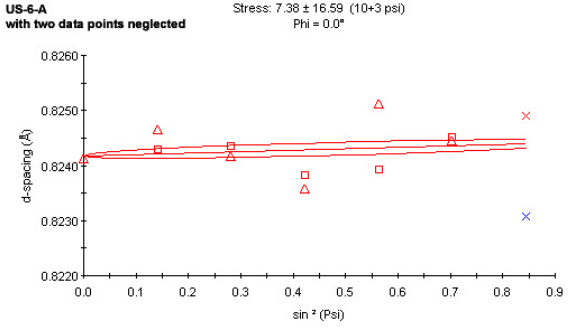
US-6-A
with two data points neglected
Stress: 7.38 ± 16.59 (10+3 psi)
Phi = 0.0°
d-spacing (Å)
sin ² (Psi)

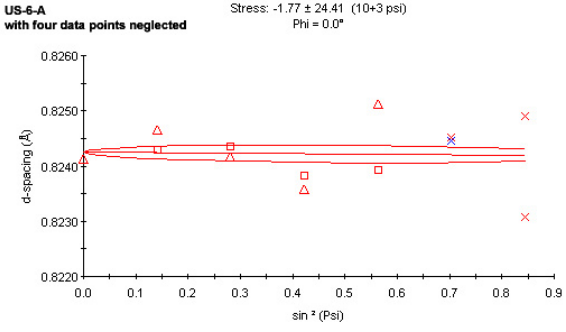
US-6-A
with four data points neglected
Stress: -1.77 ± 24.41 (10+3 psi)
Phi = 0.0°
d-spacing (Å)
sin ² (Psi)

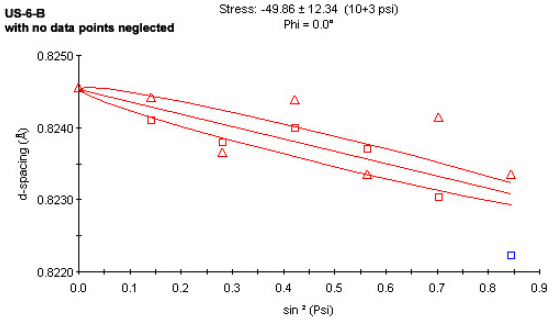
US-6-B
with no data points neglected
Stress: -49.86 ± 12.34 (10+3 psi)
Phi = 0.0°
d-spacing (Å)
sin ² (Psi)

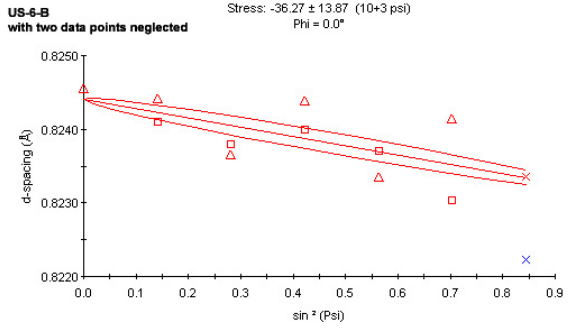
US-6-B
with two data points neglected
Stress: -36.27 ± 13.87 (10+3 psi)
Phi = 0.0°
d-spacing (Å)
sin ² (Psi)

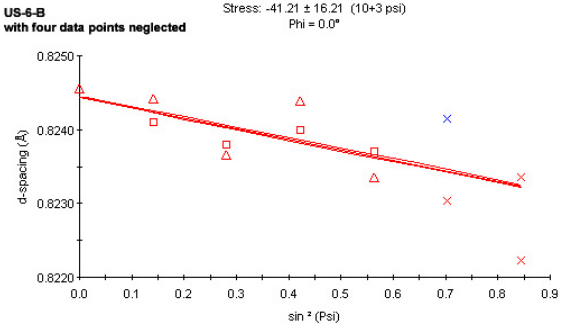
US-6-B
with four data points neglected
Stress: -41.21 ± 16.21 (10+3 psi)
Phi = 0.0°
d-spacing (Å)
sin ² (Psi)

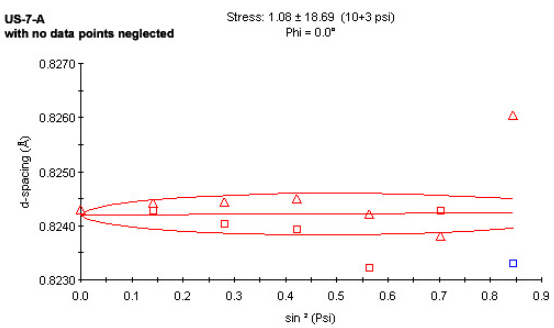
US-7-A
with no data points neglected
Stress: 1.08 ± 18.69 (10+3 psi)
Phi = 0.0°
d-spacing (Å)
sin ² (Psi)

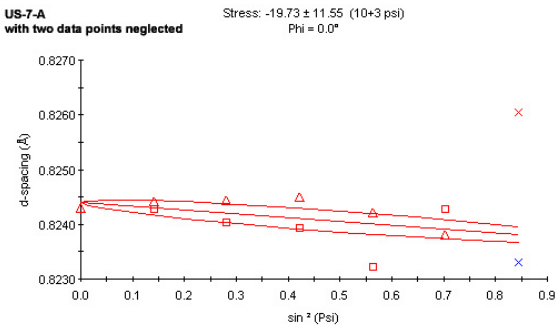
US-7-A
with two data points neglected
Stress: -19.73 ± 11.55 (10+3 psi)
Phi = 0.0°
d-spacing (Å)
sin ² (Psi)

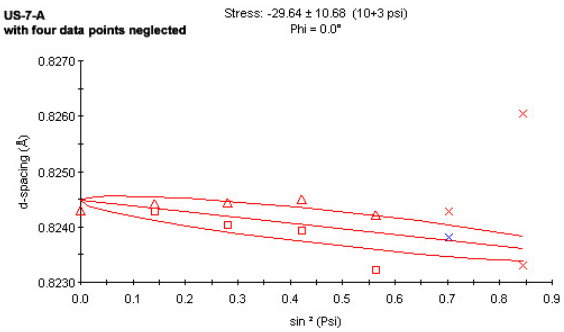
US-7-A
with four data points neglected
Stress: -29.64 ± 10.68 (10+3 psi)
Phi = 0.0°
d-spacing (Å)
sin ² (Psi)

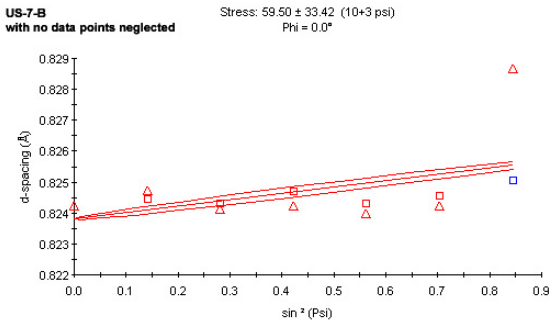
US-7-B
with no data points neglected
Stress: 59.50 ± 33.42 (10+3 psi)
Phi = 0.0°
d-spacing (Å)
sin ² (Psi)

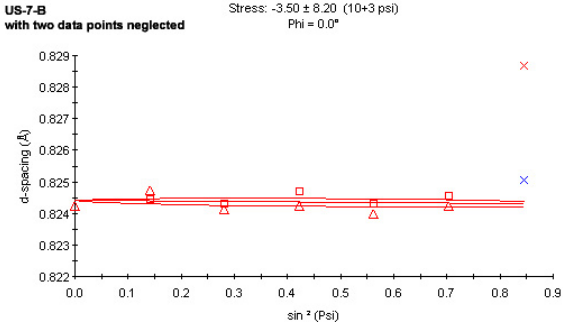
US-7-B
with two data points neglected
Stress: -3.50 ± 8.20 (10+3 psi)
Phi = 0.0°
d-spacing (Å)
sin ² (Psi)

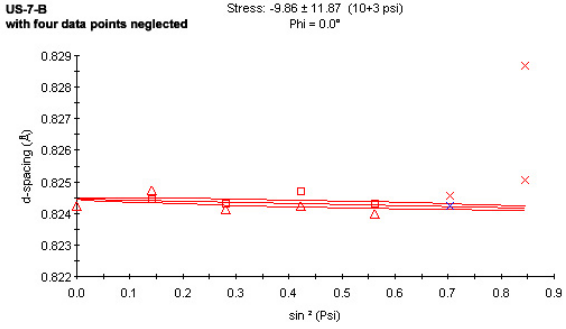
US-7-B
with four data points neglected
Stress: -9.86 ± 11.87 (10+3 psi)
Phi = 0.0°
d-spacing (Å)
sin ² (Psi)

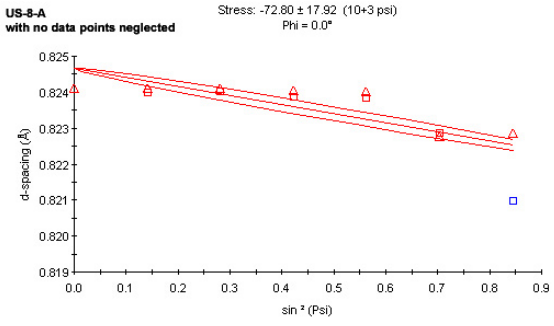
US-8-A
with no data points neglected
Stress: -72.80 ± 17.92 (10+3 psi)
Phi = 0.0°
d-spacing (Å)
sin ² (Psi)

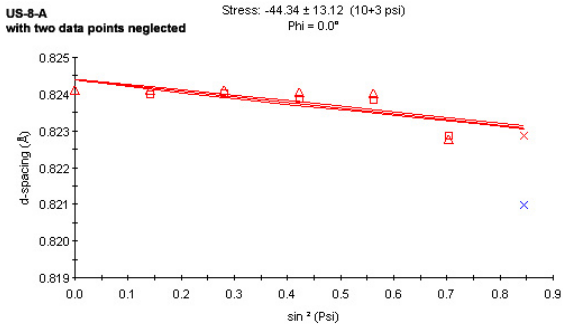
US-8-A
with two data points neglected
Stress: -44.34 ± 13.12 (10+3 psi)
Phi = 0.0°
d-spacing (Å)
sin ² (Psi)

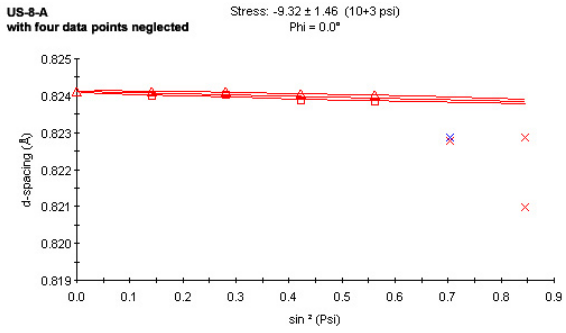
US-8-A
with four data points neglected
Stress: -9.32 ± 1.46 (10+3 psi)
Phi = 0.0°
d-spacing (Å)
sin ² (Psi)

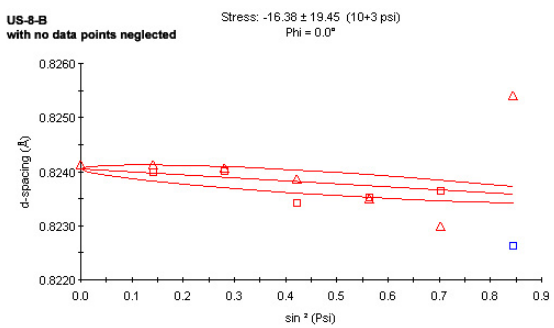
US-8-B
with no data points neglected
Stress: -16.38 ± 19.45 (10+3 psi)
Phi = 0.0°
d-spacing (Å)
sin ² (Psi)

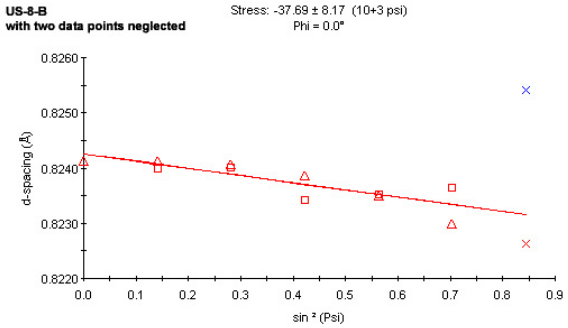
US-8-B
with two data points neglected
Stress: -37.69 ± 8.17 (10+3 psi)
Phi = 0.0°
d-spacing (Å)
sin ² (Psi)

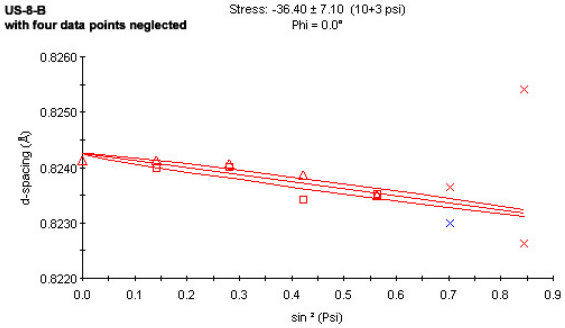
US-8-B
with four data points neglected
Stress: -36.40 ± 7.10 (10+3 psi)
Phi = 0.0°
d-spacing (Å)
sin ² (Psi)

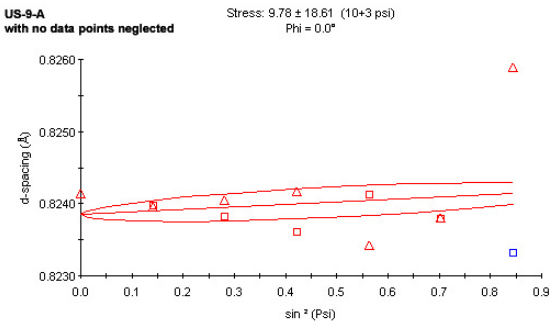
US-9-A
with no data points neglected
Stress: 9.78 ± 18.61 (10+3 psi)
Phi = 0.0°
d-spacing (Å)
sin ² (Psi)

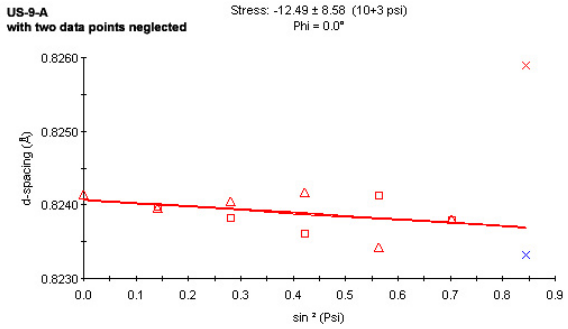
US-9-A
with two data points neglected
Stress: -12.49 ± 8.58 (10+3 psi)
Phi = 0.0°
d-spacing (Å)
sin ² (Psi)

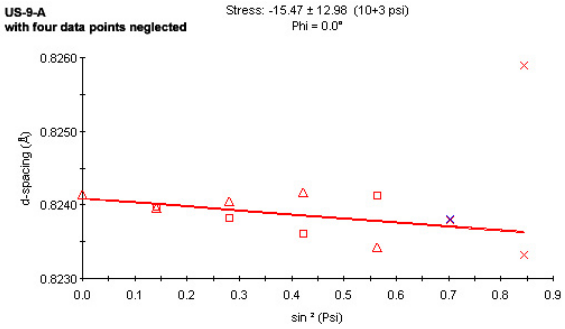
US-9-A
with four data points neglected
Stress: -15.47 ± 12.98 (10+3 psi)
Phi = 0.0°
d-spacing (Å)
sin ² (Psi)

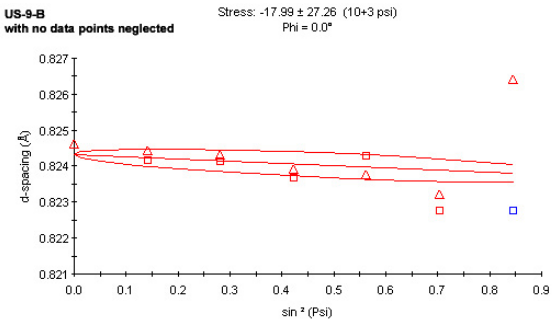
US-9-B
with no data points neglected
Stress: -17.99 ± 27.26 (10+3 psi)
Phi = 0.0°
d-spacing (Å)
sin ² (Psi)

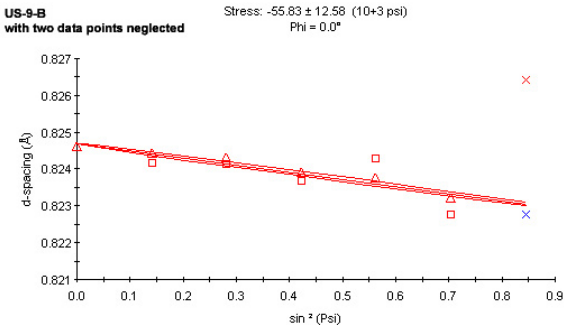
US-9-B
with two data points neglected
Stress: -55.83 ± 12.58 (10+3 psi)
Phi = 0.0°
d-spacing (Å)
sin ² (Psi)

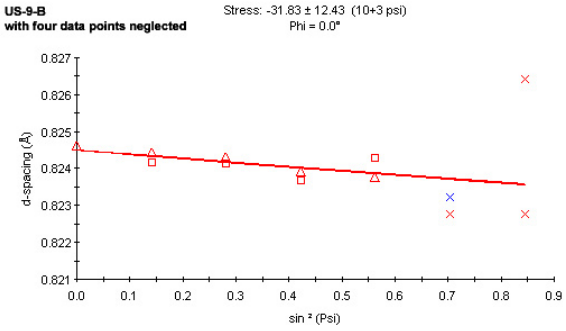
US-9-B
with four data points neglected
Stress: -31.83 ± 12.43 (10+3 psi)
Phi = 0.0°
d-spacing (Å)
sin ² (Psi)

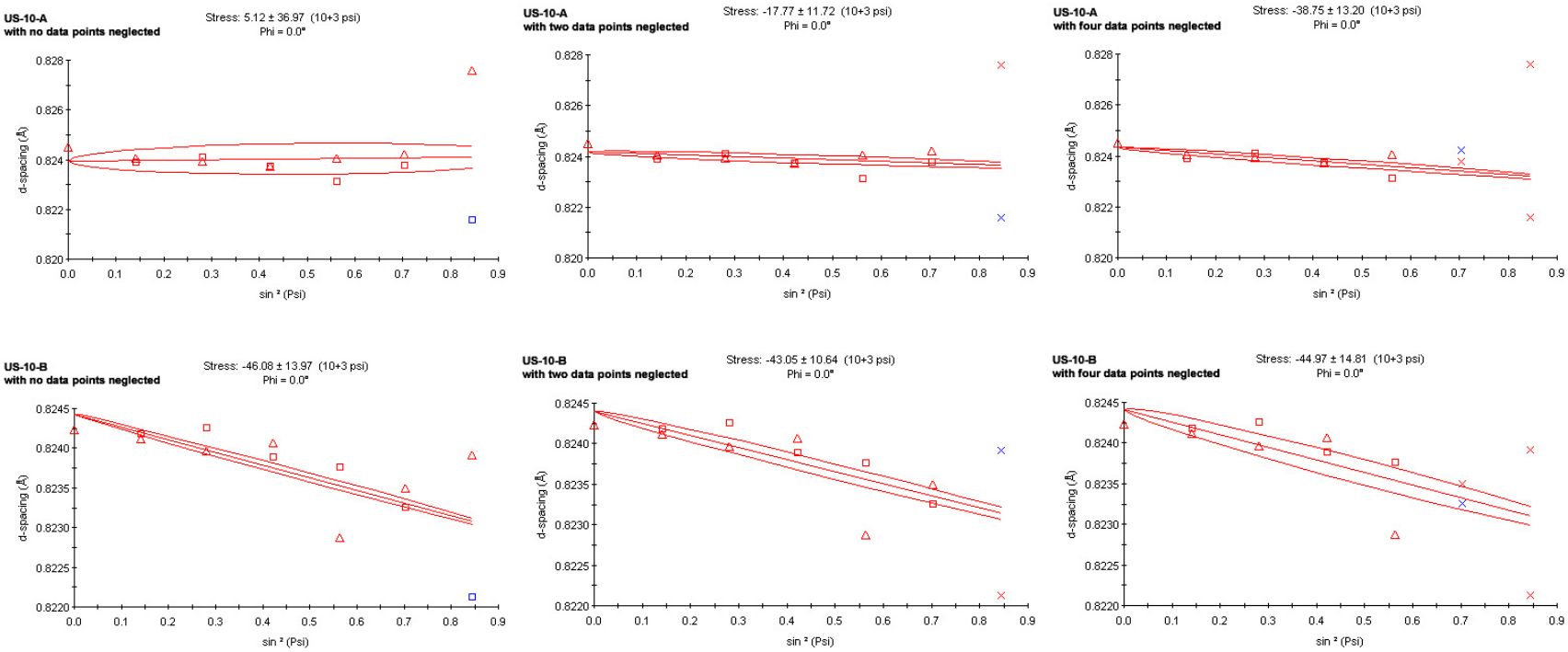

Figure 21: *d* versus $\sin^2\psi$ curves of unblasted samples.

The stress results from all analysis are summarized in Table 4.

Table 4: Summary of XRD stress results for unblasted samples.

Sample no.	Location				σ_ϕ (ksi)	σ_ϕ StdDev (ksi)
	No.	# data pts. neglected	x (in.)	y (in.)		
US1	A	0	3.250	0.500	-40.28	13.83
		2			-30.44	18.15
		4			-47.11	12.96
	B	0	4.125	0.500	-14.29	26.93
		2			-36.46	7.88
		4			-48.59	9.22
US2	A	0	3.250	0.500	-60.17	24.79
		2			-41.68	11.55
		4			-48.48	12.83
	B	0	4.125	0.500	-25.44	17.18
		2			-46.28	19.13
		4			-39.31	8.27
US3	A	0	3.250	0.500	-49.01	21.59
		2			-46.18	24.19
		4			-45.46	31.78
	B	0	4.125	0.500	-59.63	14.60
		2			-39.32	11.29
		4			-26.30	9.88
US4	A	0	3.250	0.500	-16.93	10.46
		2			-23.18	12.22
		4			-44.22	4.26
	B	0	4.125	0.500	-8.85	35.90
		2			-30.31	13.91
		4			-20.09	15.24
US5	A	0	3.250	0.500	62.76	27.02
		2			57.94	18.26
		4			18.71	16.57
	B	0	4.125	0.500	36.53	8.06
		2			46.06	8.72
		4			39.95	12.77
US6	A	0	3.250	0.500	-2.34	15.83
		2			7.38	16.59
		4			-1.77	24.41
	B	0	4.125	0.500	-49.86	12.34
		2			-36.27	13.87
		4			-41.21	16.21
US7	A	0	3.250	0.500	1.08	18.69
		2			-19.73	11.55
		4			-29.64	10.68
	B	0	4.125	0.500	59.50	33.42
		2			-3.50	8.20
		4			-9.86	11.87
US8	A	0	3.250	0.500	-72.80	17.92
		2			-44.34	13.12
		4			-9.32	1.46
	B	0	4.125	0.500	-16.38	19.45
		2			-37.69	8.17
		4			-36.40	7.10
US9	A	0	3.250	0.500	9.78	18.61
		2			-12.49	8.58
		4			-15.47	12.98
	B	0	4.125	0.500	-17.99	27.26
		2			-55.83	12.58
		4			-31.83	12.43
US10	A	0	3.250	0.500	5.12	36.97
		2			-17.77	11.72
		4			-38.75	13.20
	B	0	4.125	0.500	-46.08	13.97
		2			-43.05	10.64
		4			-44.97	14.81

Note: Numbers in blue are stress values with neglecting data points of psi = ±66.75°
Numbers in pink are stress values with neglecting data points of psi = ±66.75°, ±57.01°

Figure 21 and Table 4 demonstrate that by neglecting several "bad" data points on the *d* vs. $\sin^2\psi$ curves, standard deviations can generally be reduced.

The results above also show that residual stress varied along the length of sample. Although points A and B were not that far apart from each other, there generally seemed to be quite a variation in stress between these two points. The actual state of stress of the samples was unknown. However, these X-ray diffraction measurement results were verified by the ESPI hole drilling method, and will be discussed in Section 6.4.1.

6.1.2 Sandblasted Samples

Figure 22 shows three- *d* vs. $\sin^2\psi$ curves for each X-ray diffraction measurement of the sandblasted samples.

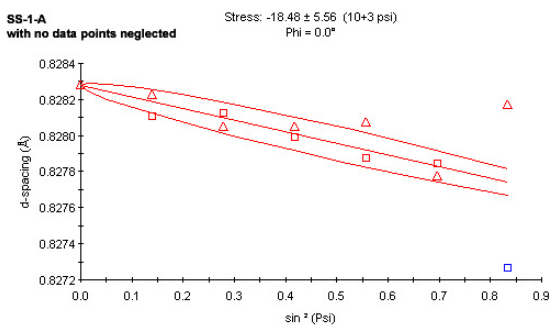
SS-1-A
with no data points neglected
Stress: -18.48 ± 5.56 (10+3 psi)
Phi = 0.0°
d-spacing (Å)
sin ² (Psi)

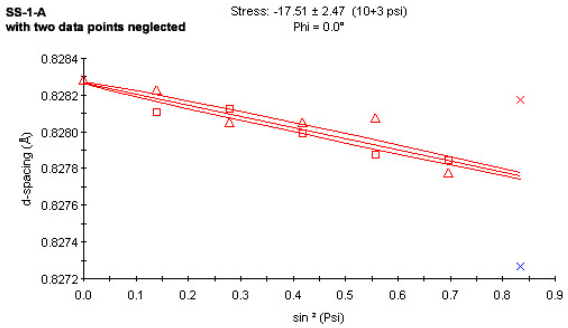
SS-1-A
with two data points neglected
Stress: -17.51 ± 2.47 (10+3 psi)
Phi = 0.0°
d-spacing (Å)
sin ² (Psi)

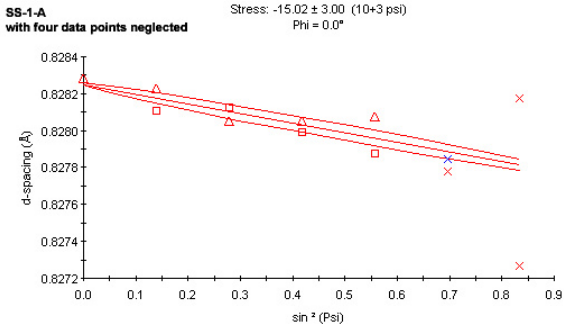
SS-1-A
with four data points neglected
Stress: -15.02 ± 3.00 (10+3 psi)
Phi = 0.0°
d-spacing (Å)
sin ² (Psi)

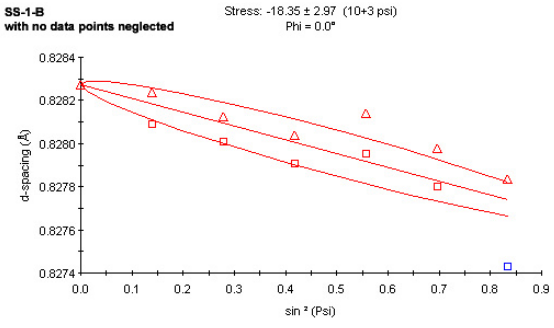
SS-1-B
with no data points neglected
Stress: -18.35 ± 2.97 (10+3 psi)
Phi = 0.0°
d-spacing (Å)
sin ² (Psi)

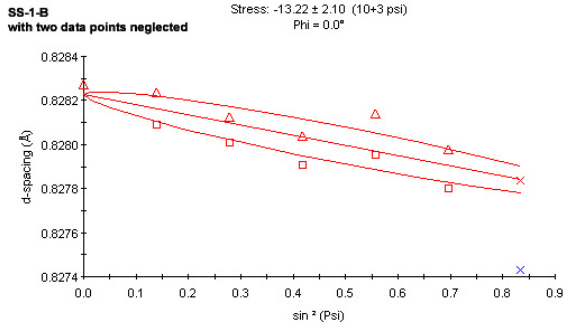
SS-1-B
with two data points neglected
Stress: -13.22 ± 2.10 (10+3 psi)
Phi = 0.0°
d-spacing (Å)
sin ² (Psi)

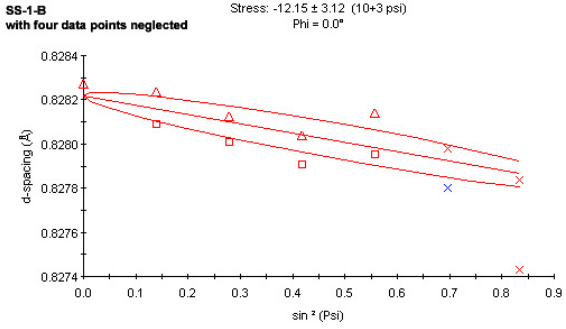
SS-1-B
with four data points neglected
Stress: -12.15 ± 3.12 (10+3 psi)
Phi = 0.0°
d-spacing (Å)
sin ² (Psi)

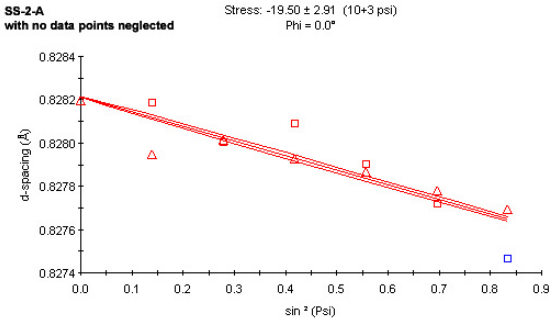
SS-2-A
with no data points neglected
Stress: -19.50 ± 2.91 (10+3 psi)
Phi = 0.0°
d-spacing (Å)
sin ² (Psi)

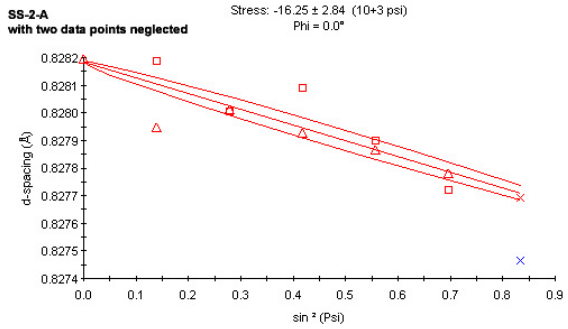
SS-2-A
with two data points neglected
Stress: -16.25 ± 2.84 (10+3 psi)
Phi = 0.0°
d-spacing (Å)
sin ² (Psi)

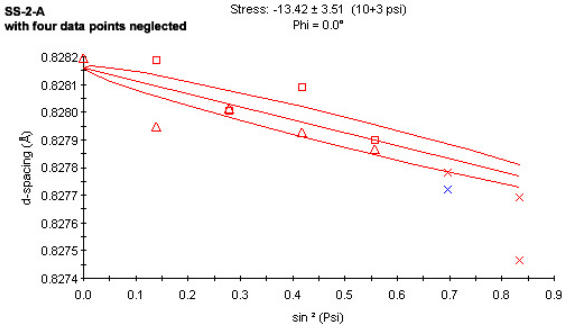
SS-2-A
with four data points neglected
Stress: -13.42 ± 3.51 (10+3 psi)
Phi = 0.0°
d-spacing (Å)
sin ² (Psi)

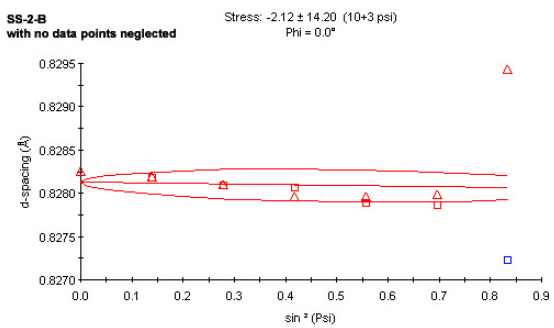
SS-2-B
with no data points neglected
Stress: -2.12 ± 14.20 (10+3 psi)
Phi = 0.0°
d-spacing (Å)
sin ² (Psi)

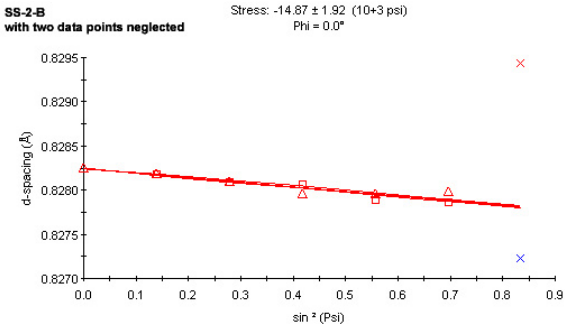
SS-2-B
with two data points neglected
Stress: -14.87 ± 1.92 (10+3 psi)
Phi = 0.0°
d-spacing (Å)
sin ² (Psi)

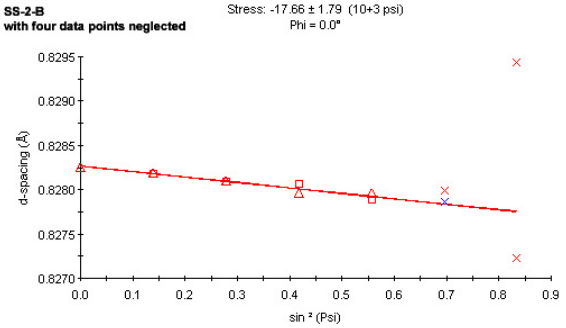
SS-2-B
with four data points neglected
Stress: -17.66 ± 1.79 (10+3 psi)
Phi = 0.0°
d-spacing (Å)
sin ² (Psi)

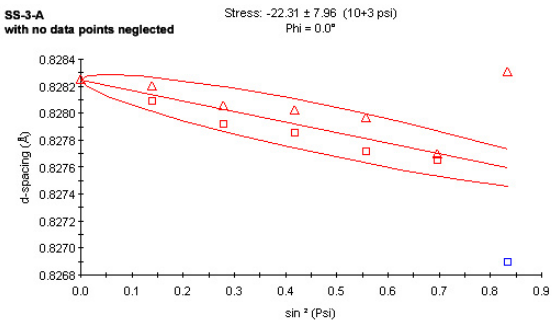
SS-3-A
with no data points neglected
Stress: -22.31 ± 7.96 (10+3 psi)
Phi = 0.0°
d-spacing (Å)
sin ² (Psi)

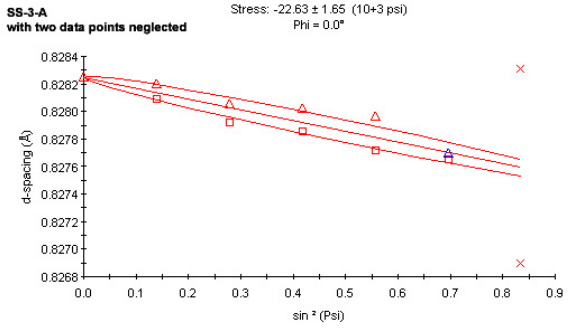
SS-3-A
with two data points neglected
Stress: -22.63 ± 1.65 (10+3 psi)
Phi = 0.0°
d-spacing (Å)
sin ² (Psi)

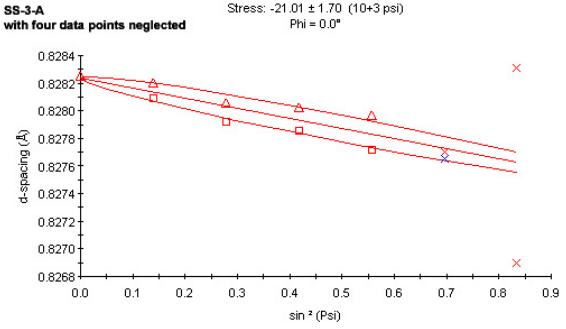
SS-3-A
with four data points neglected
Stress: -21.01 ± 1.70 (10+3 psi)
Phi = 0.0°
d-spacing (Å)
sin ² (Psi)

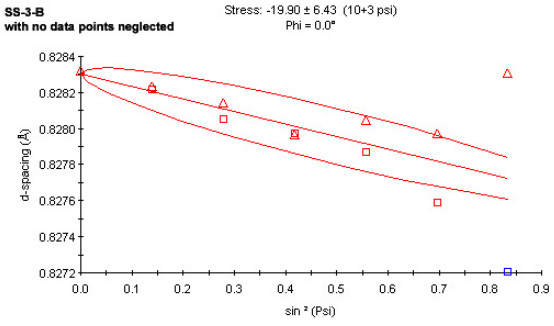
SS-3-B
with no data points neglected
Stress: -19.90 ± 6.43 (10+3 psi)
Phi = 0.0°
d-spacing (Å)
sin ² (Psi)

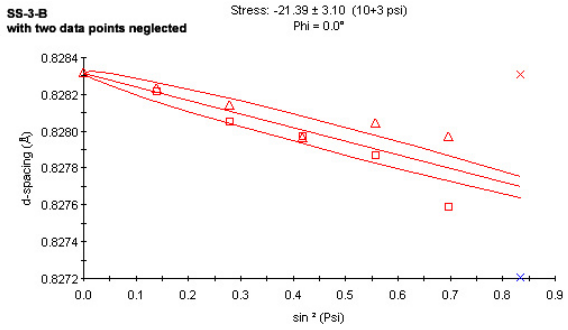
SS-3-B
with two data points neglected
Stress: -21.39 ± 3.10 (10+3 psi)
Phi = 0.0°
d-spacing (Å)
sin ² (Psi)

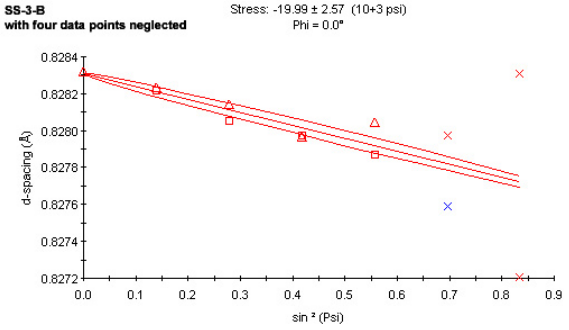
SS-3-B
with four data points neglected
Stress: -19.99 ± 2.57 (10+3 psi)
Phi = 0.0°
d-spacing (Å)
sin ² (Psi)

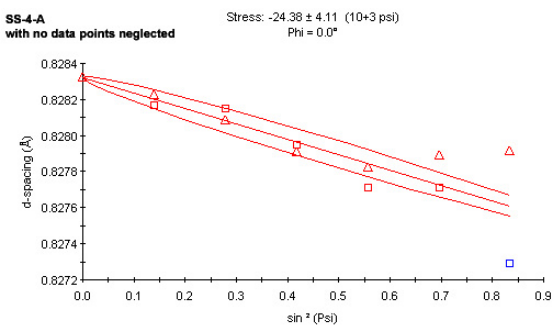
SS-4-A
with no data points neglected
Stress: -24.38 ± 4.11 (10+3 psi)
Phi = 0.0°
d-spacing (Å)
sin ² (Psi)

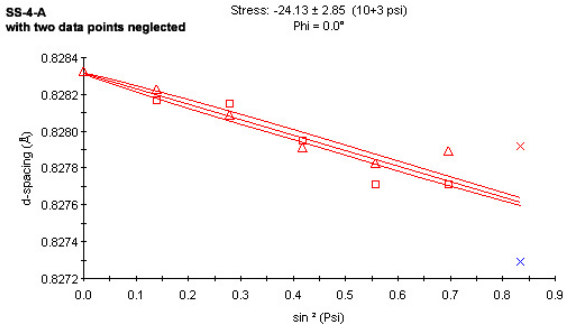
SS-4-A
with two data points neglected
Stress: -24.13 ± 2.85 (10+3 psi)
Phi = 0.0°
d-spacing (Å)
sin ² (Psi)

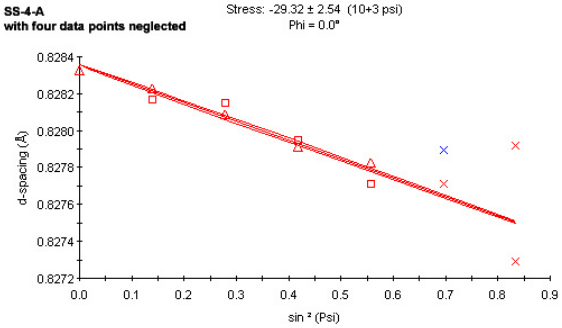
SS-4-A
with four data points neglected
Stress: -29.32 ± 2.54 (10+3 psi)
Phi = 0.0°
d-spacing (Å)
sin ² (Psi)

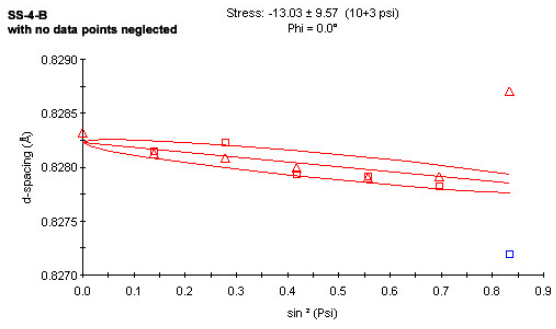
SS-4-B
with no data points neglected
Stress: -13.03 ± 9.57 (10+3 psi)
Phi = 0.0°
d-spacing (Å)
sin ² (Psi)

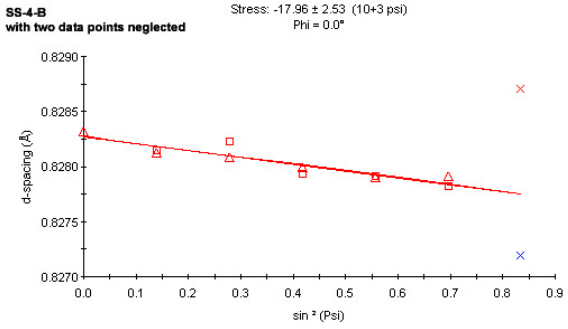
SS-4-B
with two data points neglected
Stress: -17.96 ± 2.53 (10+3 psi)
Phi = 0.0°
d-spacing (Å)
sin ² (Psi)

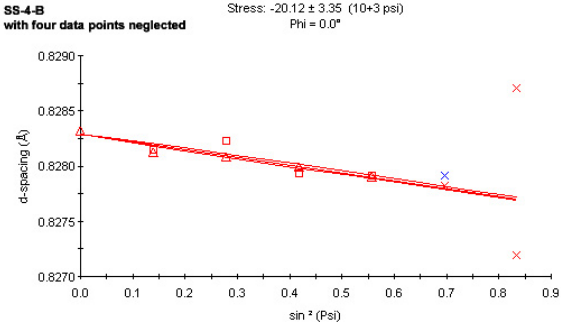
SS-4-B
with four data points neglected
Stress: -20.12 ± 3.35 (10+3 psi)
Phi = 0.0°
d-spacing (Å)
sin ² (Psi)

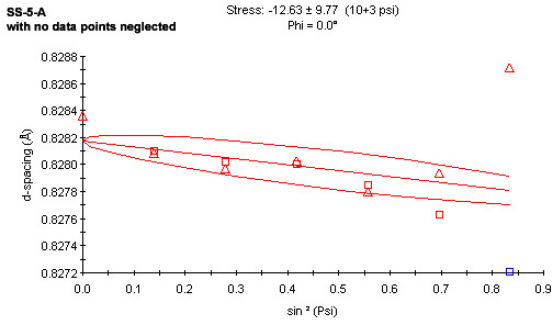
SS-5-A
with no data points neglected
Stress: -12.63 ± 9.77 (10+3 psi)
Phi = 0.0°
d-spacing (Å)
sin ² (Psi)

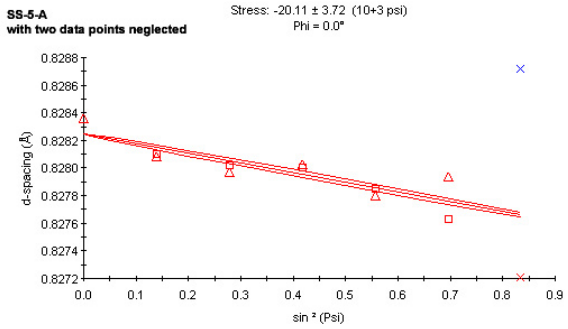
SS-5-A
with two data points neglected
Stress: -20.11 ± 3.72 (10+3 psi)
Phi = 0.0°
d-spacing (Å)
sin ² (Psi)

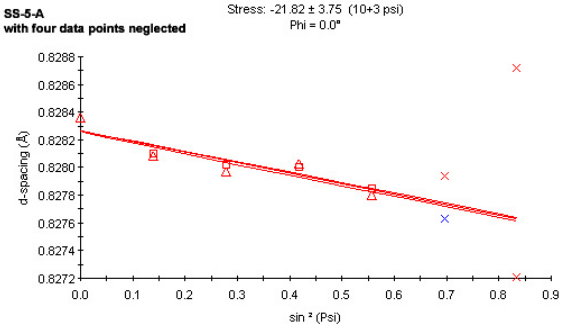
SS-5-A
with four data points neglected
Stress: -21.82 ± 3.75 (10+3 psi)
Phi = 0.0°
d-spacing (Å)
sin ² (Psi)

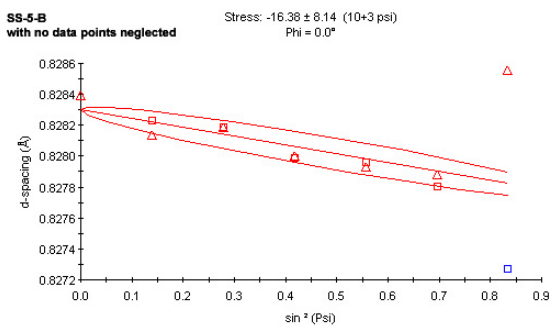
SS-5-B
with no data points neglected
Stress: -16.38 ± 8.14 (10+3 psi)
Phi = 0.0°
d-spacing (Å)
sin ² (Psi)

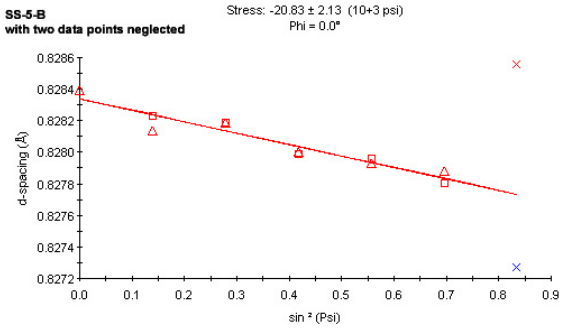
SS-5-B
with two data points neglected
Stress: -20.83 ± 2.13 (10+3 psi)
Phi = 0.0°
d-spacing (Å)
sin ² (Psi)

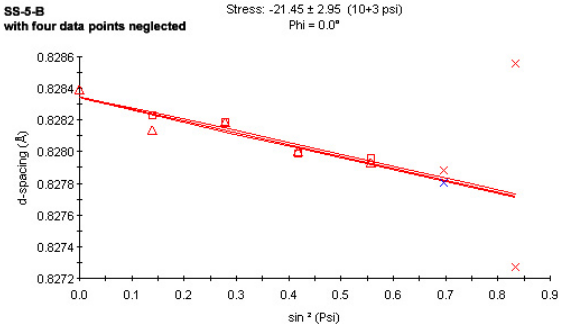
SS-5-B
with four data points neglected
Stress: -21.45 ± 2.95 (10+3 psi)
Phi = 0.0°
d-spacing (Å)
sin ² (Psi)

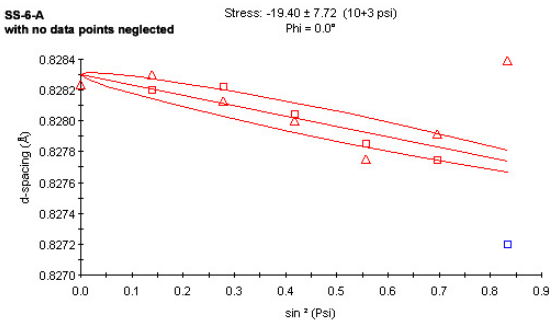
SS-6-A
with no data points neglected
Stress: -19.40 ± 7.72 (10+3 psi)
Phi = 0.0°
d-spacing (Å)
sin ² (Psi)

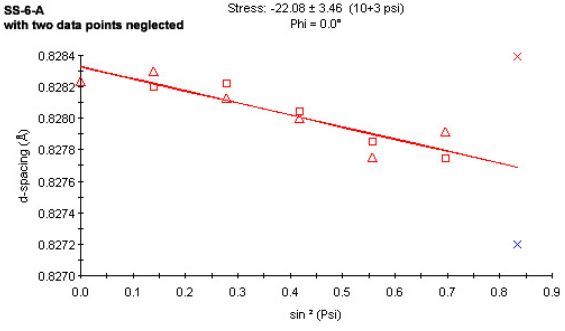
SS-6-A
with two data points neglected
Stress: -22.08 ± 3.46 (10+3 psi)
Phi = 0.0°
d-spacing (Å)
sin ² (Psi)

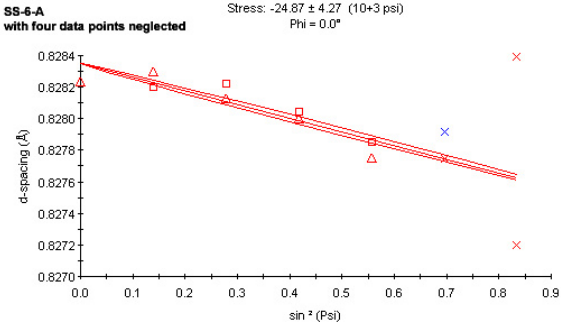
SS-6-A
with four data points neglected
Stress: -24.87 ± 4.27 (10+3 psi)
Phi = 0.0°
d-spacing (Å)
sin ² (Psi)

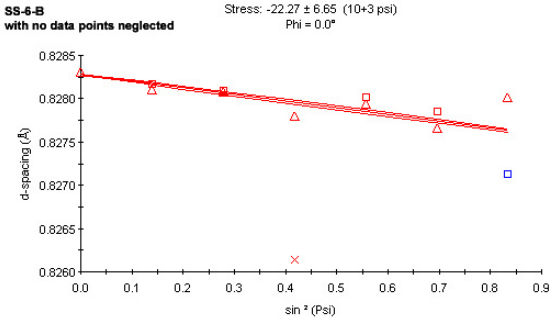
SS-6-B
with no data points neglected
Stress: -22.27 ± 6.65 (10+3 psi)
Phi = 0.0°
d-spacing (Å)
sin ² (Psi)

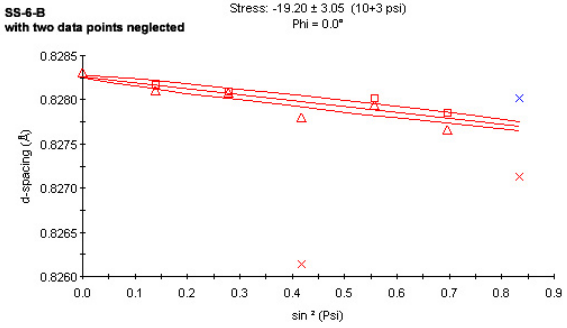
SS-6-B
with two data points neglected
Stress: -19.20 ± 3.05 (10+3 psi)
Phi = 0.0°
d-spacing (Å)
sin ² (Psi)

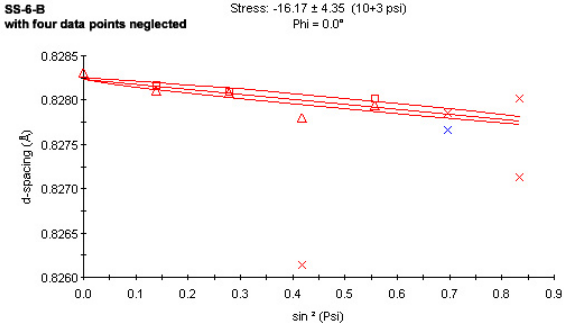
SS-6-B
with four data points neglected
Stress: -16.17 ± 4.35 (10+3 psi)
Phi = 0.0°
d-spacing (Å)
sin ² (Psi)

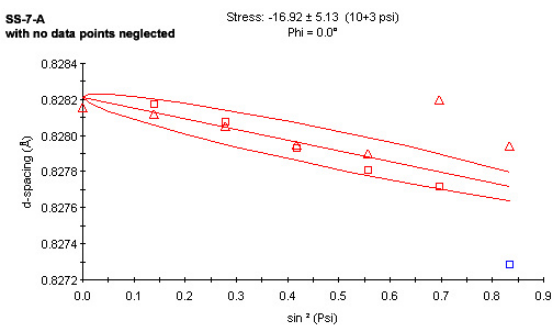
SS-7-A
with no data points neglected
Stress: -16.92 ± 5.13 (10+3 psi)
Phi = 0.0°
d-spacing (Å)
sin ² (Psi)

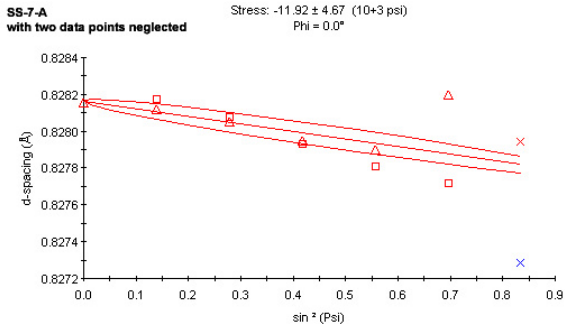
SS-7-A
with two data points neglected
Stress: -11.92 ± 4.67 (10+3 psi)
Phi = 0.0°
d-spacing (Å)
sin ² (Psi)

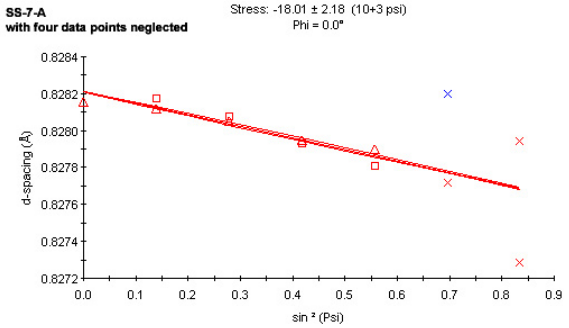
SS-7-A
with four data points neglected
Stress: -18.01 ± 2.18 (10+3 psi)
Phi = 0.0°
d-spacing (Å)
sin ² (Psi)

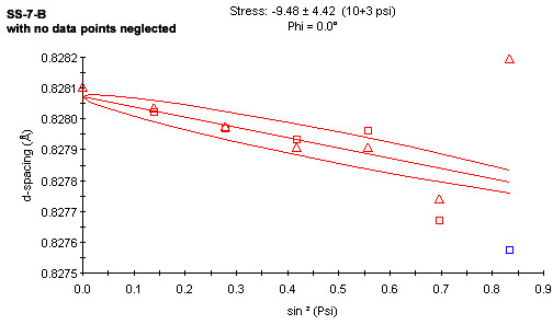
SS-7-B
with no data points neglected
Stress: -9.48 ± 4.42 (10+3 psi)
Phi = 0.0°
d-spacing (Å)
sin ² (Psi)

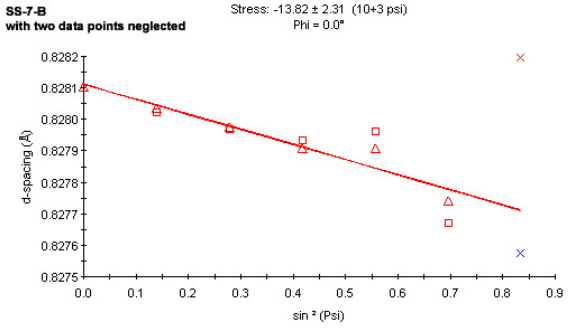
SS-7-B
with two data points neglected
Stress: -13.82 ± 2.31 (10+3 psi)
Phi = 0.0°
d-spacing (Å)
sin ² (Psi)

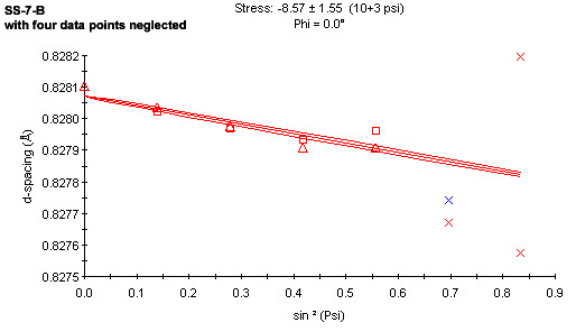
SS-7-B
with four data points neglected
Stress: -8.57 ± 1.55 (10+3 psi)
Phi = 0.0°
d-spacing (Å)
sin ² (Psi)

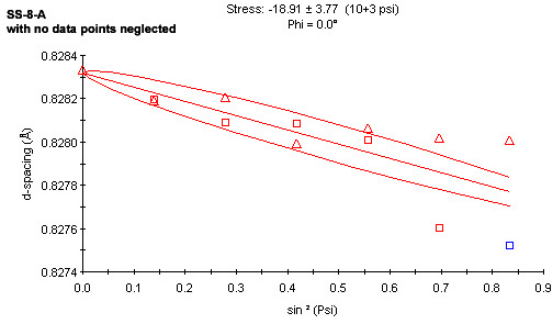
SS-8-A
with no data points neglected
Stress: -18.91 ± 3.77 (10+3 psi)
Phi = 0.0°
d-spacing (Å)
sin ² (Psi)

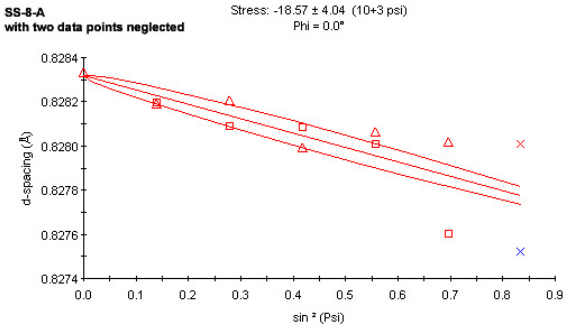
SS-8-A
with two data points neglected
Stress: -18.57 ± 4.04 (10+3 psi)
Phi = 0.0°
d-spacing (Å)
sin ² (Psi)

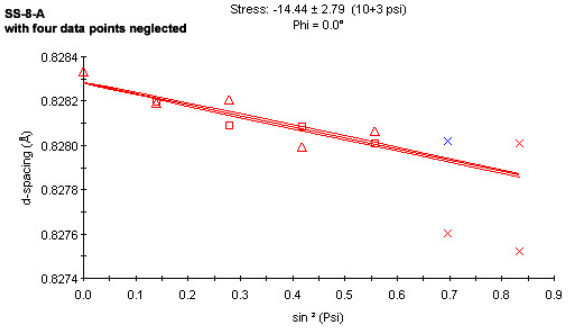
SS-8-A
with four data points neglected
Stress: -14.44 ± 2.79 (10+3 psi)
Phi = 0.0°
d-spacing (Å)
sin ² (Psi)

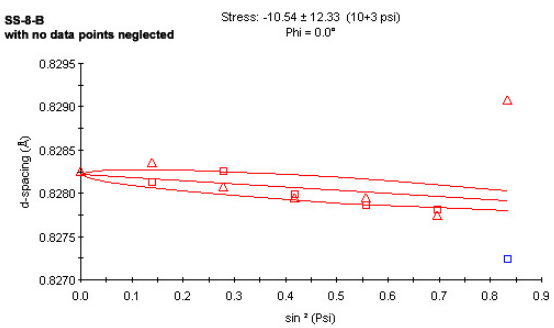
SS-8-B
with no data points neglected
Stress: -10.54 ± 12.33 (10+3 psi)
Phi = 0.0°
d-spacing (Å)
sin ² (Psi)

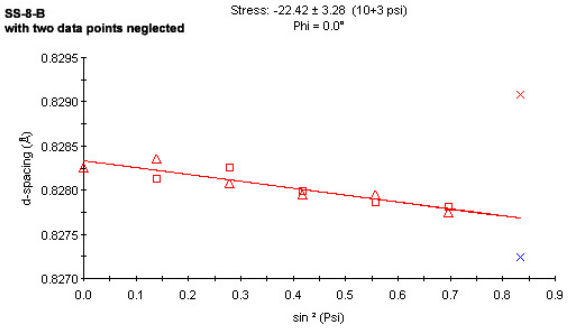
SS-8-B
with two data points neglected
Stress: -22.42 ± 3.28 (10+3 psi)
Phi = 0.0°
d-spacing (Å)
sin ² (Psi)

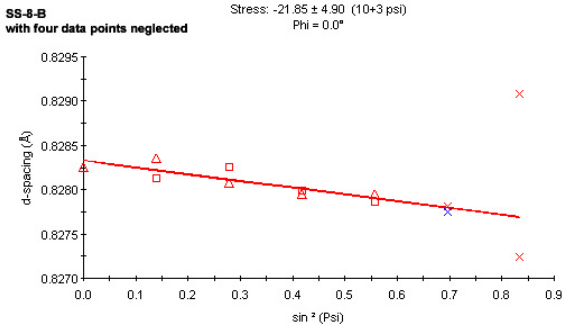
SS-8-B
with four data points neglected
Stress: -21.85 ± 4.90 (10+3 psi)
Phi = 0.0°
d-spacing (Å)
sin ² (Psi)

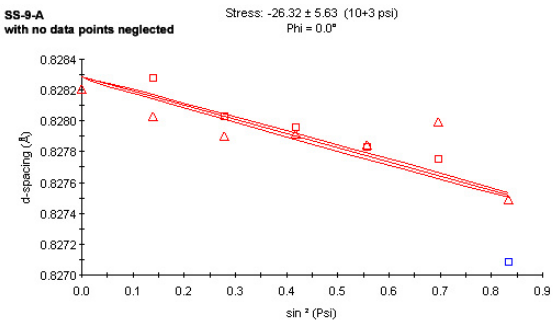
SS-9-A
with no data points neglected
Stress: -26.32 ± 5.63 (10+3 psi)
Phi = 0.0°
d-spacing (Å)
sin ² (Psi)

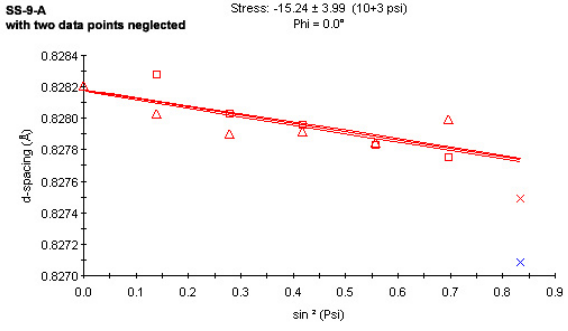
SS-9-A
with two data points neglected
Stress: -15.24 ± 3.99 (10+3 psi)
Phi = 0.0°
d-spacing (Å)
sin ² (Psi)

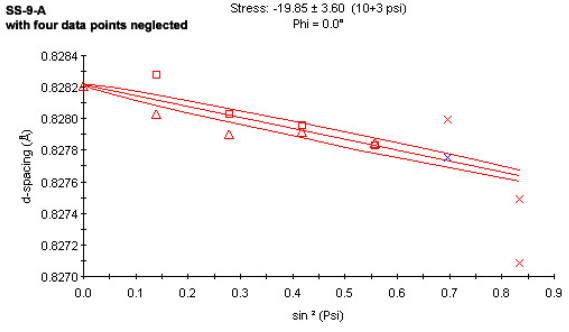
SS-9-A
with four data points neglected
Stress: -19.85 ± 3.60 (10+3 psi)
Phi = 0.0°
d-spacing (Å)
sin ² (Psi)

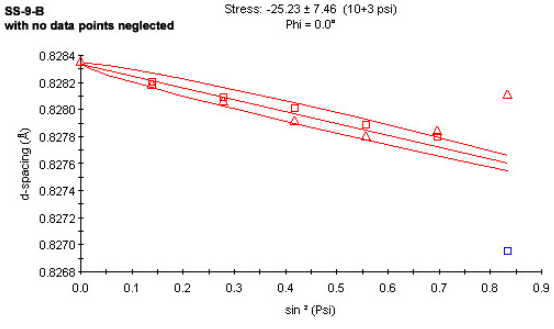
SS-9-B
with no data points neglected
Stress: -25.23 ± 7.46 (10+3 psi)
Phi = 0.0°
d-spacing (Å)
sin ² (Psi)

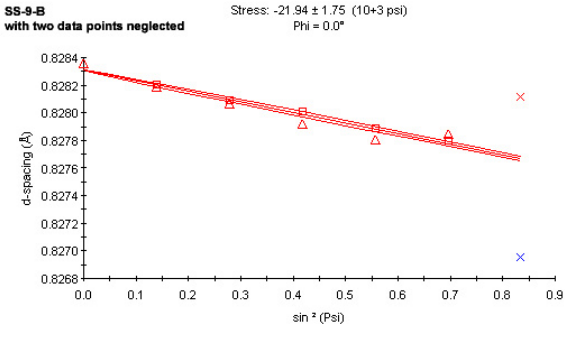
SS-9-B
with two data points neglected
Stress: -21.94 ± 1.75 (10+3 psi)
Phi = 0.0°
d-spacing (Å)
sin ² (Psi)

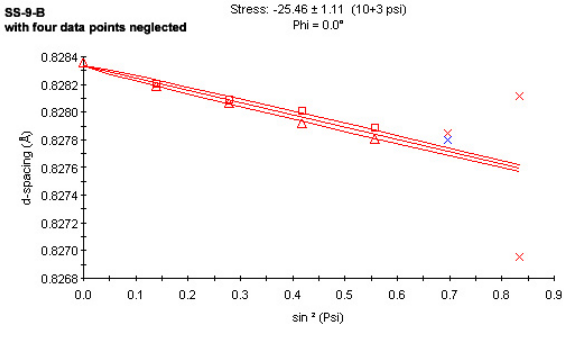
SS-9-B
with four data points neglected
Stress: -25.46 ± 1.11 (10+3 psi)
Phi = 0.0°
d-spacing (Å)
sin ² (Psi)

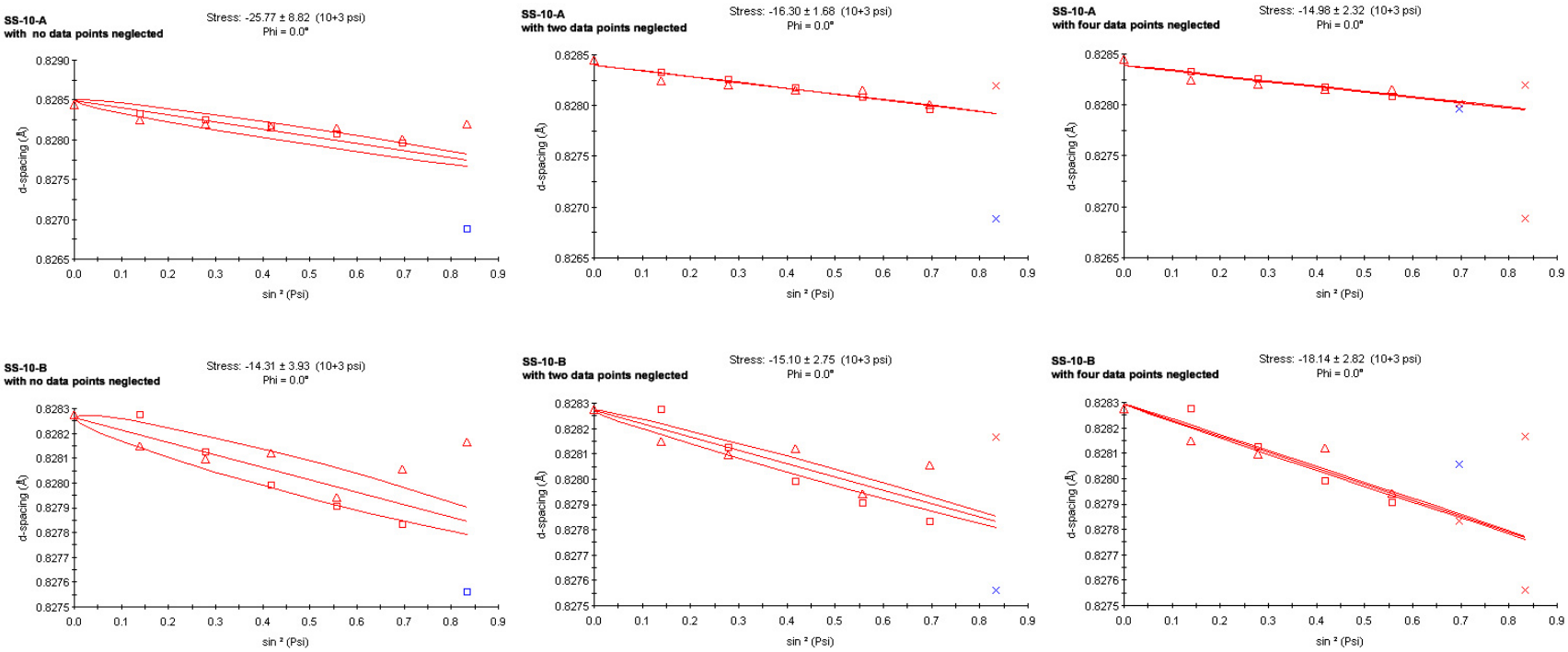

Figure 22: d versus $\sin^2\psi$ curves of sandblasted samples.

The stress results from all analysis are summarized in Table 5.

Table 5: Summary of XRD stress results for sandblasted samples.

Sample	Location				σ_ϕ (ksi)	σ_ϕ StdDev (ksi)
	No.	# data pts. neglected	x (in.)	y (in.)		
SS1	A	0	3.250	0.500	-18.48	5.56
		2			-17.51	2.47
		4			-15.02	3.00
	B	0	4.125	0.500	-18.35	2.97
		2			-13.22	2.10
		4			-12.15	3.12
SS2	A	0	3.250	0.500	-19.50	2.91
		2			-16.25	2.84
		4			-13.42	3.51
	B	0	4.125	0.500	-2.12	14.20
		2			-14.87	1.92
		4			-17.66	1.79
SS3	A	0	3.250	0.500	-22.31	7.96
		2			-22.63	1.65
		4			-21.01	1.70
	B	0	4.125	0.500	-19.90	6.43
		2			-21.39	3.10
		4			-19.99	2.57
SS4	A	0	3.250	0.500	-24.38	4.11
		2			-24.13	2.85
		4			-29.32	2.54
	B	0	4.125	0.500	-13.03	9.57
		2			-17.96	2.53
		4			-20.12	3.35
SS5	A	0	3.250	0.500	-12.63	9.77
		2			-20.11	3.72
		4			-21.82	3.75
	B	0	4.125	0.500	-16.38	8.14
		2			-20.83	2.13
		4			-21.45	2.95

Sample no.	Location				σ_ϕ (ksi)	σ_ϕ StdDev (ksi)
	No.	# data pts. neglected	x (in.)	y (in.)		
SS6	A	0	3.250	0.500	-19.40	7.72
		2			-22.08	3.46
		4			-24.87	4.27
	B	0	4.125	0.500	-22.27	6.65
		2			-19.20	3.05
		4			-16.17	4.35
SS7	A	0	3.250	0.500	-16.92	5.13
		2			-11.92	4.67
		4			-18.01	2.18
	B	0	4.125	0.500	-9.48	4.42
		2			-13.82	2.31
		4			-8.57	1.55
SS8	A	0	3.250	0.500	-18.91	3.77
		2			-18.57	4.04
		4			-14.44	2.79
	B	0	4.125	0.500	-10.54	12.33
		2			-22.42	3.28
		4			-21.85	4.90
SS9	A	0	3.250	0.500	-26.32	5.63
		2			-15.24	3.99
		4			-19.85	3.60
	B	0	4.125	0.500	-25.23	7.46
		2			-21.94	1.75
		4			-25.46	1.11
SS10	A	0	3.250	0.500	-25.77	8.82
		2			-16.30	1.68
		4			-14.98	2.32
	B	0	4.125	0.500	-14.31	3.93
		2			-15.10	2.75
		4			-18.14	2.82

Note: Numbers in blue are stress values with neglecting data points of psi = ±66.00°
Numbers in pink are stress values with neglecting data points of psi = ±66.00°, ±56.51°

Figure 22 and Table 5 demonstrate that by neglecting several "bad" data points on the *d* vs. $\sin^2\psi$ curves, standard deviations can generally be reduced.

The results above also show that residual stresses were quite uniform along the length of sample. Generally, there was not much variation between the residual stress values of points A and B. The actual state of stress of the samples was unknown. However, these X-ray diffraction measurement results were verified by the ESPI hole drilling method, and will be discussed in Section 6.4.2.

6.1.3 Discussions

The stress analyses of the sandblasted samples yielded lower standard deviations than the unblasted samples. In addition, the unblasted samples generally had higher compressive stresses than the sandblasted samples. One possible reason is that before the plate was cut into the samples, it may have undergone some type of cold leveling to flatten its surface, and therefore compressive residual stresses close to the surface were induced. Other possible reasons include the presence of mill scale in the unblasted specimens, as well as the fluorescence produced by the atoms that absorb the energy from the K-α_1 component of the incident beam. As discussed in Section 2.3, the use of a chromium anode, instead of copper, is recommended for iron samples. The reason is that a chromium anode has a longer wavelength compared to copper. As a result, its radiation will not have sufficient energy to cause fluorescence. The less energetic chromium anode also penetrates further into the material compared to the more energetic copper anode. While a Cr-Kα anode penetrates to about 3.9-4.7 μm into a material, a Cu-Kα anode only penetrates to about 1.5-1.9 μm [8].

6.2 STRAIN-GAGE HOLE DRILLING METHOD

For each sample tested, one strain-gage hole drilling measurement was taken along the centerline. The location was at a distance of 3.250 in. from one end of the sample, which is the same exact location as point A, as described in Section 6.1. Identical to the X-ray diffraction method, all unblasted samples start with the prefix 'US', and all sandblasted samples start with the prefix 'SS'. Stresses were calculated from the strain readings using the integral method (using H-DRILL software, developed by G. Schajer), as described in Section 3.2.2. The integral method was chosen over the other analysis methods because the stress fields within the material tested were highly non-uniform, for both the unblasted and the sandblasted samples. Once the state of stress was calculated for each measurement, graphs of σ_{xx}, σ_{yy}, and τ_{xy}, versus depth were then plotted for both types of samples.

6.2.1 Unblasted Samples

Plots of σ_{xx}, σ_{yy}, and τ_{xy}, versus depth for strain-gage hole drilling measurements of the unblasted samples are shown by Figures 23-25 below.

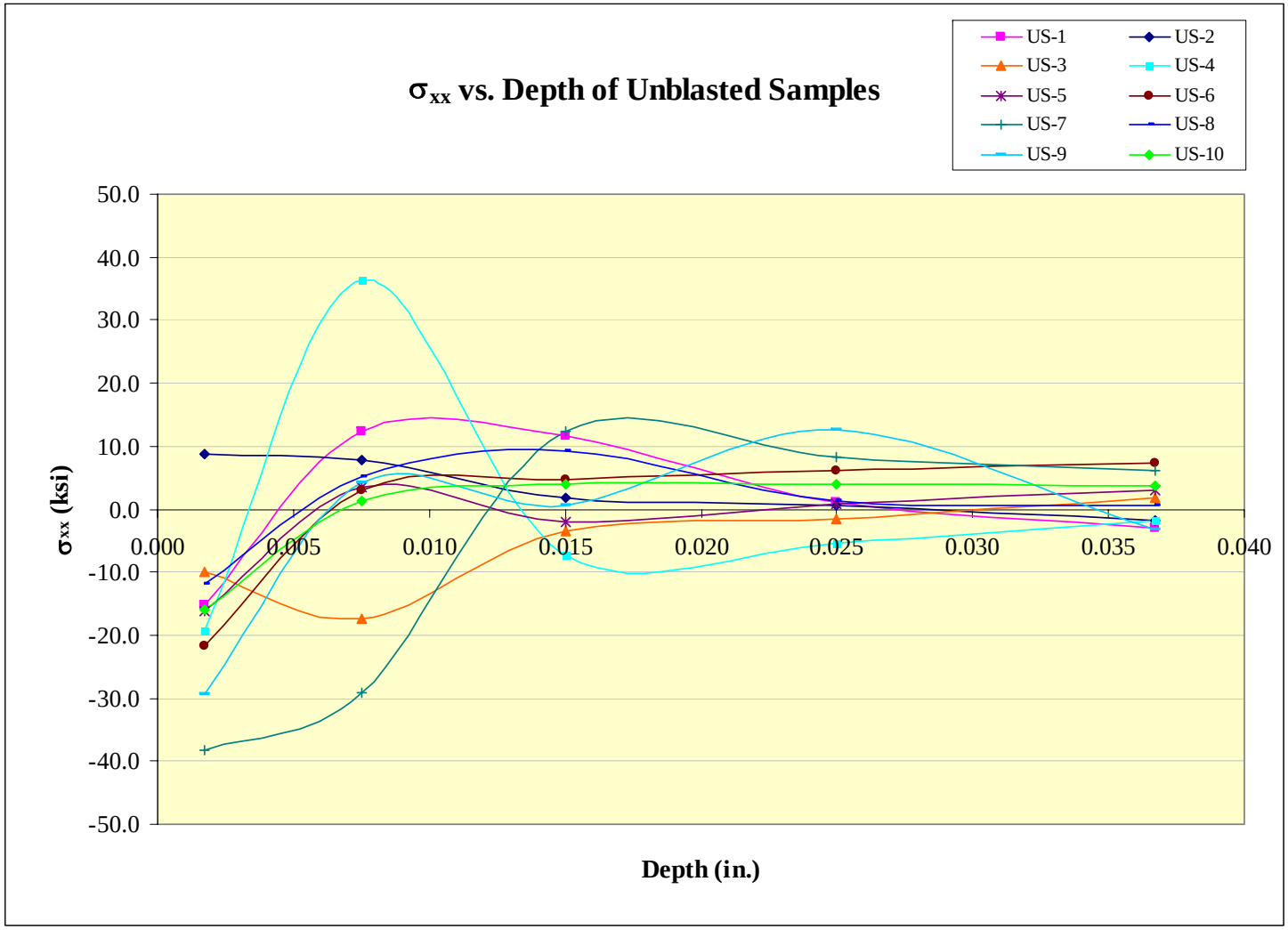

Figure 23: σ_{xx} versus depth curves of unblasted samples – SGHD method.

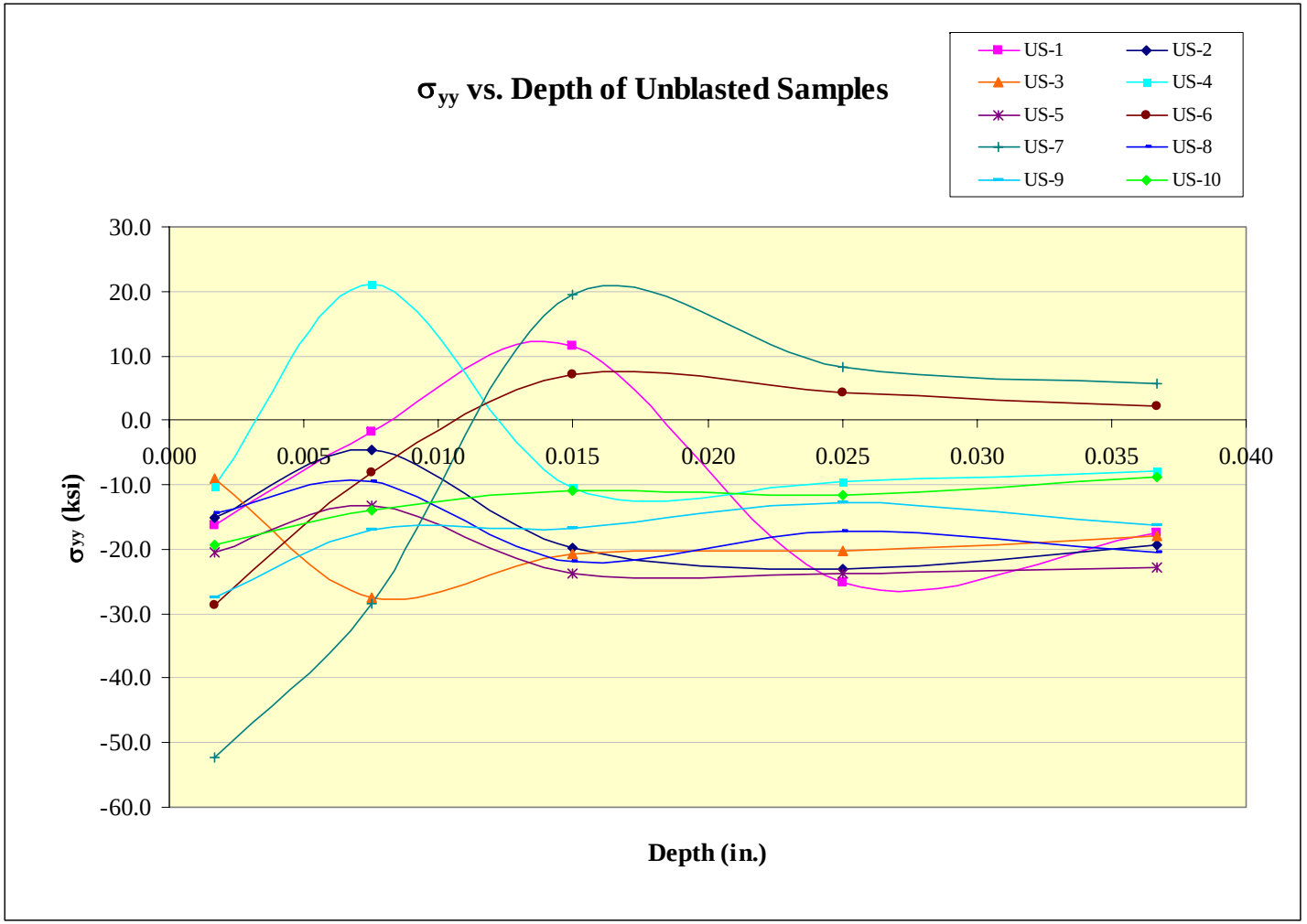

Figure 24: σ_{yy} versus depth curves of unblasted samples – SGHD method.

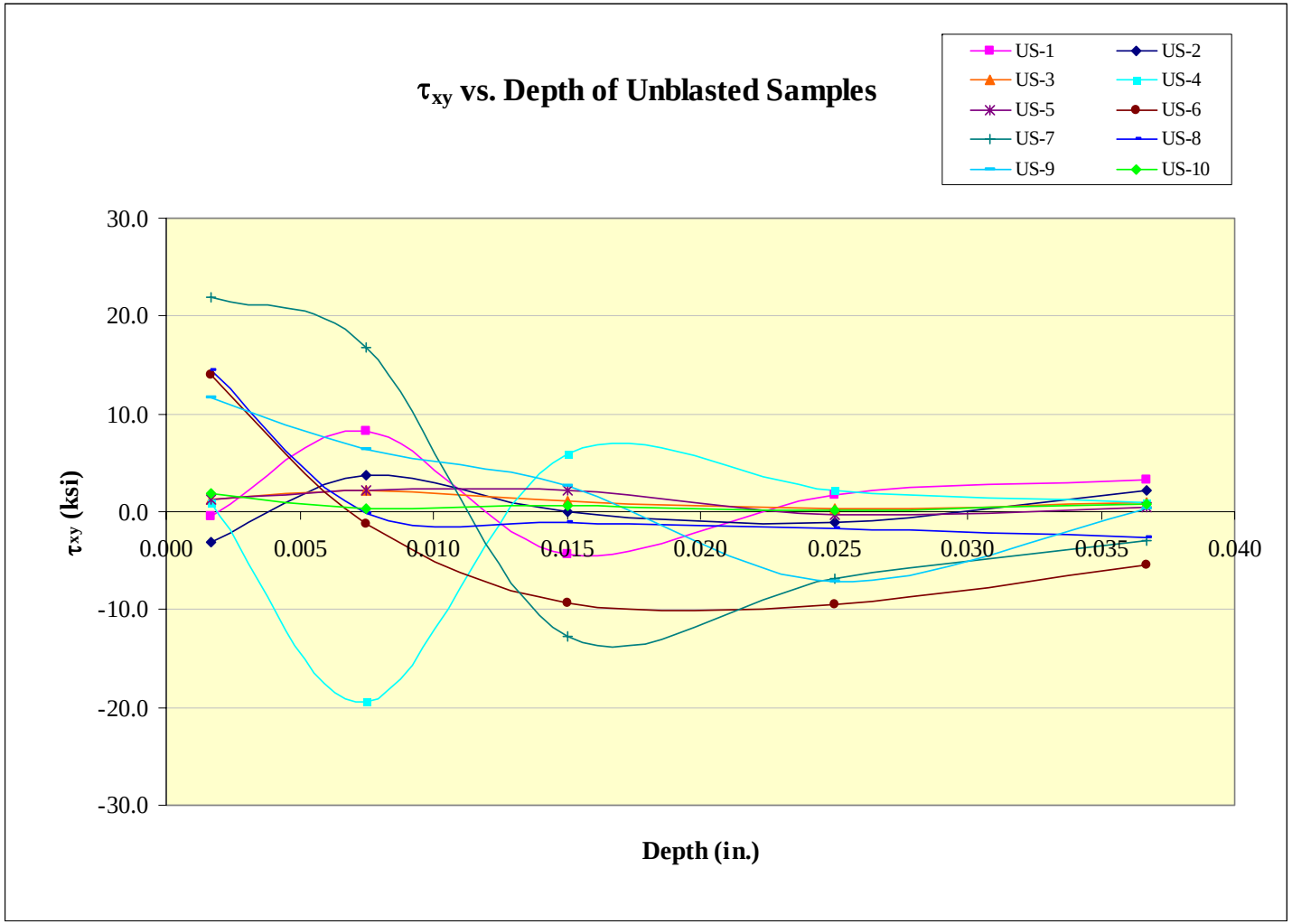

Figure 25: τ_{xy} versus depth curves of unblasted samples – SGHD method.

Referring to Figure 23, the value of σ_{xx} for most samples was compressive closer to the surface, and became tensile at depths of 0.003 – 0.007 in. from the surface. It can also be observed that most of the unblasted samples have similar σ_{xx} profiles. Stresses started off as compressive close to the surface, and then became tensile or fairly close to zero as depth increased. For most samples, stress values also became constant below depth of 0.015 in.

Figure 24 also shows that the unblasted samples had similar σ_{yy} profiles in general. Unlike σ_{xx}, the σ_{yy} values stayed compressive as depth increased for most samples. The graph demonstrates that compressive stress value decreased up to a depth of 0.0075 in., and then increased with depth. The compressive stress values also became constant starting at a depth of 0.015 in.

Figure 25 illustrates that the amount of shear stress (τ_{xy}) present in the unblasted samples was generally very small. The magnitude was about constant throughout the whole depth.

6.2.2 Sandblasted Samples

Plots of σ_{xx}, σ_{yy}, and τ_{xy}, versus depth for strain-gage hole drilling measurements of the sandblasted samples are shown by Figures 26-28 below.

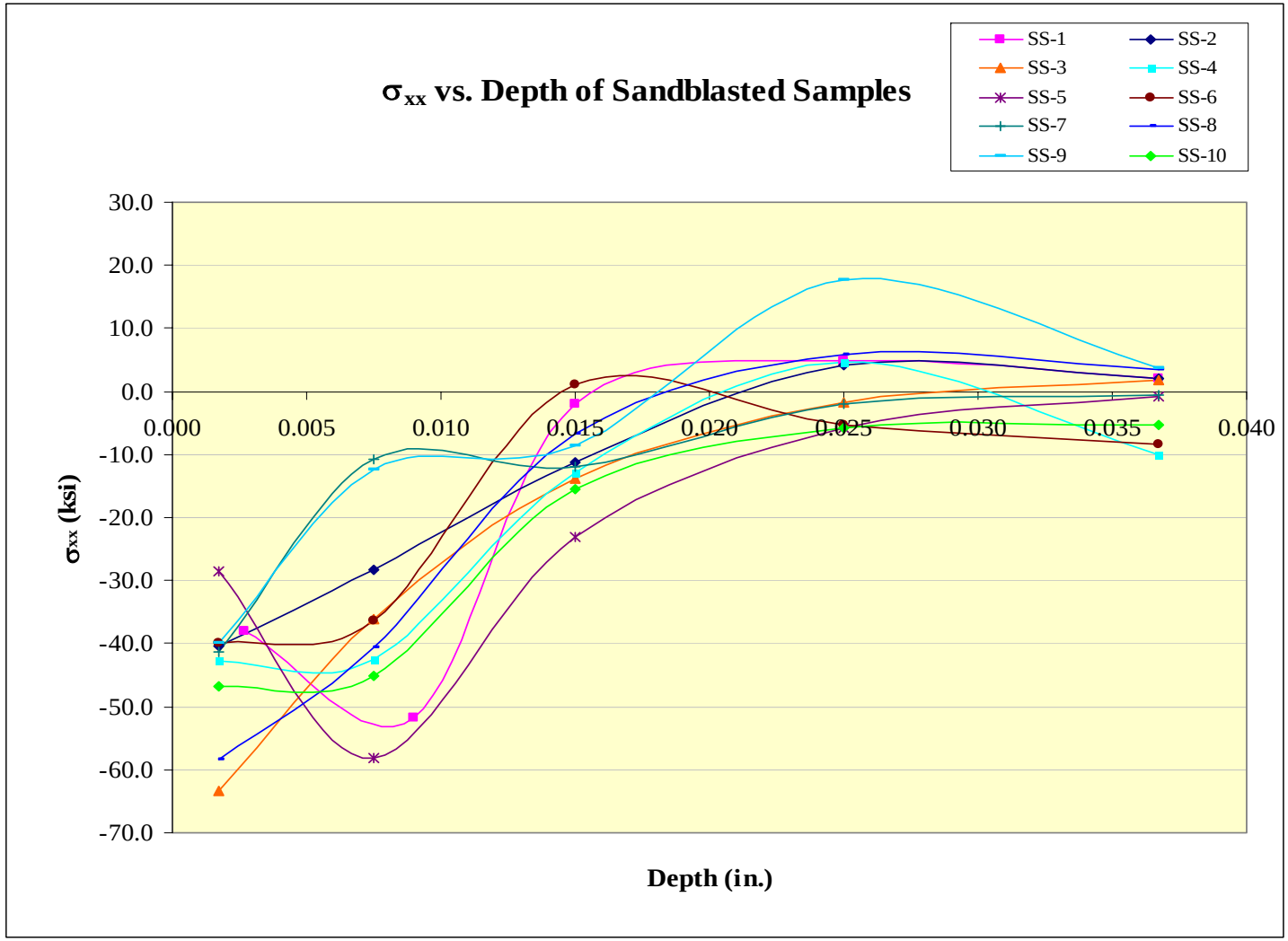

Figure 26: σ_{xx} **versus depth curves of sandblasted samples – SGHD method.**

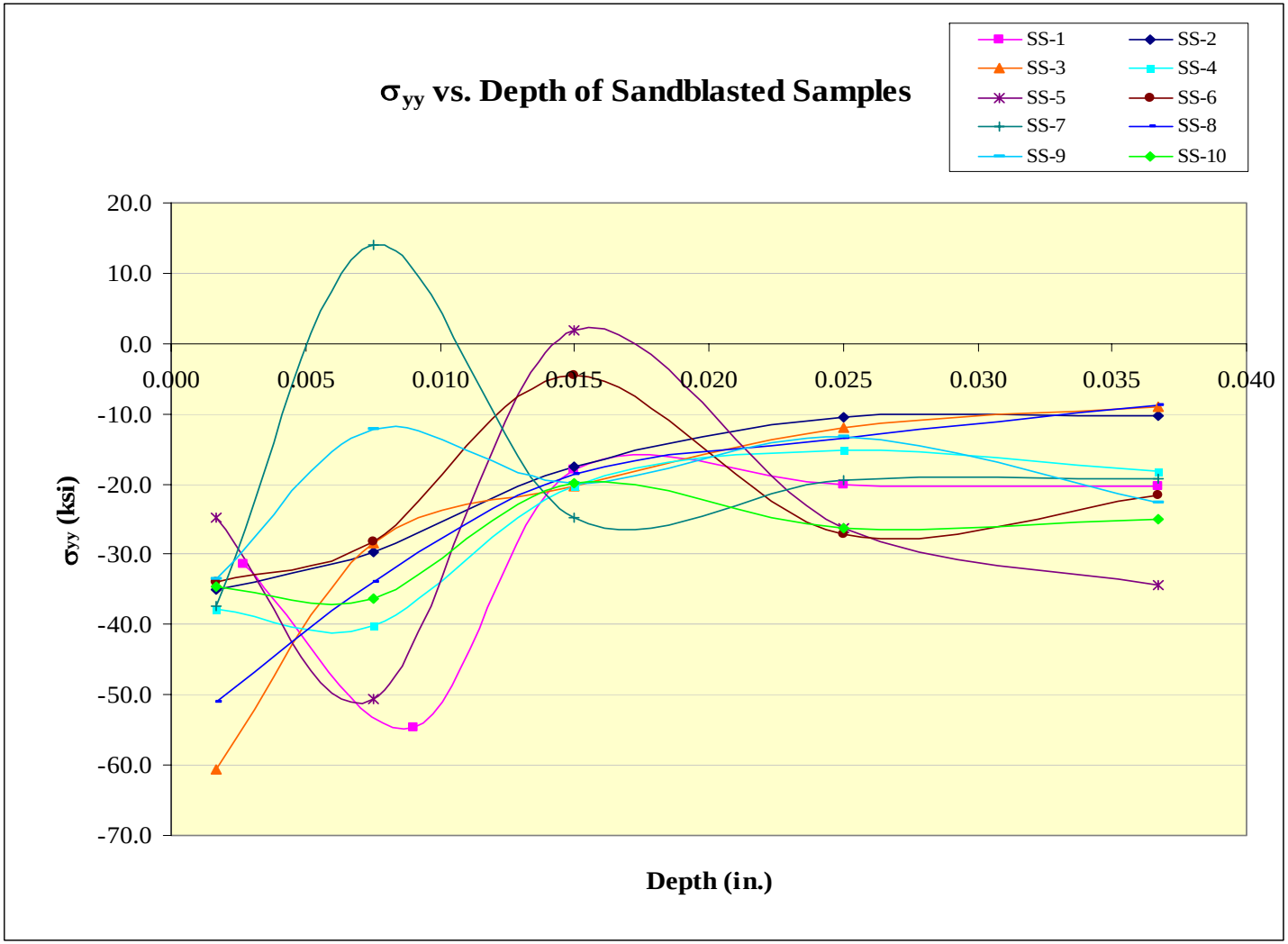

Figure 27: σ_{yy} versus depth curves of sandblasted samples – SGHD method.

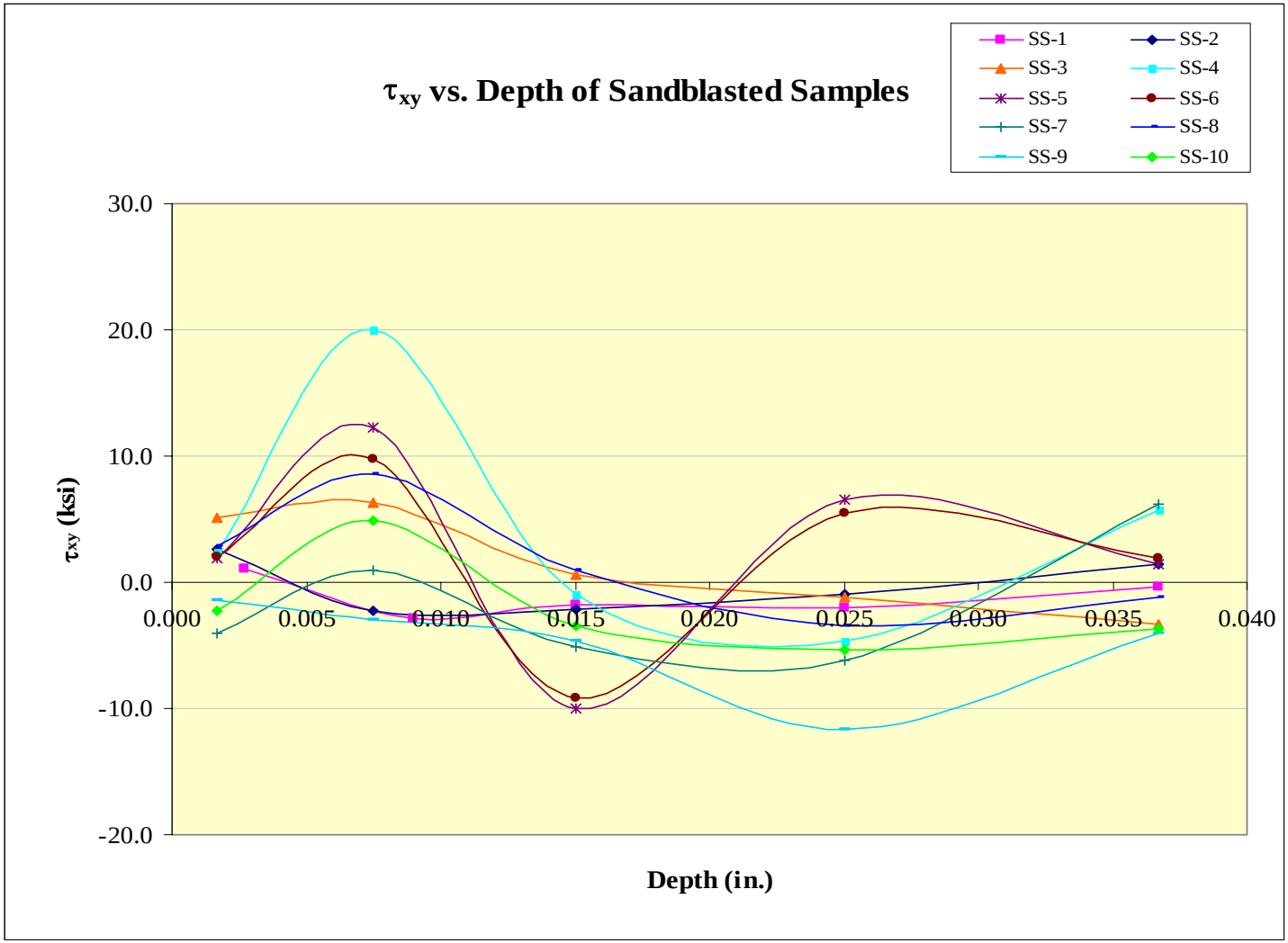

Figure 28: τ_{xy} versus depth curves of sandblasted samples – SGHD method.

Referring to Figure 26, the value of σ_{xx} for all samples started off as compressive. This is expected for sandblasted samples, since sandblasting creates compressive stresses close to the surface. The compressive stresses in eight out of ten samples decreased gradually as depth increased. Some stresses eventually became tensile, while some stayed compressive. The other two samples showed an increase in compressive stress up to depth of 0.0075-0.0085 in. from the surface. Compressive stress then decreased as depth increased. One stress became tensile and the other stayed compressive. Overall, σ_{xx} in all samples eventually became fairly close to zero as depth increased. In general, most of the sandblasted samples had similar σ_{xx} profiles.

Figure 27 demonstrates similar behavior of σ_{yy} in the sandblasted samples to that of σ_{xx}, as described in the previous paragraph. The only exception is that instead of converging to zero, six out of ten σ_{yy} values converged to around -20 ksi and three out of ten converged to -10 ksi as depth increased. Unlike σ_{xx}, σ_{yy} in most samples did not become tensile; they generally stayed compressive.

Figure 28 illustrates that shear stress (τ_{xy}) in the sandblasted samples generally increased up to a depth of 0.0075 in., and then decreased to eventually become fairly close to zero as depth increased.

6.2.3 Discussions

Again, one can observe that the unblasted samples generally have compressive stresses close to the surface. Unlike the sandblasted samples, this behavior was not expected. As stated in Section 6.1.3, one possible reason for this phenomenon is that the plate may have undergone some type of cold leveling to flatten its surface, before it was

cut into smaller pieces. If this is indeed the case, the compressive stresses close to the surface would be expected.

Figures 23 and 26 also demonstrate that close to the surface, the sandblasted samples had higher compressive stresses compared to the unblasted samples. This was expected, and is due on the effect of sandblasting.

Shear stress **(**τ_{xy}**)** magnitudes in the unblasted samples tended to be constant throughout the hole depth, and generally very small. Shear stresses in the sandblasted samples were not constant throughout the hole depth. They generally increased up to a depth of 0.0075 in., and then decreased to eventually become fairly close to zero as depth increased.

6.3 ESPI HOLE DRILLING METHOD

All ESPI hole drilling measurements were taken along the centerline of each sample. One measurement was taken at a distance of 4.125 in. from one end of the sample, which is the same exact location as point B, as described in Section 6.1, and the others were taken at random locations along the centerline of each sample. Since point A (where the strain-gage hole drilling measurements were done) and point B are less than one inch apart from each other, some surface preparations done for the strain-gage hole drilling method have also affected some areas surrounding point B, where the ESPI hole drilling measurements were done (Figure 29). This factor may had an effect on the stress results, since different surface conditions generate different level of reflections. Because of this reason, more than one measurement was done on several samples to check

whether the difference in surface condition around the point of interest greatly affected the stress results.

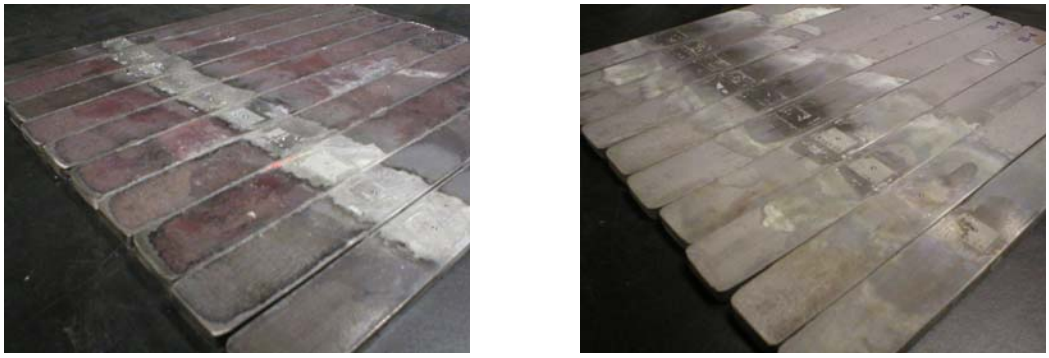

Figure 29a, b: Difference in surface conditions on unblasted & sandblasted samples.

Identical to the X-ray diffraction and the strain-gage hole drilling methods, all unblasted samples start with the prefix ‘US’, and all sandblasted samples start with the prefix ‘SS’.

Stresses were calculated from the deformation data, also known as the interferograms, using a beta version of the PRISM-RS software, which was developed by Hytec, Incorporated, in Los Alamos, New Mexico, based on the analysis method developed by Nelson, et al. [28], and later adapted by Steinzig, et al. [29], as described in Section 4.2. This is a similar analysis method to the integral method, which was used to analyze the data obtained from the strain-gage hole drilling technique. Once the state of stress was calculated for each measurement, graphs of σ_{xx}, σ_{yy}, and τ_{xy}, versus depth were then plotted for each type of samples.

6.3.1 Unblasted Samples

Fringe patterns acquired at each hole depth increment for one of the ESPI hole drilling measurements on the unblasted samples are shown on Figure 30.

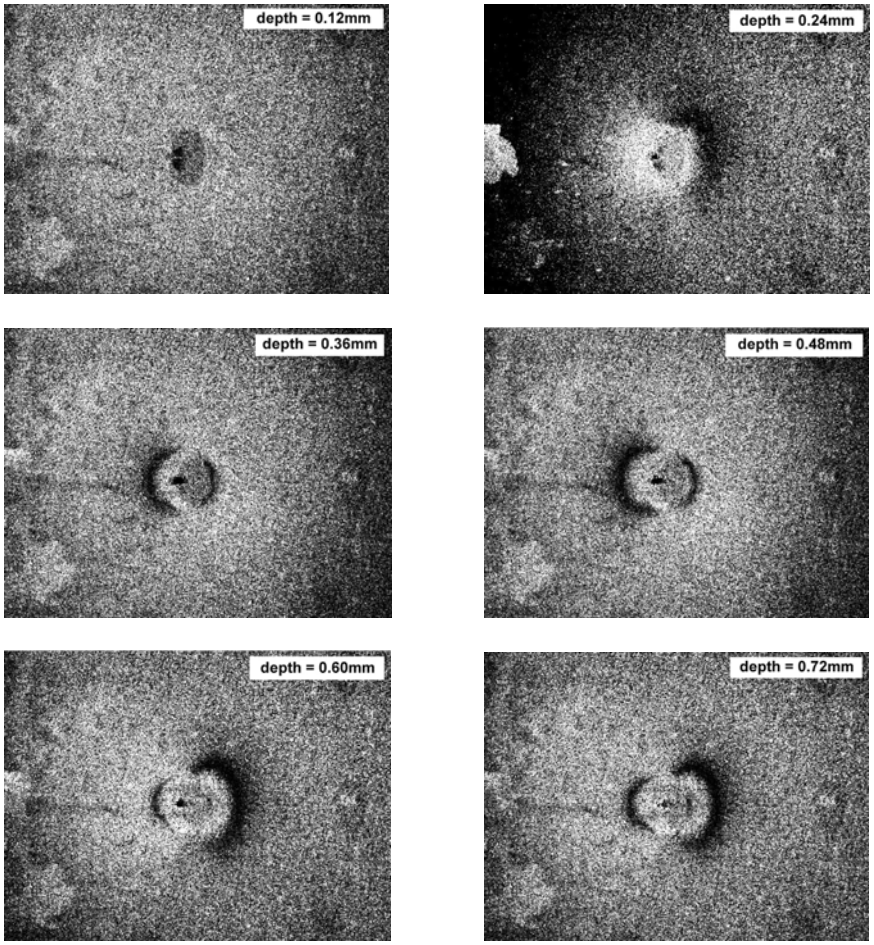

Figure 30: Fringe patterns acquired from a measurement on unblasted sample.

Figure 30 demonstrates that as depth increases, more fringes are observed.

Plots of σ_{xx}, σ_{yy}, and τ_{xy}, versus depth for ESPI hole drilling measurements of the unblasted samples are shown by Figures 31-39 below.

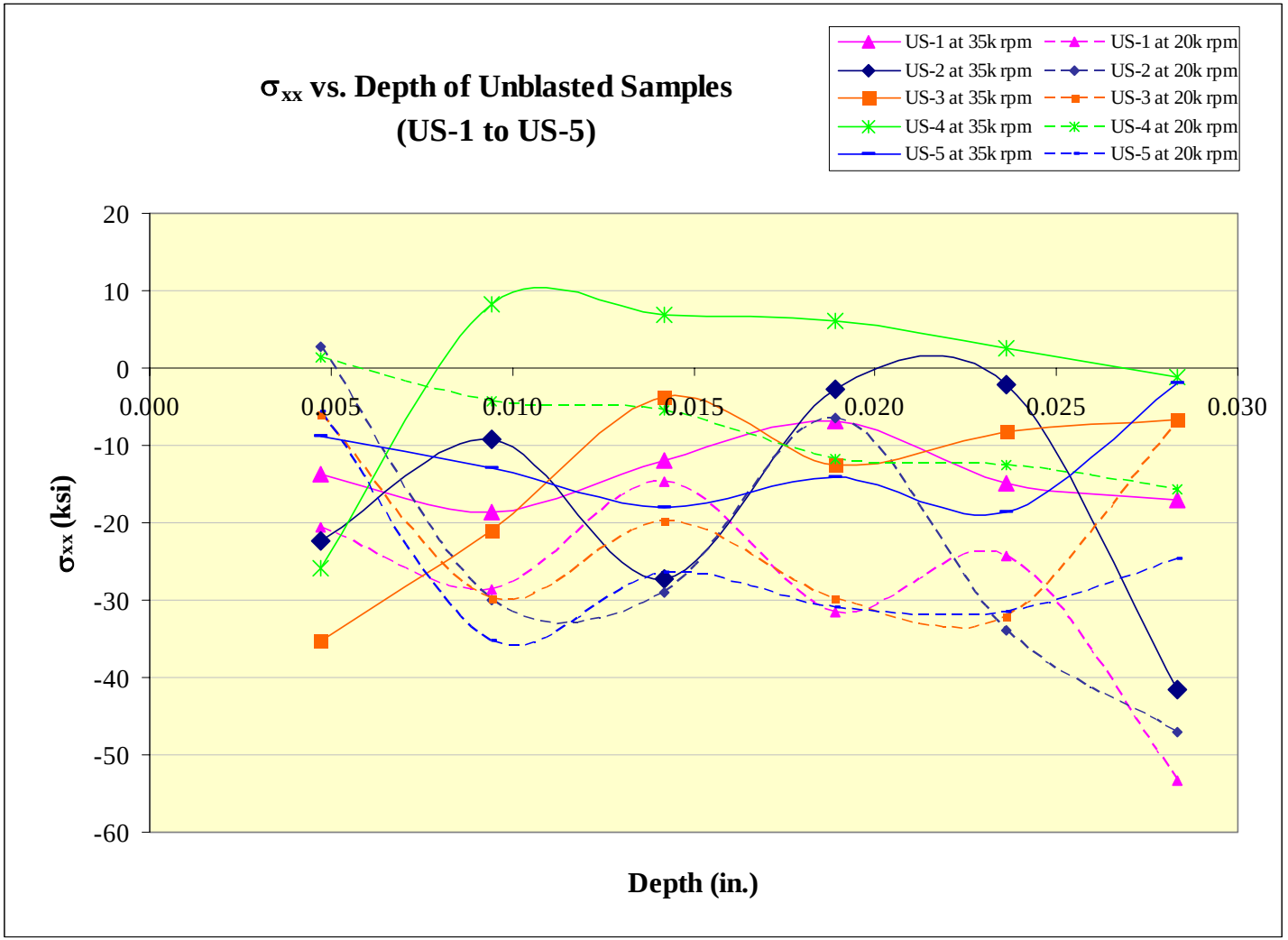

Figure 31: σ_{xx} versus depth curves of US-1 to US-5 – ESPI hole drilling method.

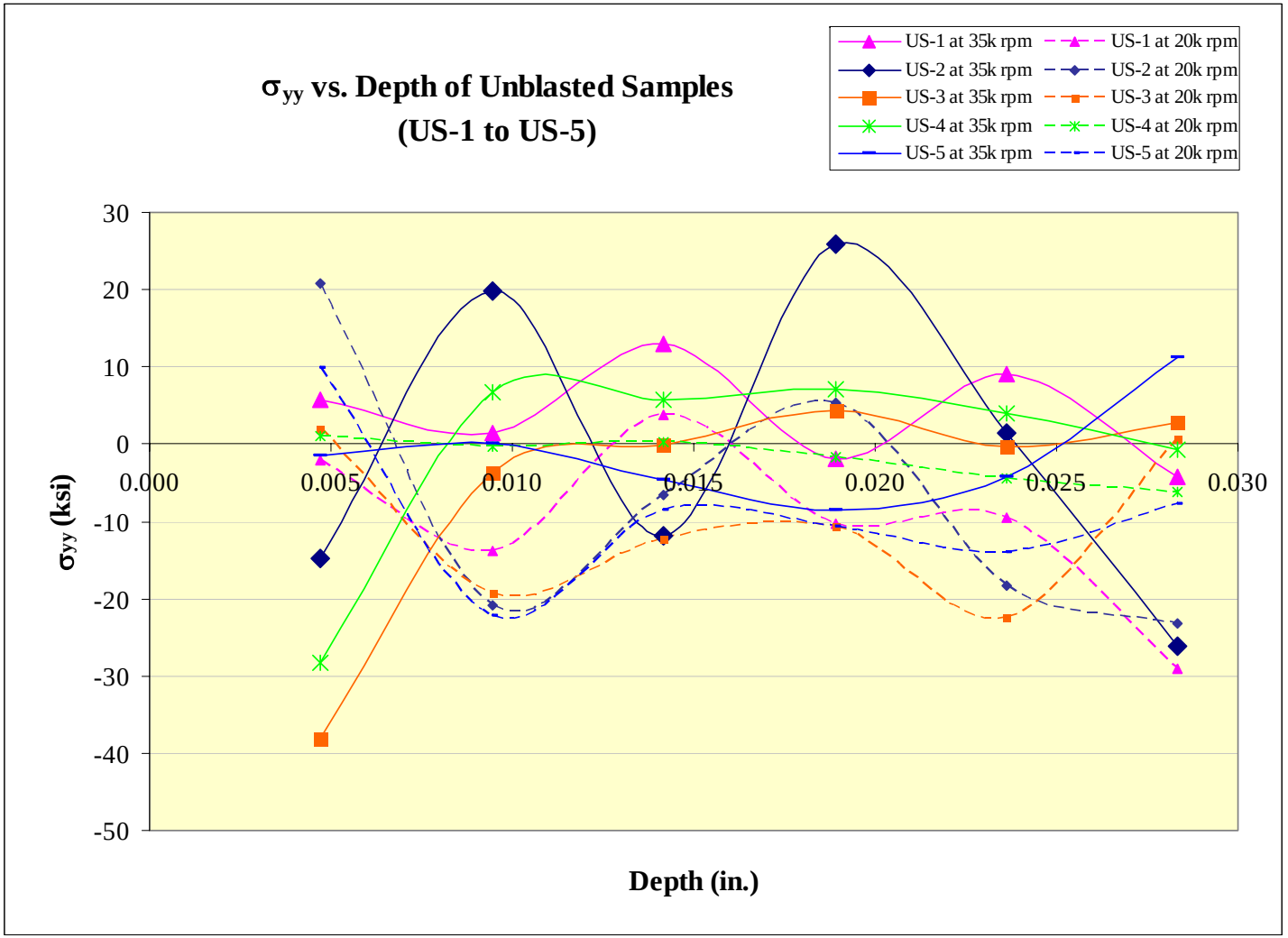

Figure 32: σ_{yy} versus depth curves of US-1 to US-5 – ESPI hole drilling method.

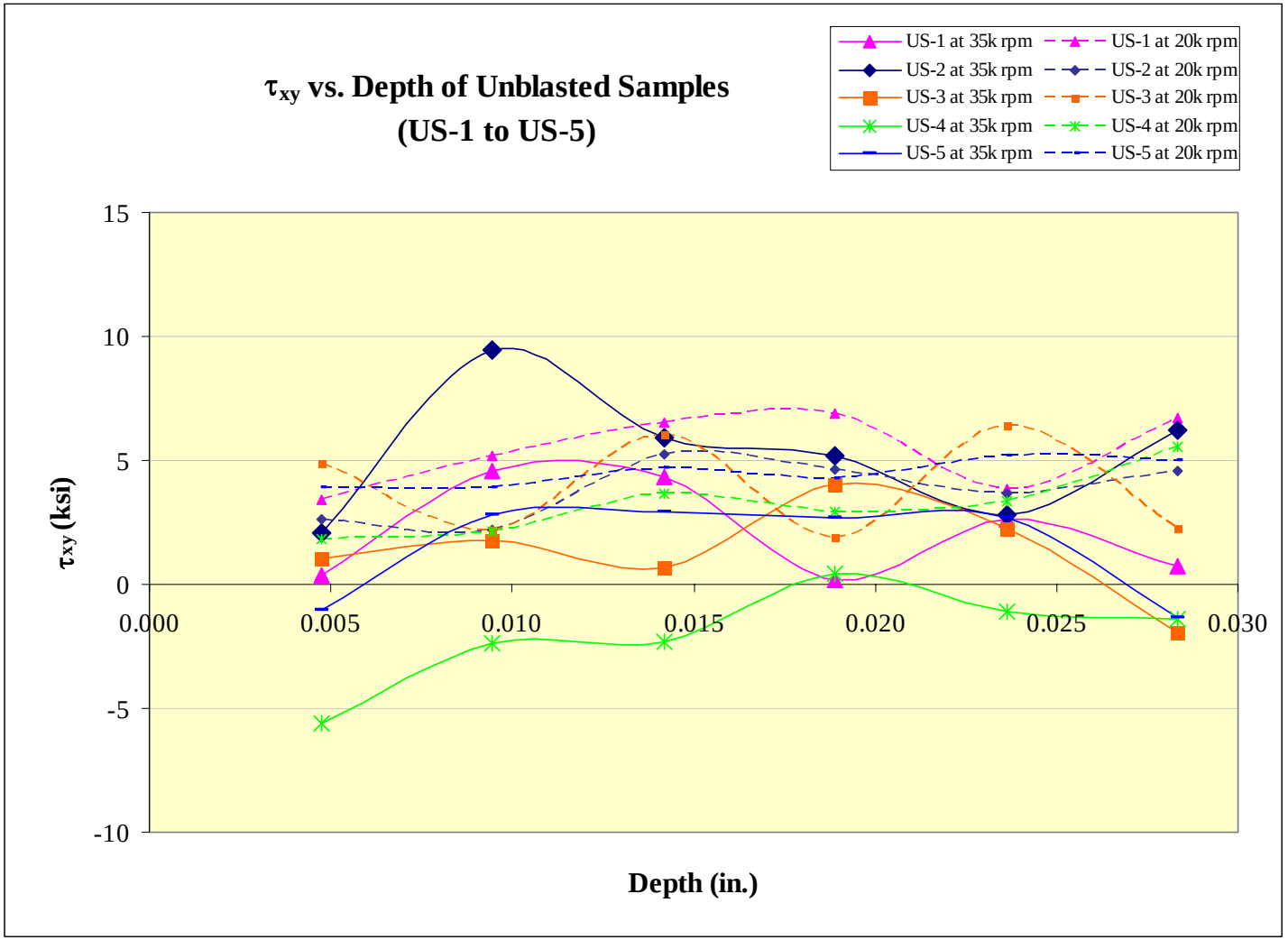

Figure 33: τ_{xy} versus depth curves of US-1 to US-5 – ESPI hole drilling method.

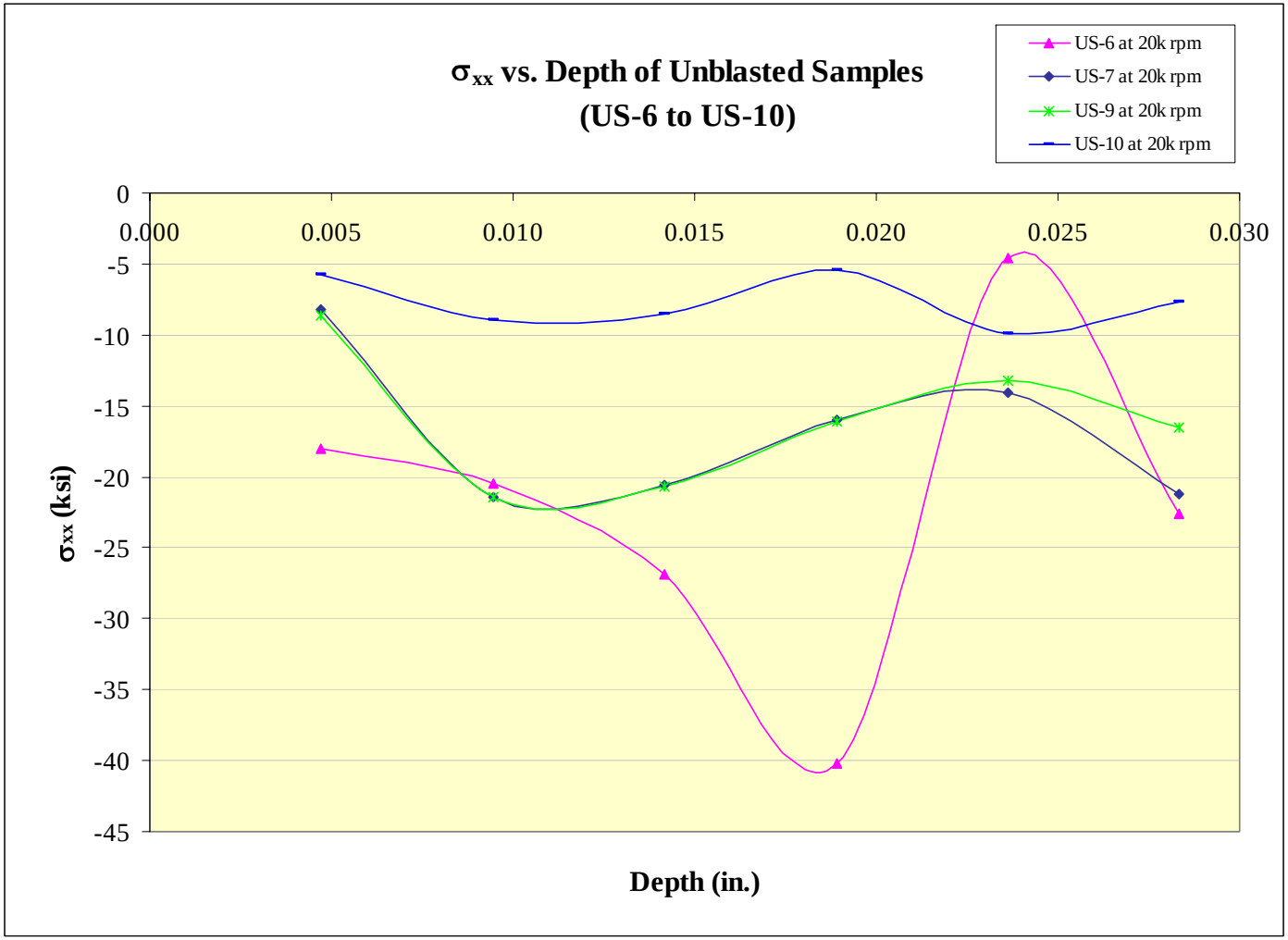

Figure 34: σ_{xx} versus depth curves of US-6 to US-10 – ESPI hole drilling method.

***NOTE**: *US-8 is excluded because of unreliable results (some excess glue is present from strain-gage hole drilling surface preparation on location surface)*

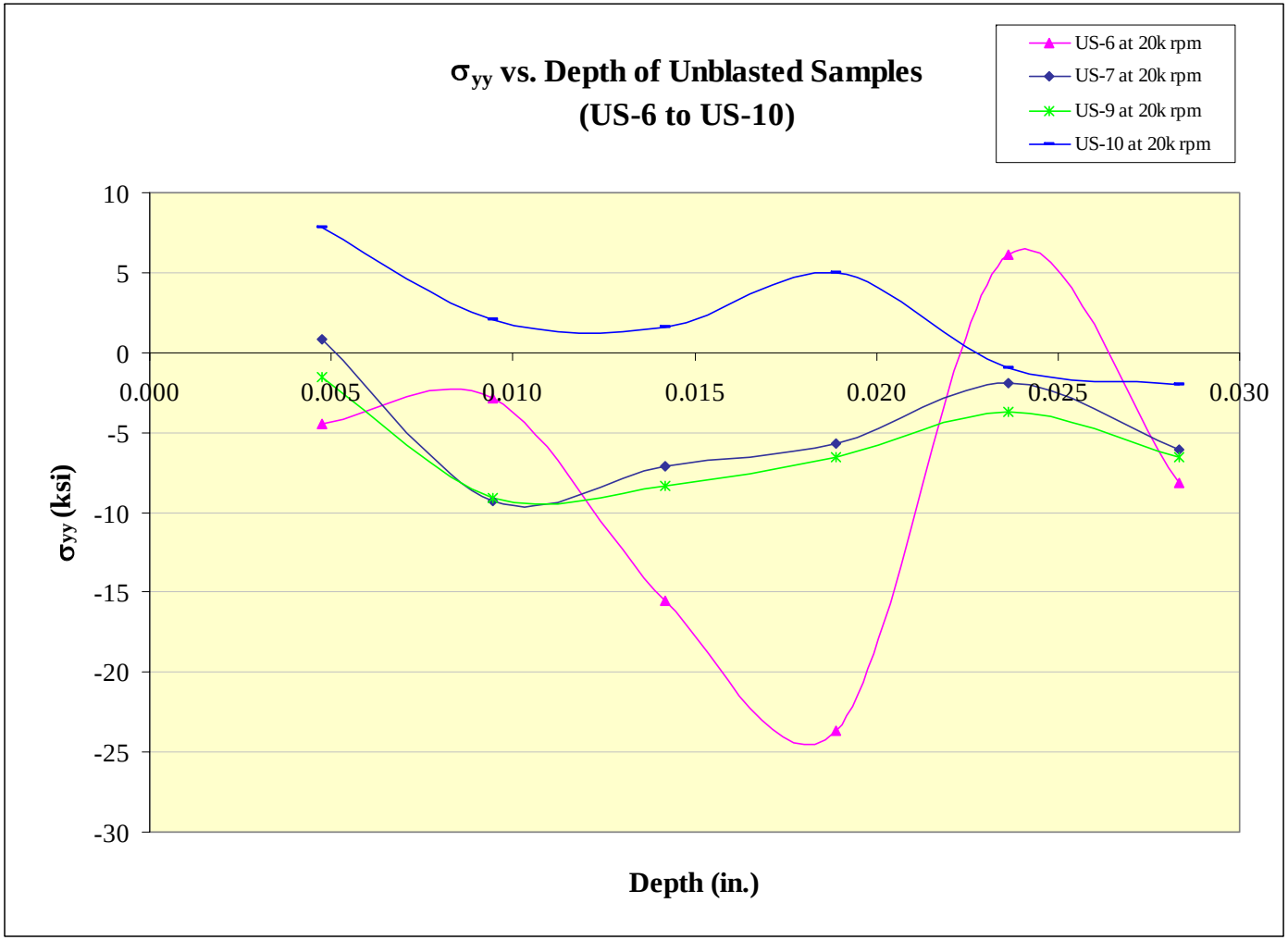

Figure 35: σ_{yy} versus depth curves of US-6 to US-10 – ESPI hole drilling method.

***NOTE**: *US-8 is excluded because of unreliable results (some excess glue is present from strain-gage hole drilling surface preparation on location surface)*

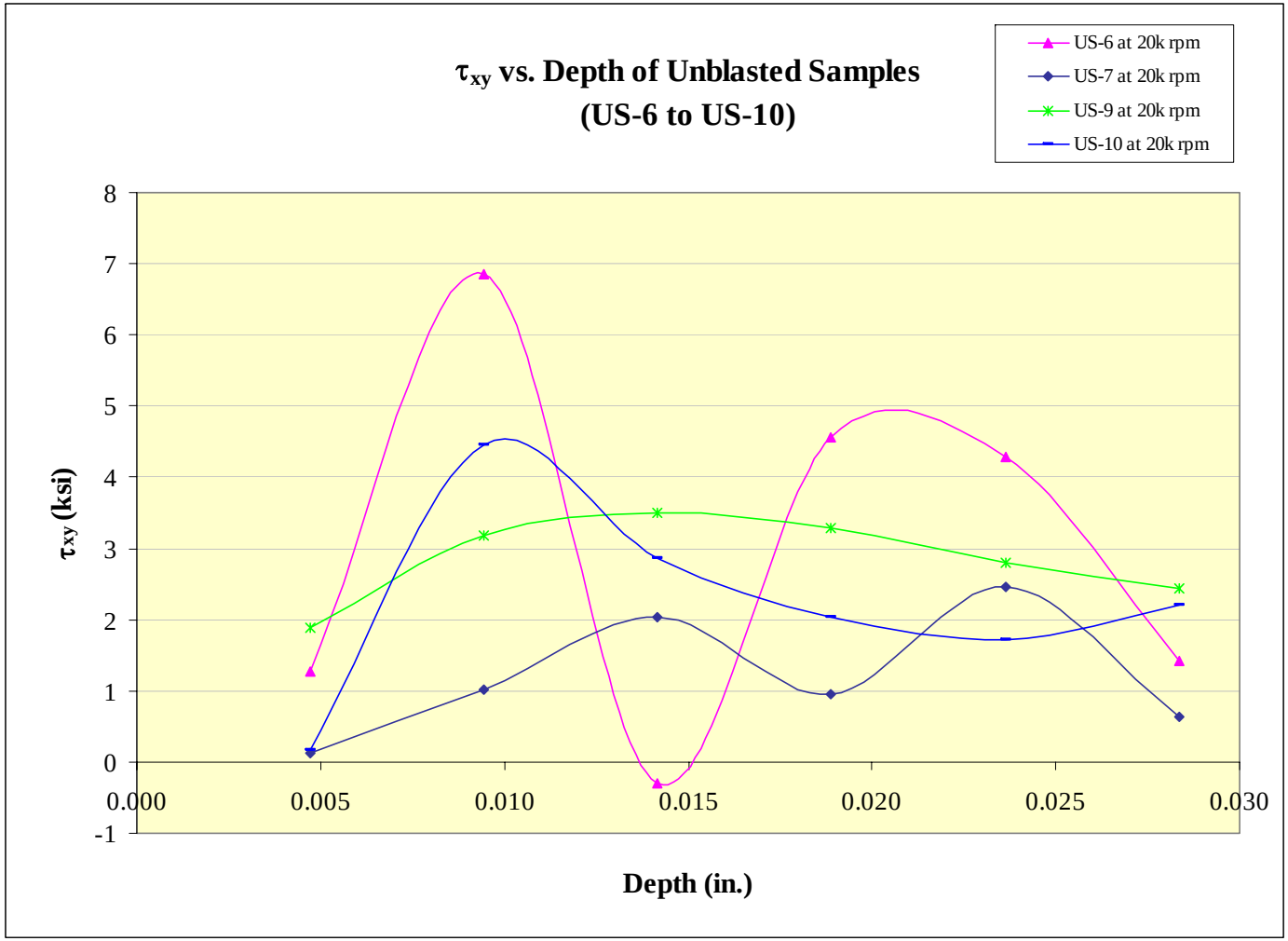

Figure 36: τ_{xy} versus depth curves of US-6 to US-10 – ESPI hole drilling method.

***NOTE**: *US-8 is excluded because of unreliable results (some excess glue is present from strain-gage hole drilling surface preparation on location surface)*

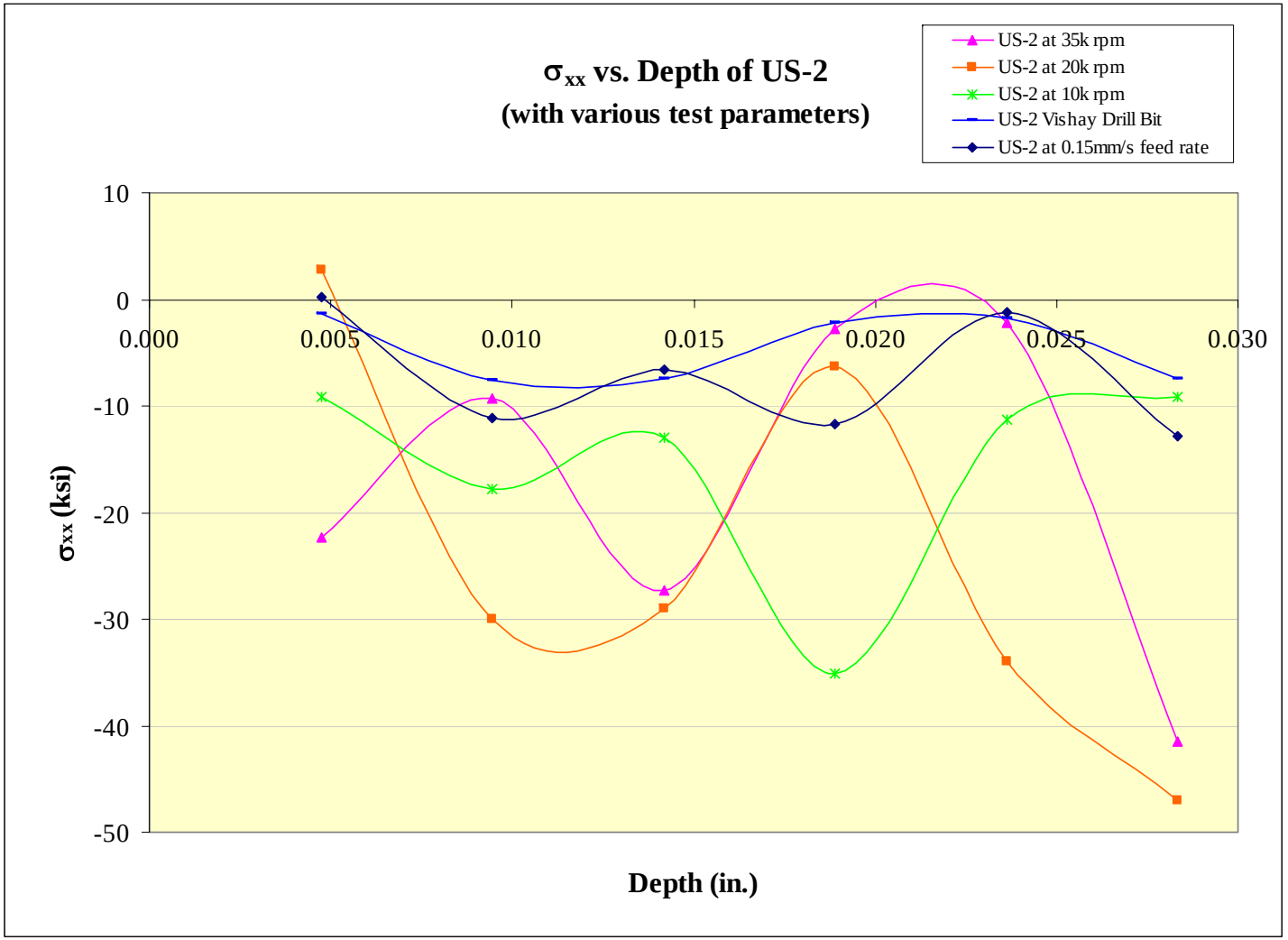

Figure 37: σ_{xx} versus depth curves of US-2 – ESPI hole drilling method.

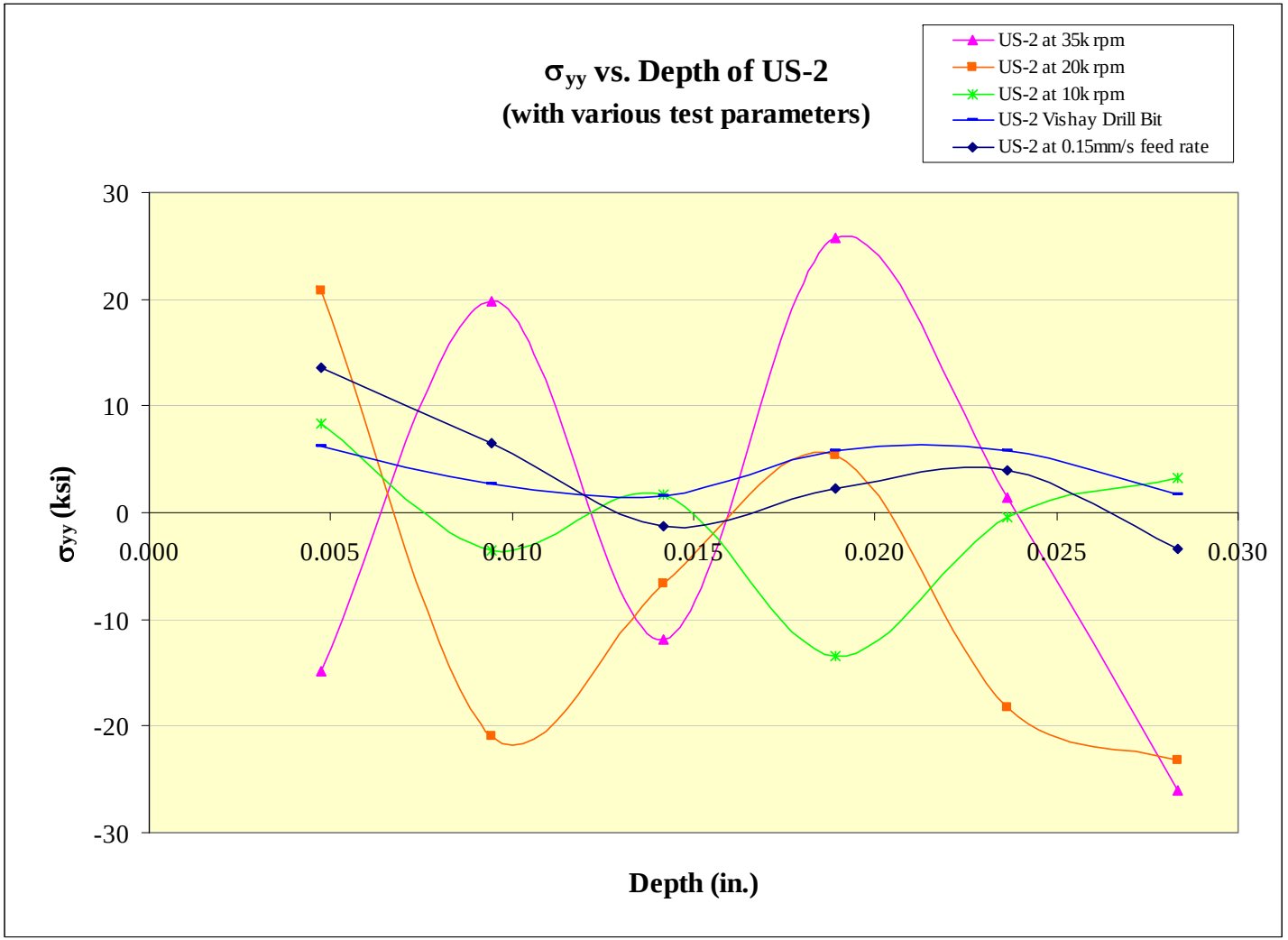

Figure 38: σ_{yy} versus depth curves of US-2 – ESPI hole drilling method.

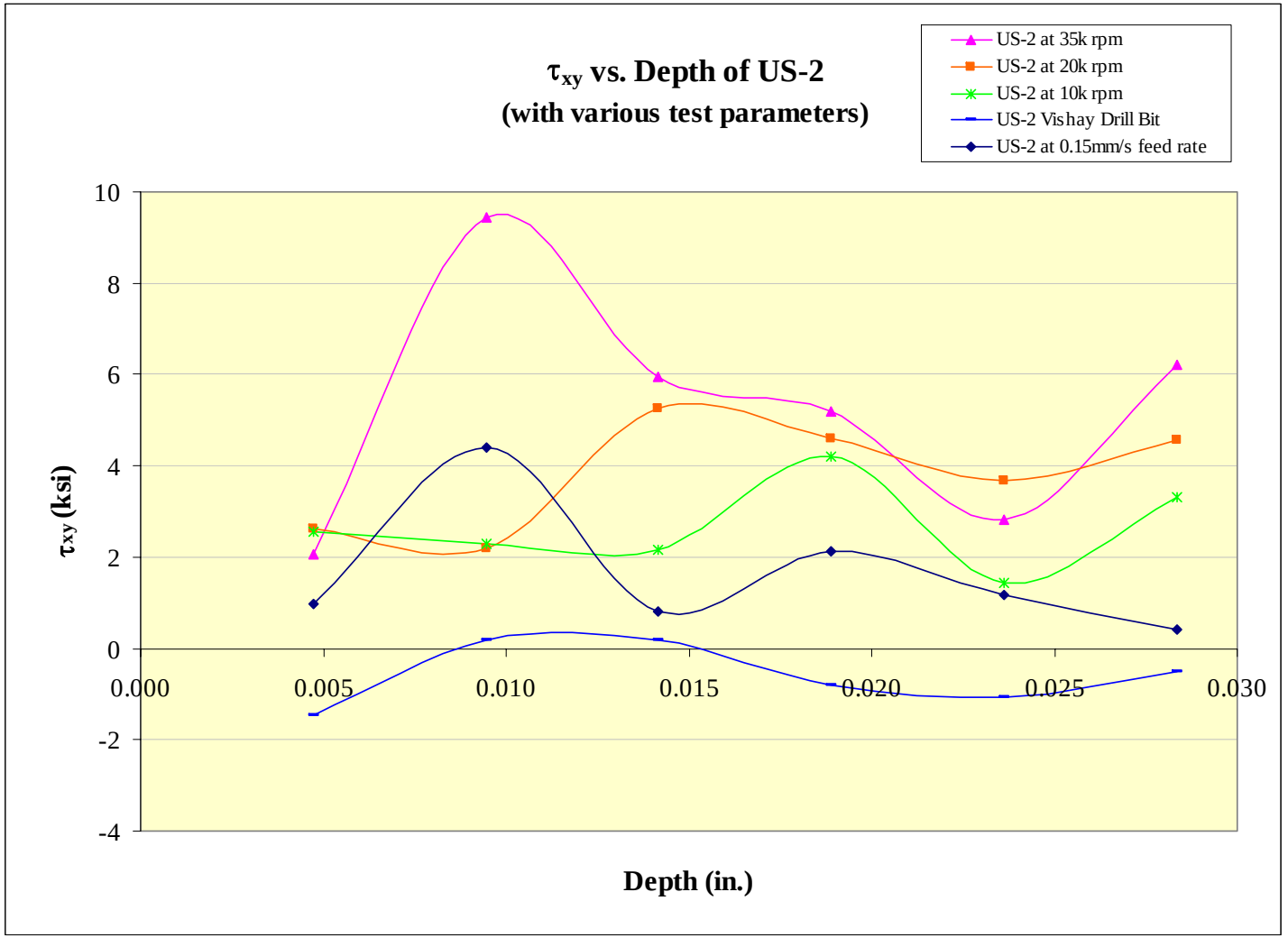

Figure 39: τ_{xy} versus depth curves of US-2 – ESPI hole drilling method.

Figures 31-33 show results of the tests performed at drill speed of 20k rpm at locations where no SGHD surface preparation had been completed. The tests performed at 35k rpm were done at point B (as described in Section 6.1), where some SGHD surface preparations had been completed on the surrounding area. The results demonstrate that at 35k rpm, the samples do not share similar σ_{xx}, σ_{yy}, and τ_{xy} profiles. The drill speed of 20k rpm yielded better results; most samples showed similar σ_{xx}, σ_{yy}, and τ_{xy} profiles.

Figures 31-33 also indicate that different surface conditions yield different results on an ESPI system. With the exception of US-1, it is apparent that measurements at point B on each sample yielded higher compressive stress close to the surface compared to the ones taken at random locations where no surface preparation had been done on their surroundings. Sample US-1 had the smallest prepared surface area compared to the other samples, and therefore the surface of point B and its surrounding area was not affected by any of the SGHD surface preparation process that may affect the state of stress close to the surface.

Since the results of US-1 to US-5 indicated that a drill speed of 20k rpm worked better than 35k rpm, all measurements on US-6 to US-10 were done using a drill speed of 20k rpm. Figures 34 and 35 show that the σ_{xx} and σ_{yy} profiles of US-7 and US-9 were almost identical to each other.

Finally, in an effort to find the appropriate drill speed, drill feed rate, and drill bit type, several measurements were completed on US-2 with various test parameters. Figures 37-39 show that the profiles vary for each setting. At this point, the appropriate test parameters for this particular material remain unknown. Further work in this area

was beyond the scope of this research. Note that the PRISM-RS beta version software was used to analyze these results.

6.3.2 Sandblasted Samples

Fringe patterns acquired at each hole depth increment for one of the ESPI hole drilling measurements on the sandblasted samples are shown on Figure 40.

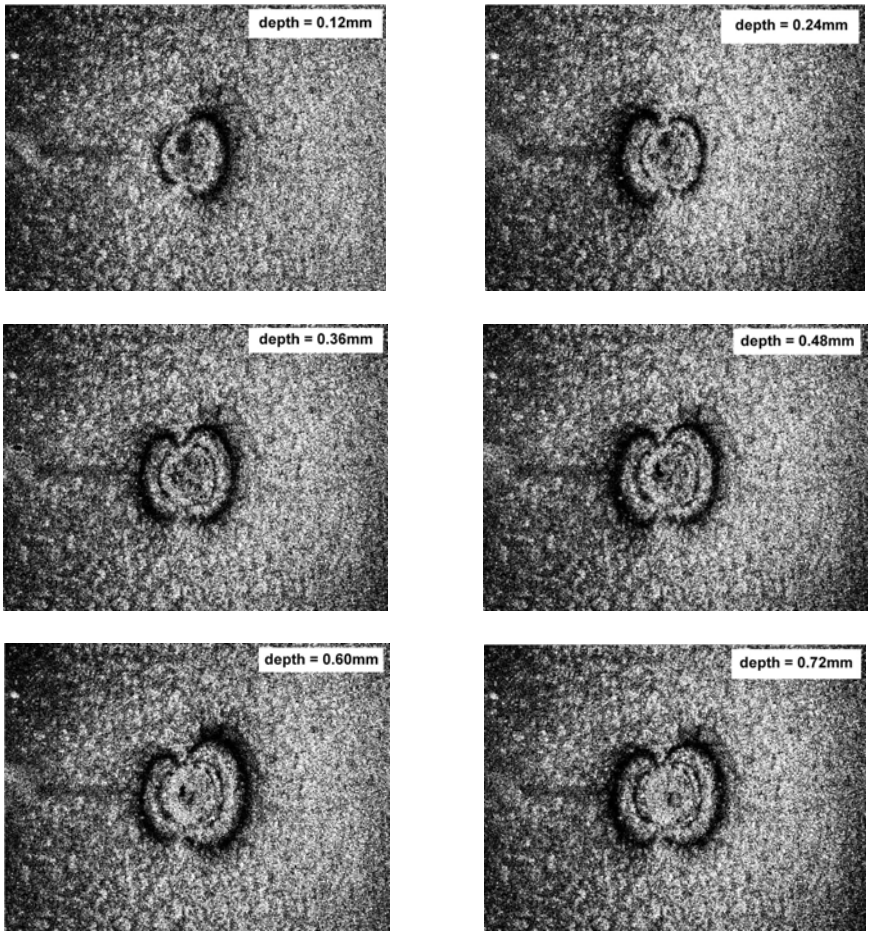

Figure 40: Fringe patterns acquired from a measurement on sandblasted sample.

Similar to Figure 30 for unblasted samples, Figure 40 demonstrates that as depth increased, more fringes were observed.

Plots of σ_{xx}, σ_{yy}, and τ_{xy}, versus depth for ESPI hole drilling measurements of the unblasted samples are shown by Figures 41-49 below.

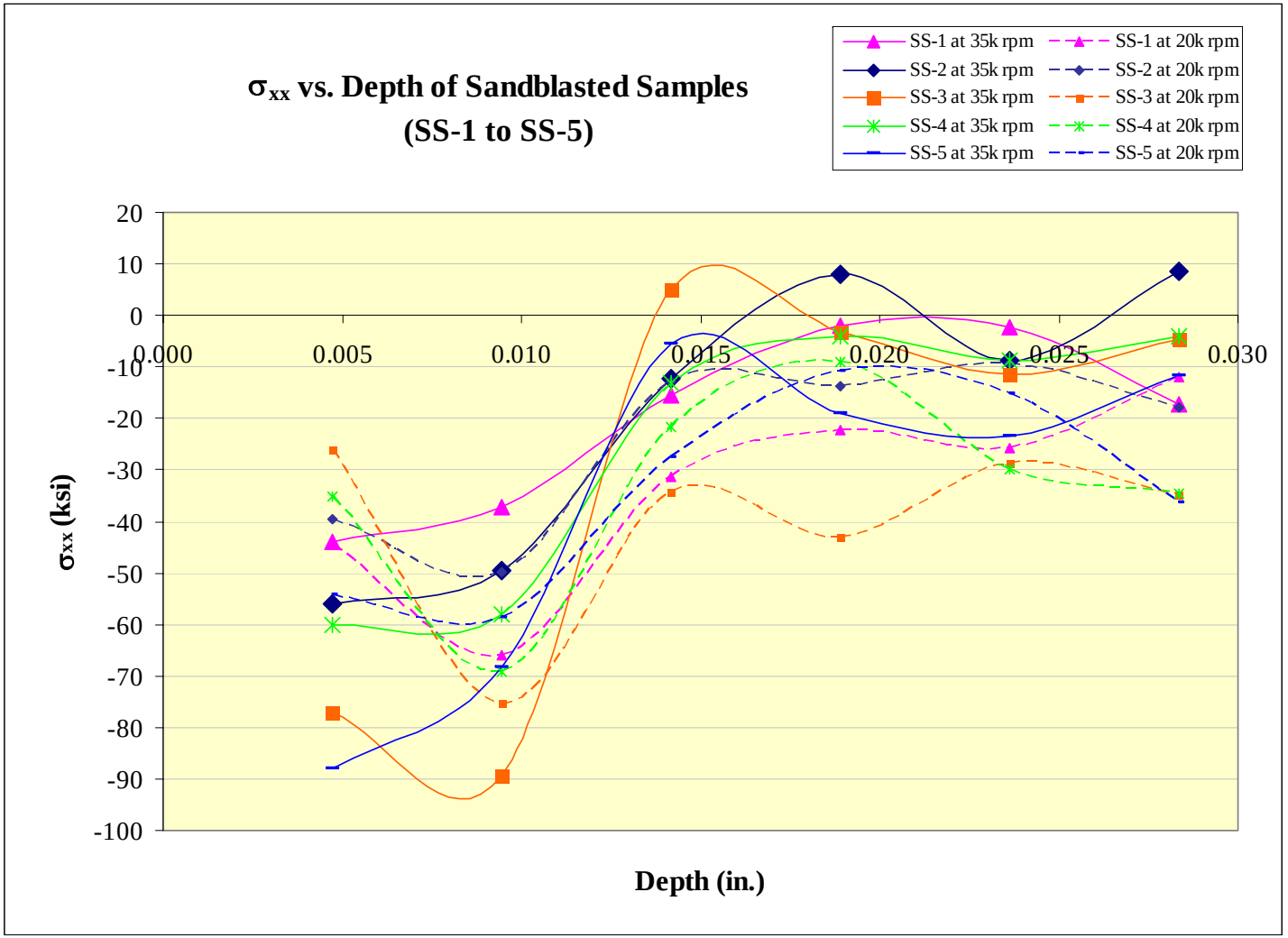

Figure 41: σ_{xx} versus depth curves of SS-1 to SS-5 – ESPI hole drilling method.

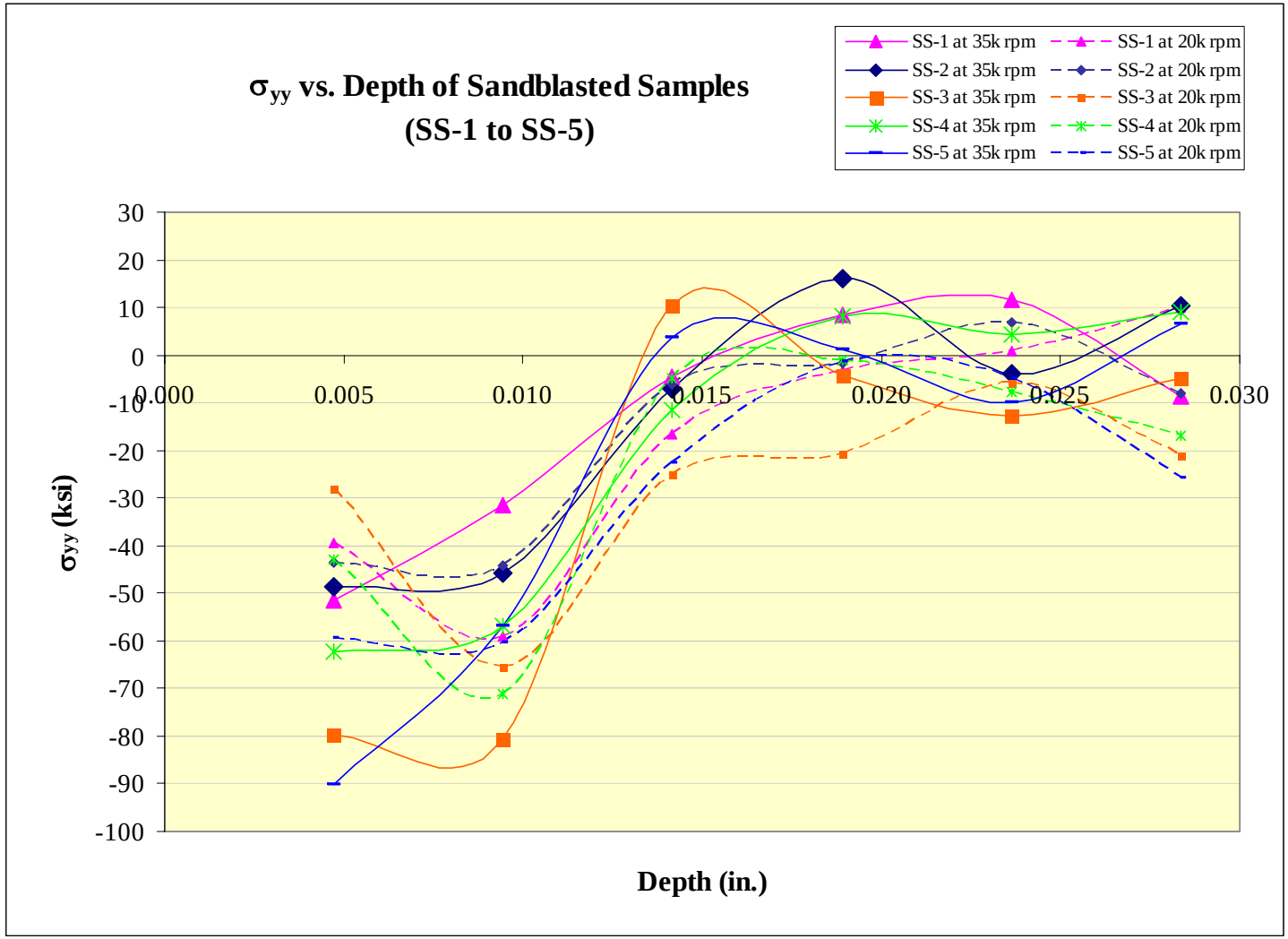

Figure 42: σ_{yy} versus depth curves of SS-1 to SS-5 – ESPI hole drilling method.

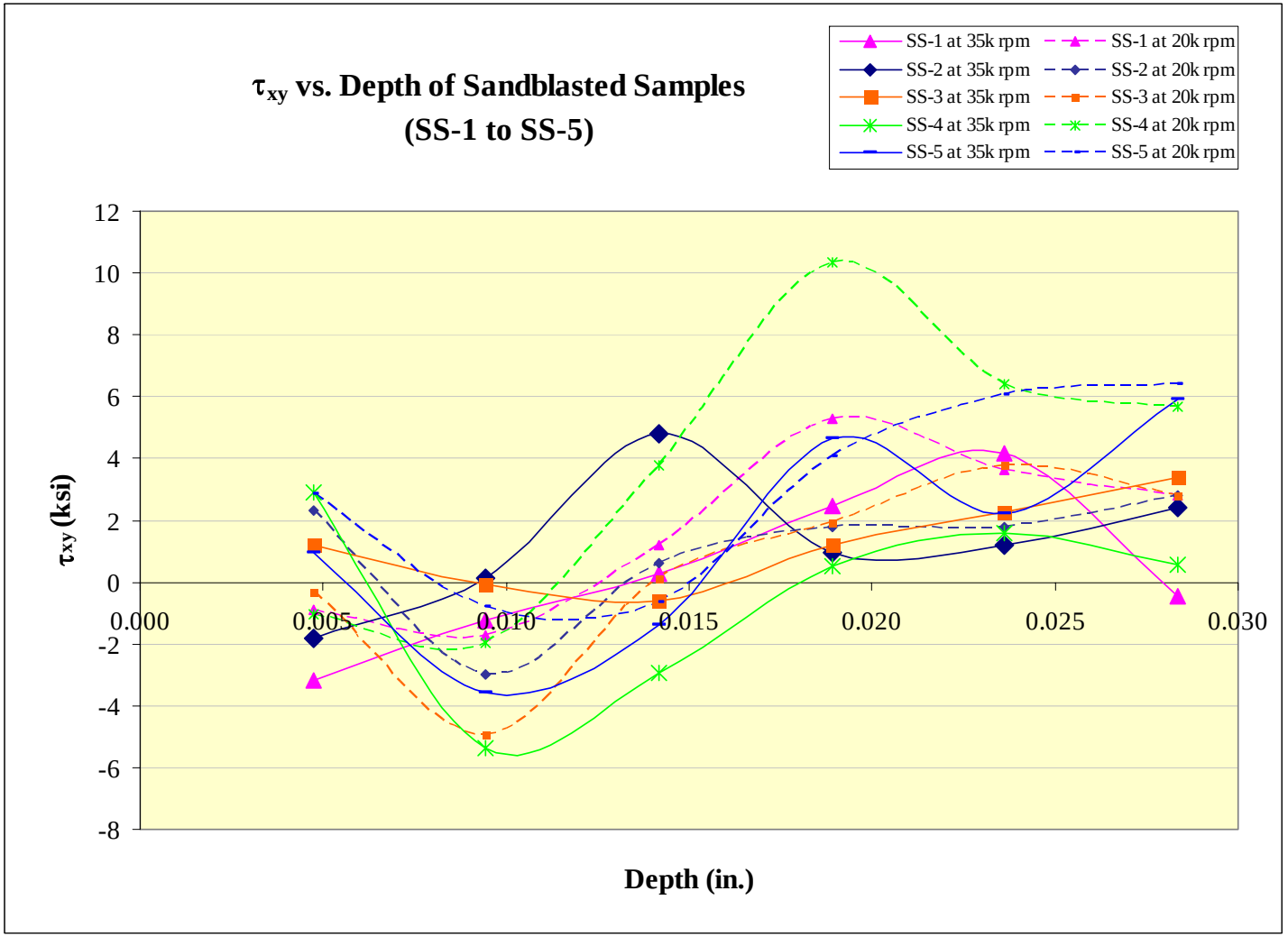

Figure 43: τ_{xy} versus depth curves of SS-1 to SS-5 – ESPI hole drilling method.

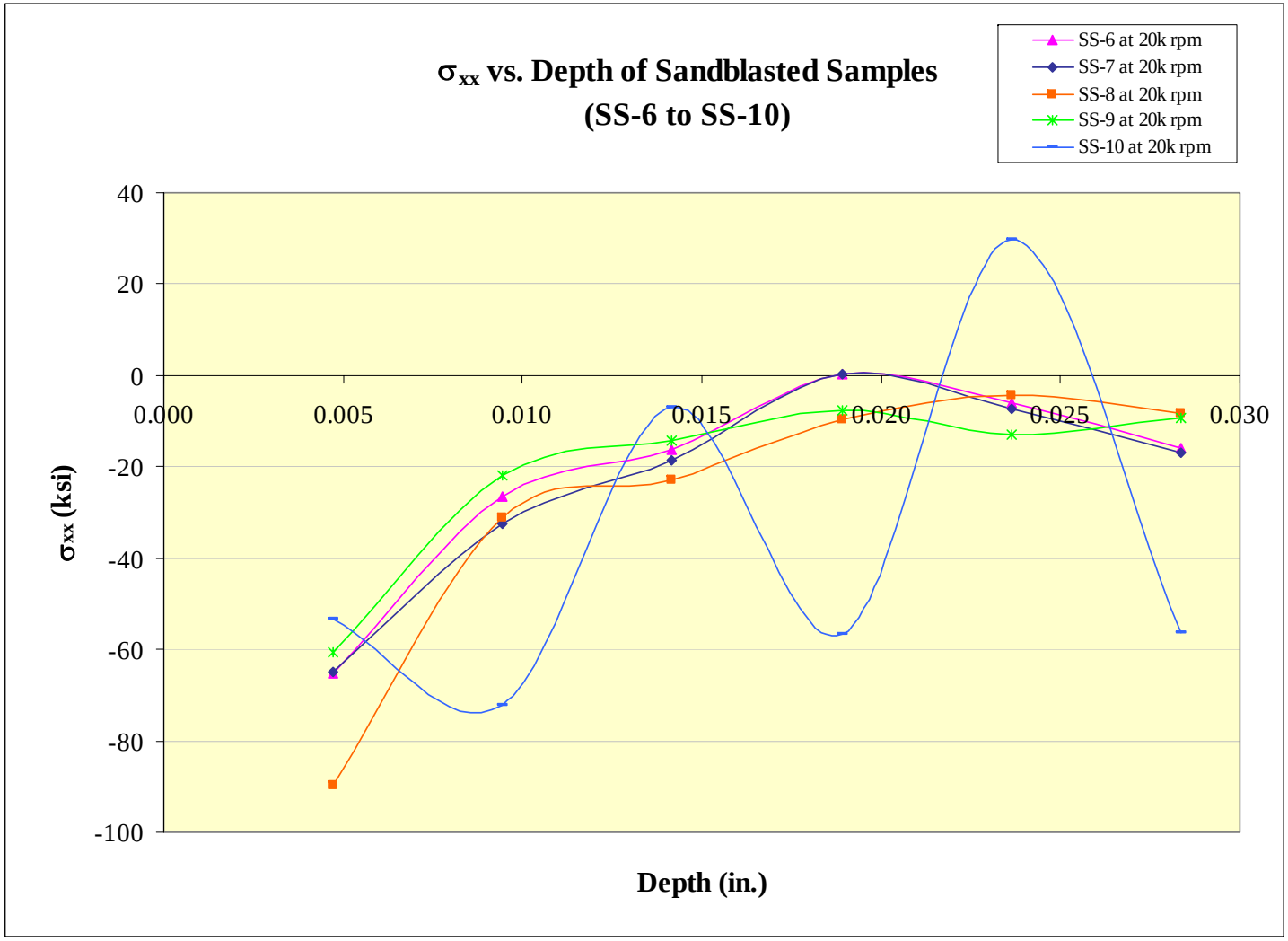

Figure 44: σ_{xx} versus depth curves of SS-6 to SS-10 – ESPI hole drilling method.

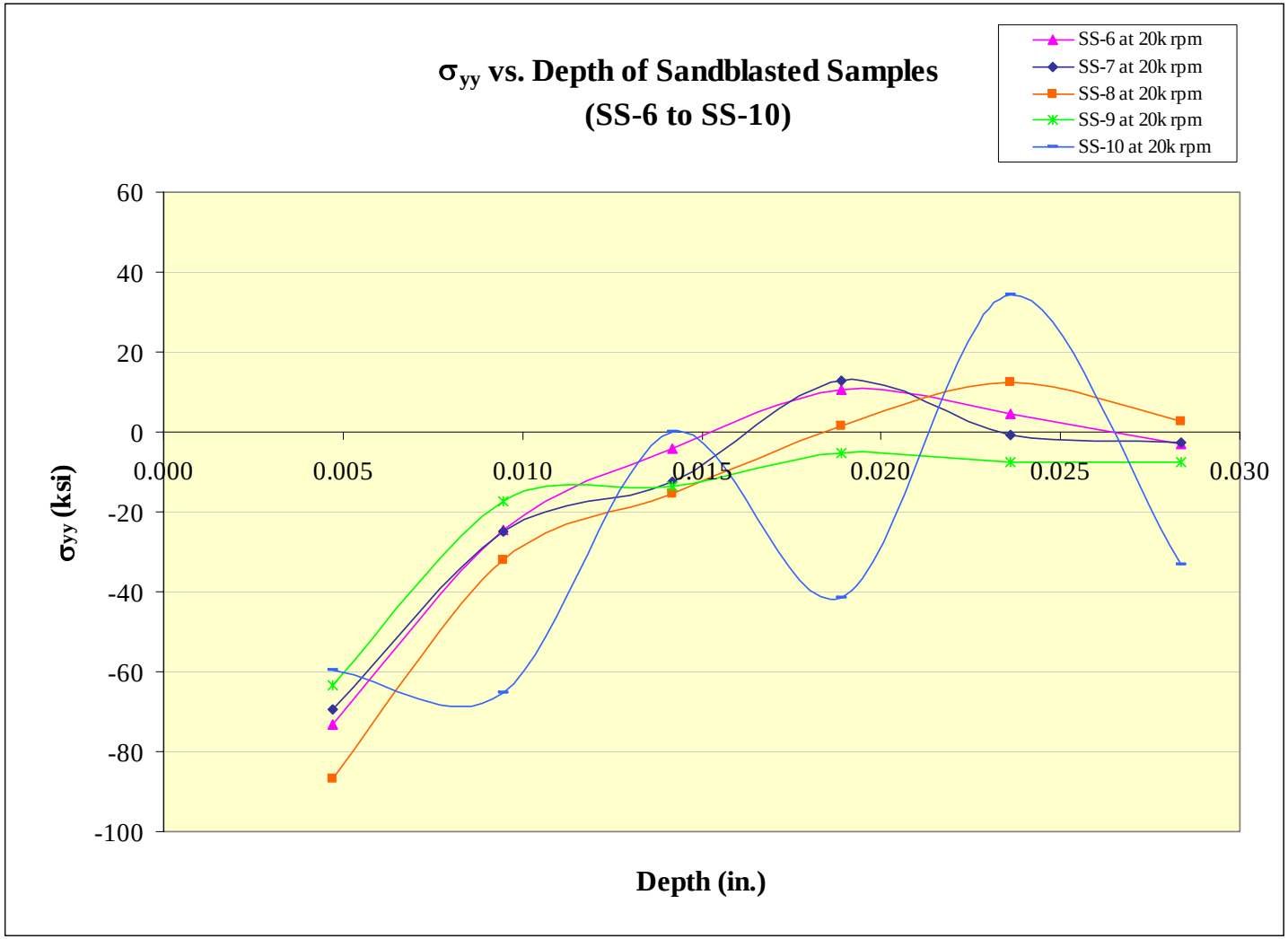

Figure 45: σ_{yy} versus depth curves of SS-6 to SS-10 – ESPI hole drilling method.

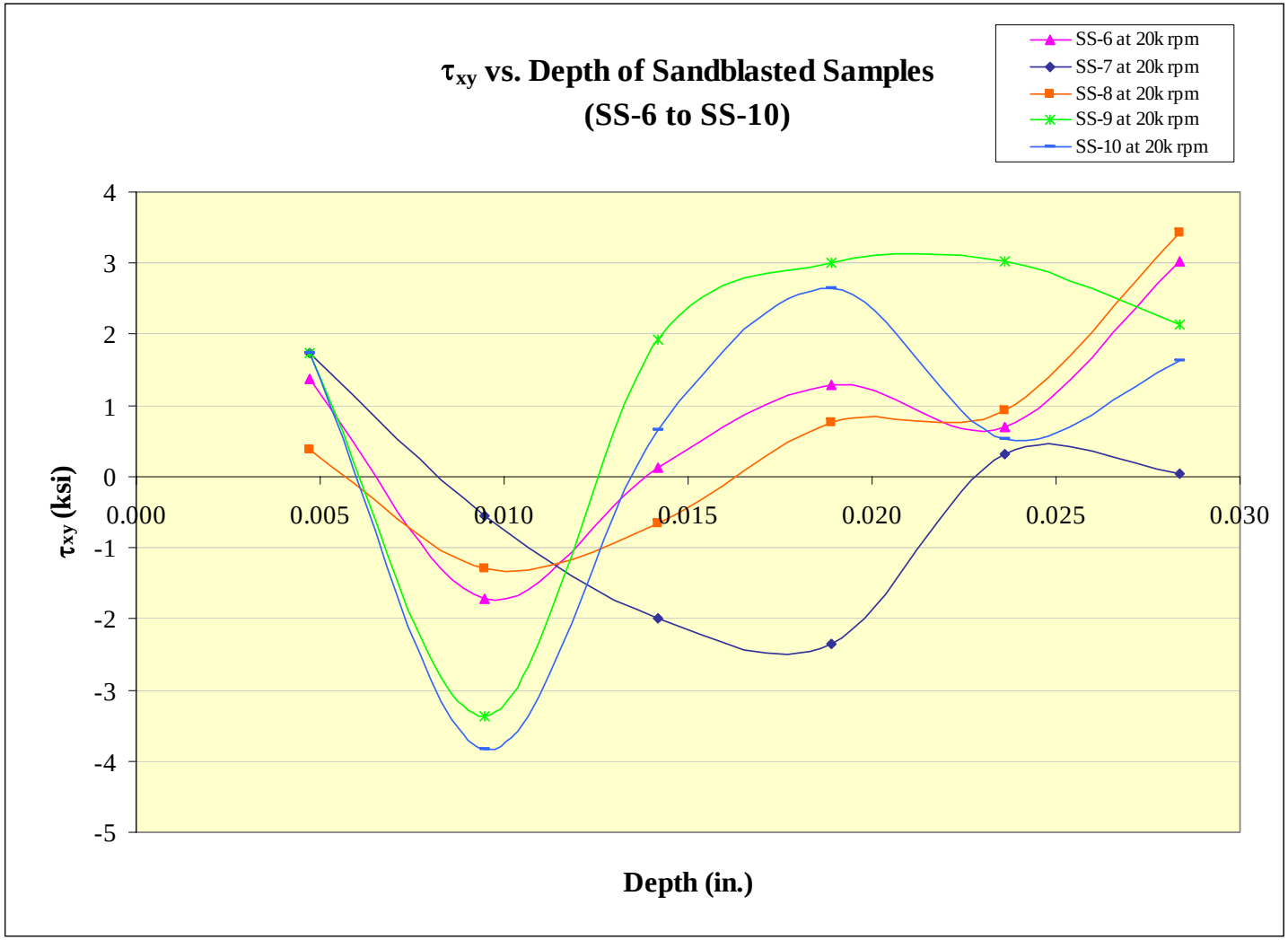

Figure 46: τ_{xy} versus depth curves of SS-6 to SS-10 – ESPI hole drilling method.

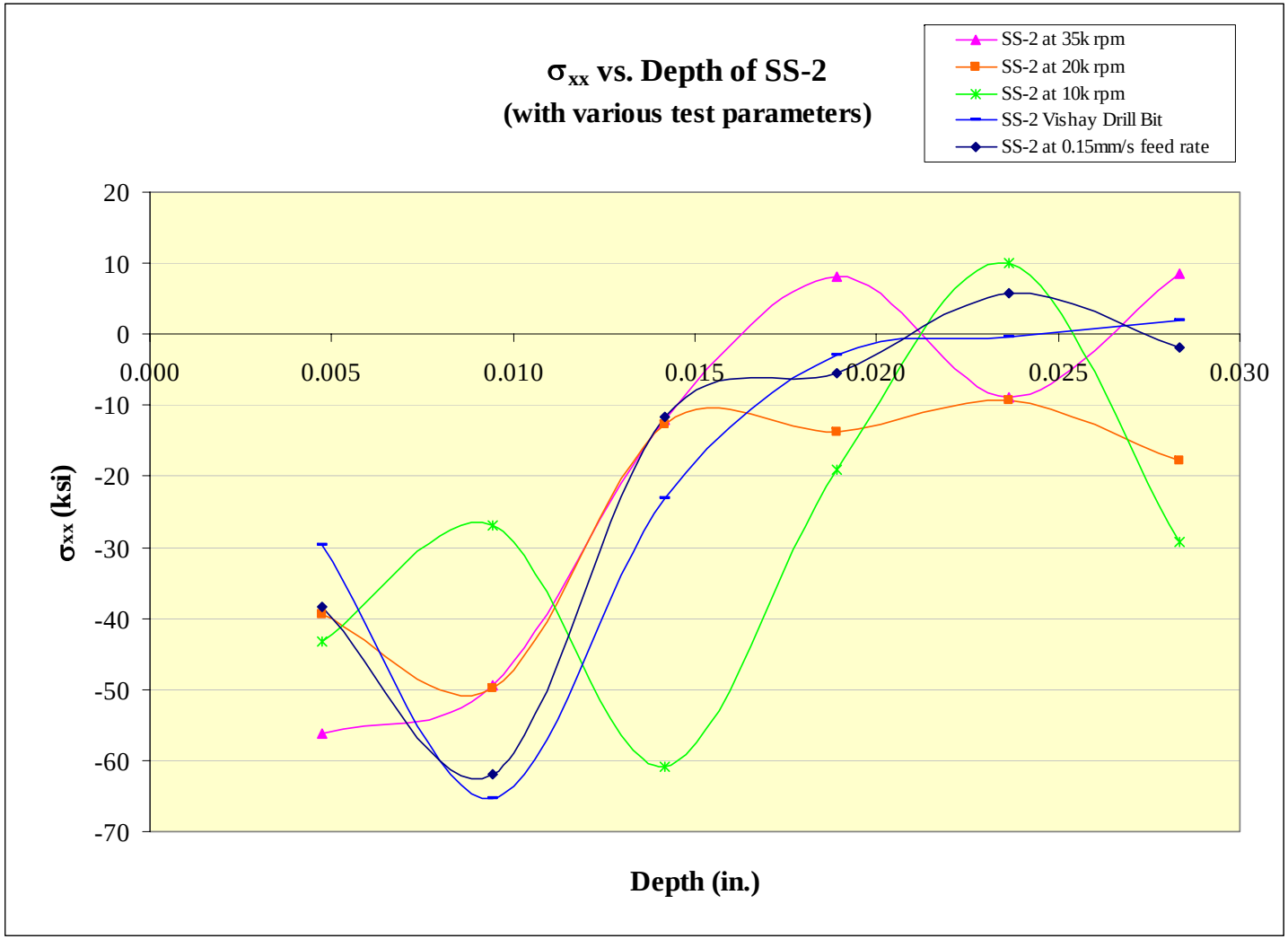

Figure 47: σ_{xx} versus depth curves of SS-2 – ESPI hole drilling method.

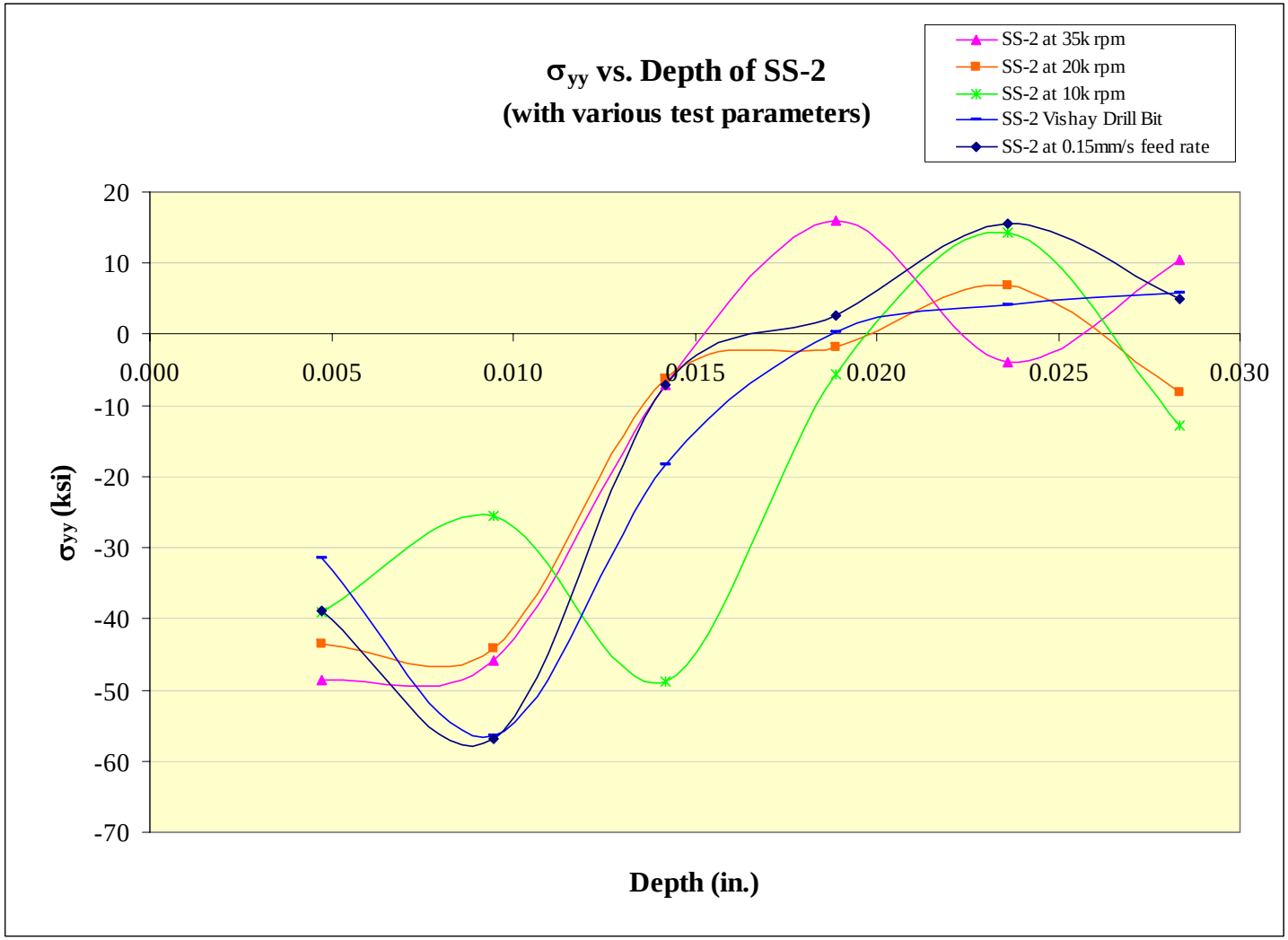

Figure 48: σ_{yy} versus depth curves of SS-2 – ESPI hole drilling method.

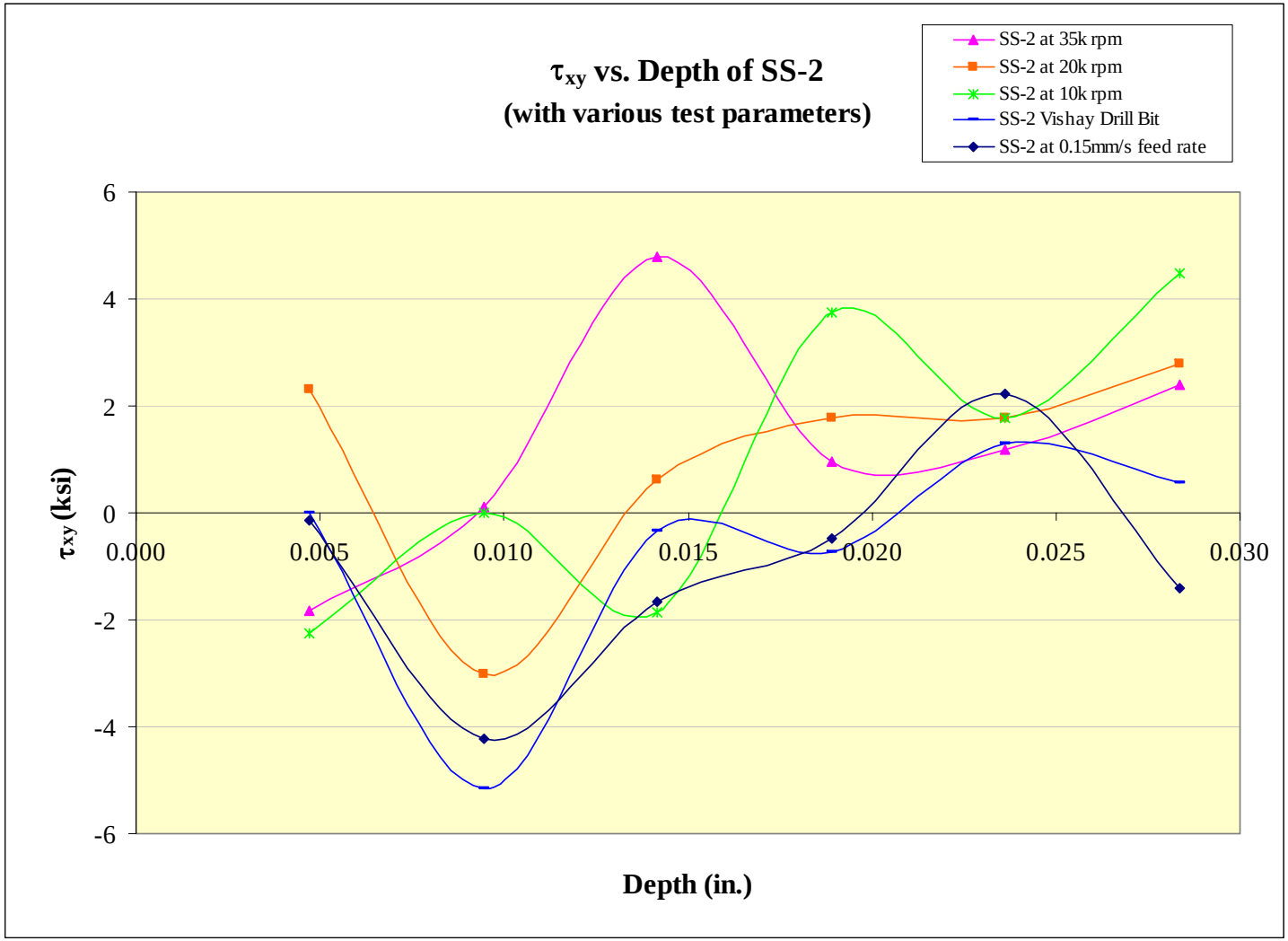

Figure 49: τ_{xy} versus depth curves of SS-2 – ESPI hole drilling method.

In Figures 41-43, the tests performed at drill speed of 20k rpm were done at locations where no SGHD surface preparation had been done to the point of interest and its surrounding area. The tests performed at 35k rpm were done on point B (as described in Section 6.1), where some SGHD surface preparations had been done on its surrounding area. Unlike the unblasted samples, the figures demonstrate that at 35k rpm, the samples share somewhat similar σ_{xx}, σ_{yy}, and τ_{xy} profiles. However, the drill speed of 20k rpm seems to yield better results; most samples show more similarities in their σ_{xx}, σ_{yy}, and τ_{xy} profiles.

Figures 41-43 also indicate that different surface conditions yield different results on an ESPI system. It is apparent that measurements at point B on each sample yielded higher compressive stress close to the surface compared to the ones taken at random locations where no surface preparation had been done on their surroundings. This situation is also observed for the unblasted samples in Figures 31-33.

Since the results of SS-1 to SS-5 indicated that a drill speed of 20k rpm worked better than 35k rpm, all measurements on SS-6 to SS-10 were done using a drill speed of 20k rpm. Figures 44 and 45 show that the σ_{xx} and σ_{yy} profiles of SS-6, SS-7, SS-8, and SS-9 are in good agreement. Since some rigid body motions were detected during the SS-10 measurement, it is expected that its results are not as reliable as the others.

Identical to tests done on sample US-2, several measurements were also done on SS-2 with various test parameters, in an effort to find the appropriate drill speed, drill feed rate, and drill bit type. Unlike the unblasted samples, in general, Figures 46-48 show that each setting yielded σ_{xx} and σ_{yy} profiles that are somewhat in good agreement to each other. However, at this point, the appropriate test parameters for this particular

material remain unknown; further study of this is beyond the scope of this research. Note that the PRISM-RS beta version software was used to analyze these results.

6.3.3 Discussions

This method indicated that σ_{xx} for the unblasted samples were generally compressive close to the surface, but not as high as the σ_{xx} compressions for the sandblasted samples. The σ_{yy} stresses for the unblasted samples were in the low compressive to low tensile range. For the sandblasted samples, σ_{yy} was compressive close to the surface, as expected, and generally decreased with depth to eventually become tensile between depths of 0.013 in.- 0.021 in.

The magnitudes of shear stresses (τ_{xy}) in the unblasted samples were about constant throughout the whole depth, and generally very small. Shear stresses in the sandblasted samples were not constant with depth. Most curves showed that a "dip" occurred at a depth of 0.0090 in. However, shear stresses remained small throughout the hole depth.

Figures 31-33 and 41-43 indicate that surface conditions also affect the stress measured by an ESPI system. Both types of sample (unblasted and sandblasted) showed that higher compressive stresses were present at locations where some surface preparations had been done.

In this research, a drill speed of 20k rpm yielded better results on both sample types. The σ_{xx} and σ_{yy} profiles obtained from drilling at 20k rpm were in better agreement to each other than those obtained from drilling at 35k rpm. Currently there is no standard available which specifies the appropriate test parameters of the ESPI hole

drilling method for measuring residual stress on a particular material. Future studies are needed to develop a standard that is theoretically and experimentally well-proven.

6.4 COMPARISON OF RESULTS

Each method samples a different volume of material at different depths into the surface. The X-ray diffraction method is especially different than the other two methods, since it only measures stresses at a depth very close to the surface (virtually zero depth). For this reason, no direct comparisons can be made between X-ray diffraction and strain-gage hole drilling, as well as between X-ray diffraction and ESPI hole drilling. Therefore, direct comparisons can only be made between the strain-gage hole drilling and ESPI hole drilling methods.

In this research, X-ray diffraction was only used to determine how stresses varied along the length of each sample. The results were verified by a couple of measurements done on two samples (one unblasted and one sandblasted) using the ESPI hole drilling method. On each sample, both measurements were identical in surface condition, drill speed, drill bit type, and drilling increments. The only test parameter that was different between the measurements was the drill feed rate; one being a drill feed rate of 0.05mm/s, and the other a rate of 0.15mm/s.

6.4.1 Unblasted Samples

Comparison graphs of the unblasted samples are shown on Figures 50-58. There are three plots for each sample: σ_{xx} versus depth, σ_{yy} versus depth, and τ_{xy} versus depth. Note that the X-ray diffraction results are also plotted on all graphs of σ_{xx} versus depth.

However, their presence is not intended for direct comparisons to the strain-gage hole drilling and ESPI hole drilling results. It should be kept in mind that XRD point A corresponds to the SGHD location, while XRD point B corresponds to the ESPI hole drilling at 35k rpm location for samples US-1 to US-5, and ESPI hole drilling at 20k rpm location for samples US-6 to US-10. In addition, sample US-8 is excluded here because of unreliable results (some excess glue was present from strain-gage hole drilling surface preparation on location surface).

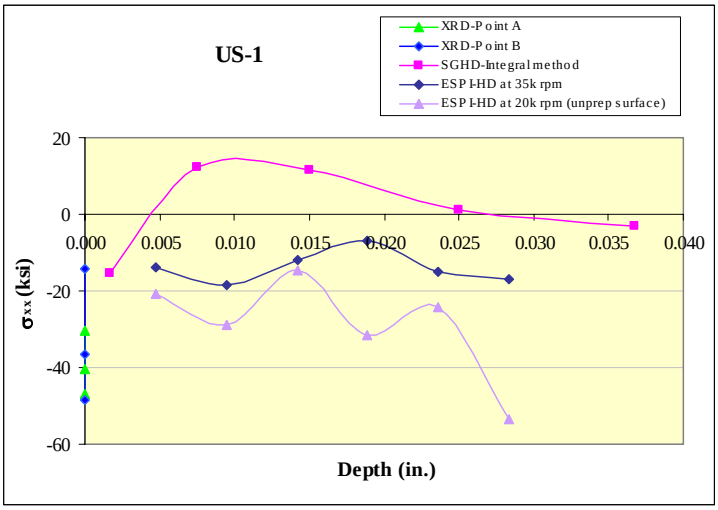

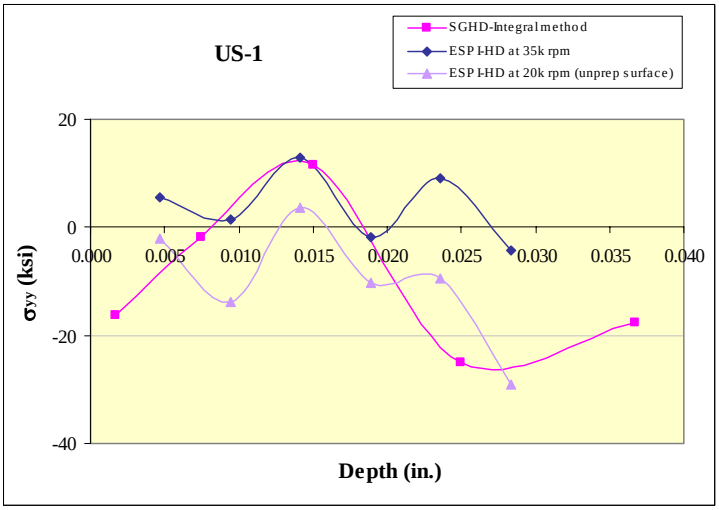

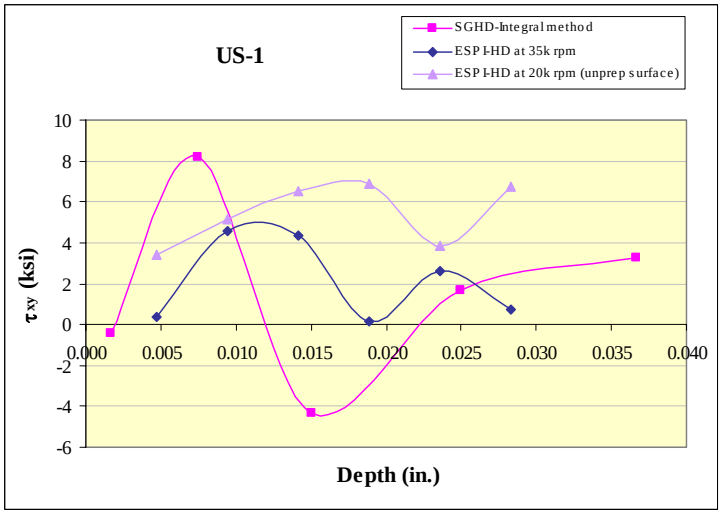

Figure 50: Comparison graphs of US-1.

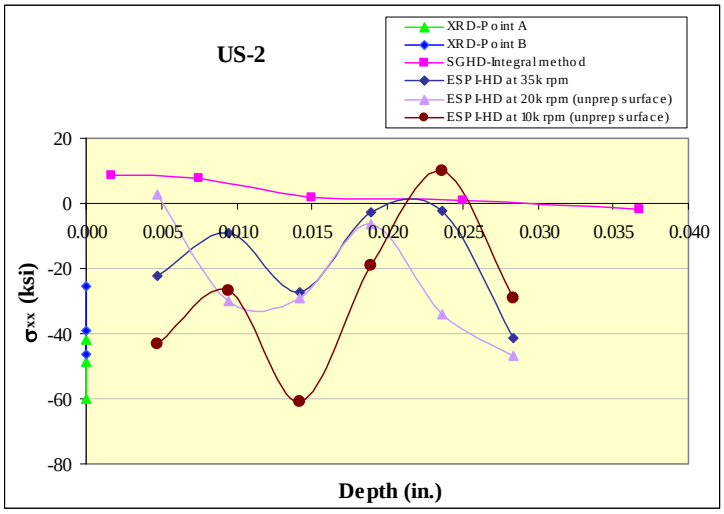
US-2
XRD-Point A
XRD-Point B
SGHD-Integral method
ESPI-HD at 35k rpm
ESPI-HD at 20k rpm (unprep surface)
ESPI-HD at 10k rpm (unprep surface)
σxx (ksi)
Depth (in.)

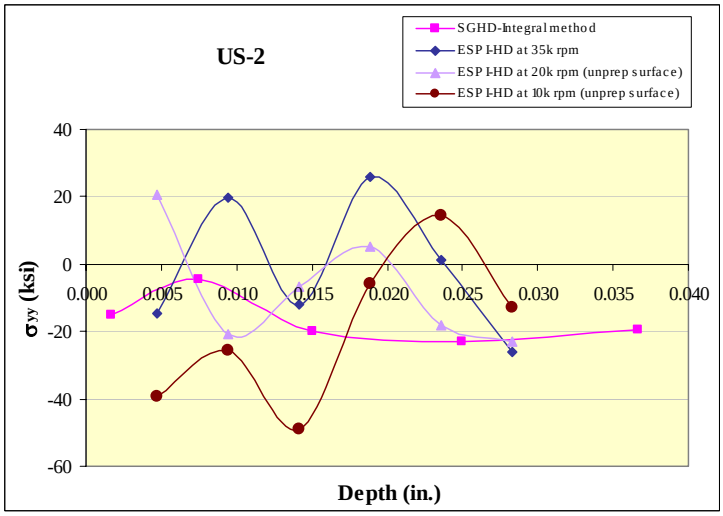
US-2
SGHD-Integral method
ESPI-HD at 35k rpm
ESPI-HD at 20k rpm (unprep surface)
ESPI-HD at 10k rpm (unprep surface)
σyy (ksi)
Depth (in.)

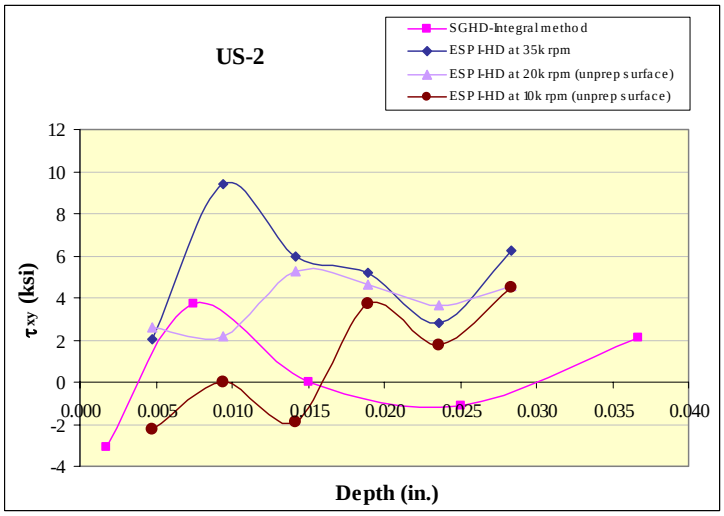
US-2
SGHD-Integral method
ESPI-HD at 35k rpm
ESPI-HD at 20k rpm (unprep surface)
ESPI-HD at 10k rpm (unprep surface)
τxy (ksi)
Depth (in.)

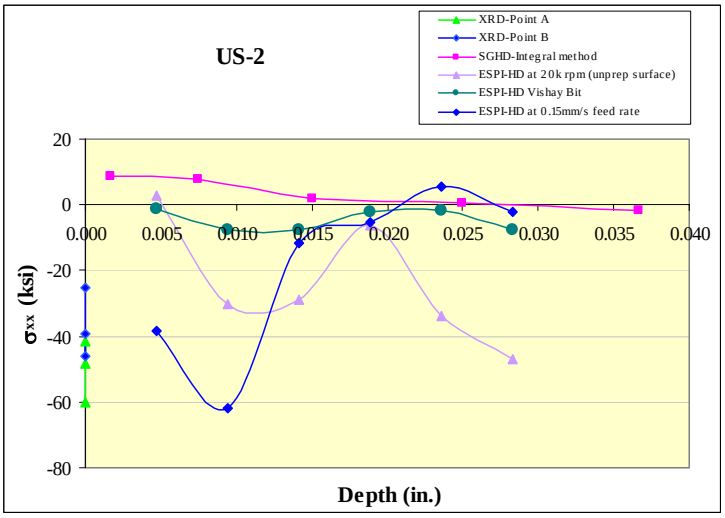

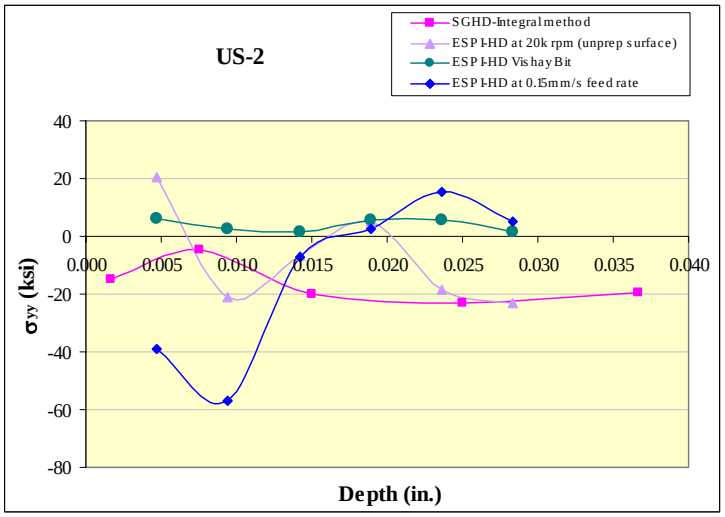

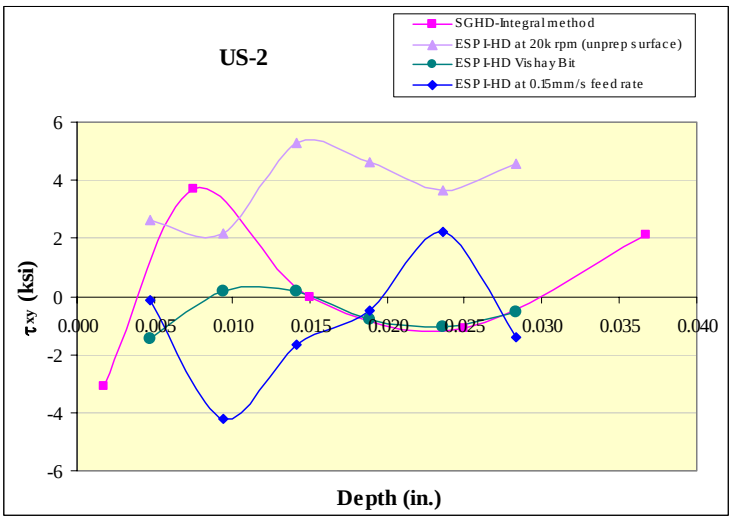

Figure 51: Comparison graphs of US-2.

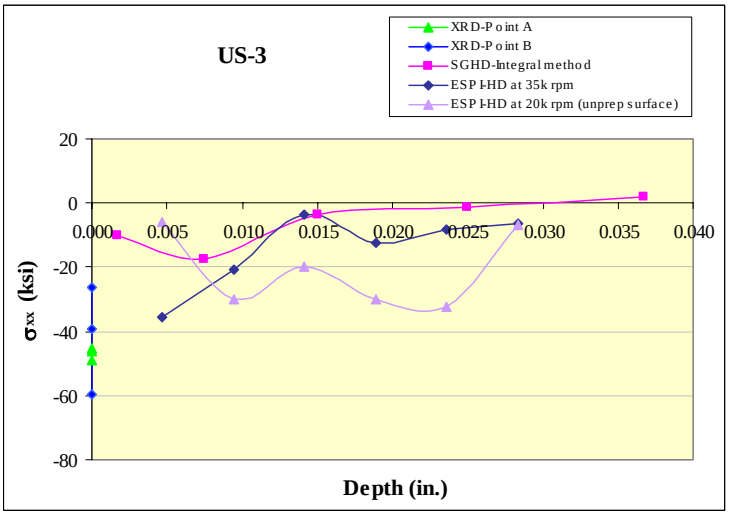

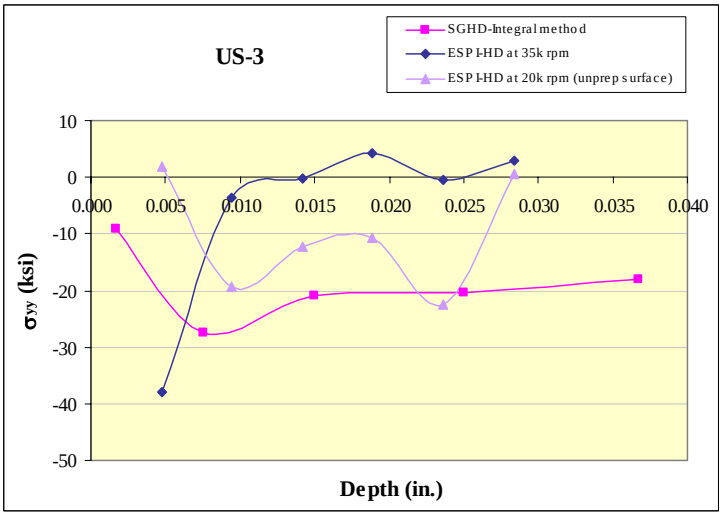

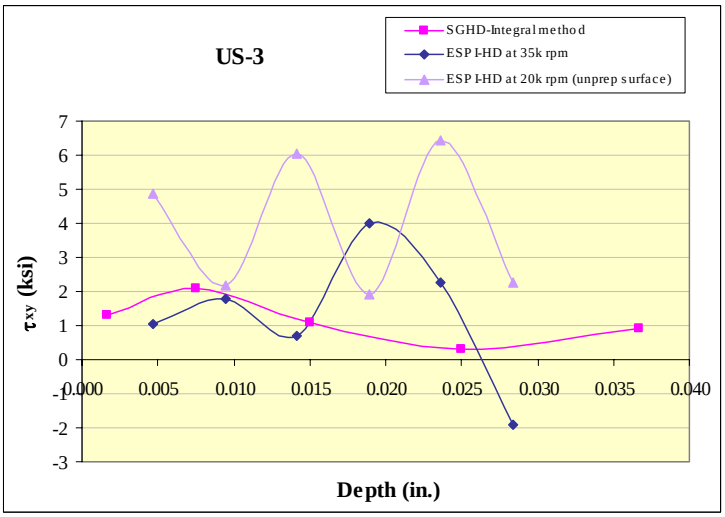

Figure 52: Comparison graphs of US-3.

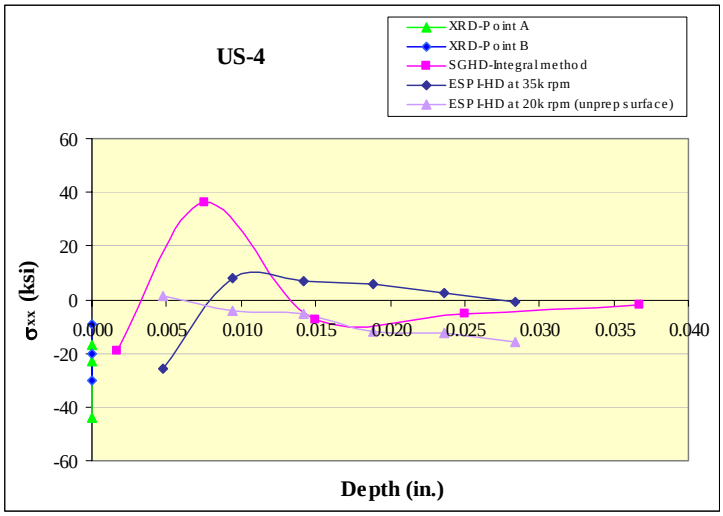

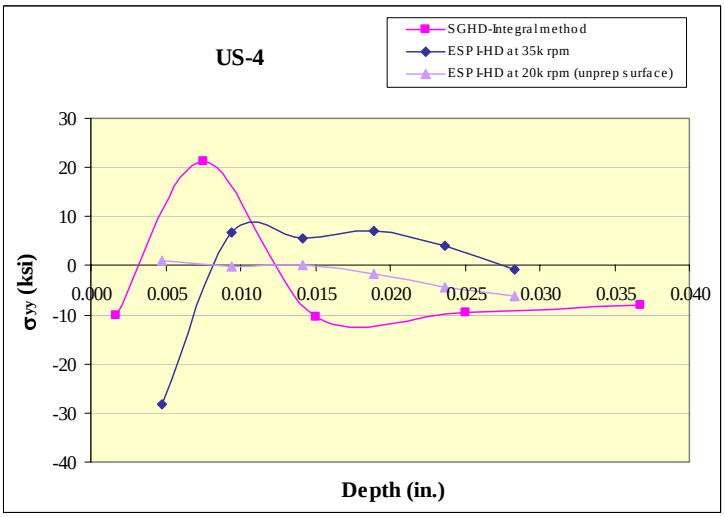

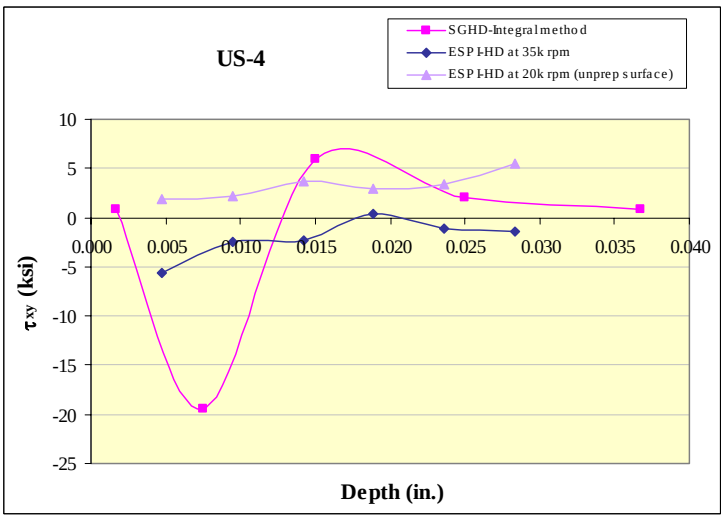

Figure 53: Comparison graphs of US-4.

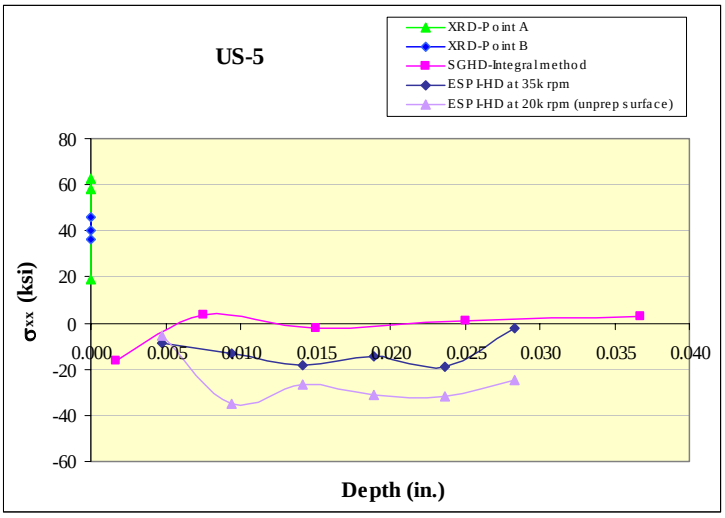

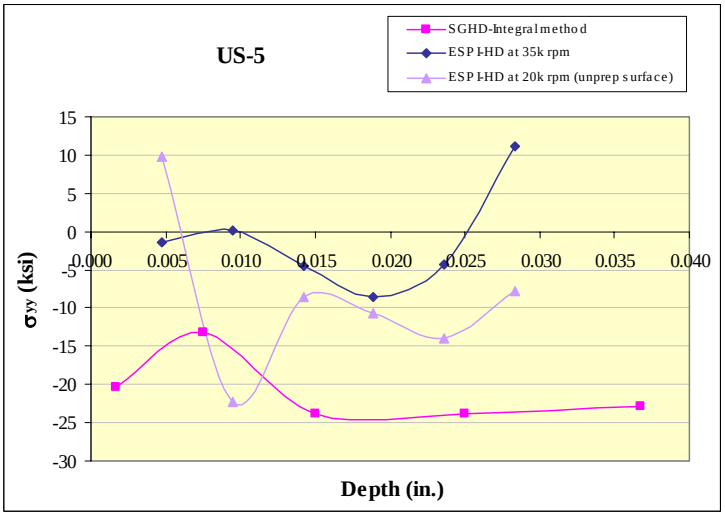

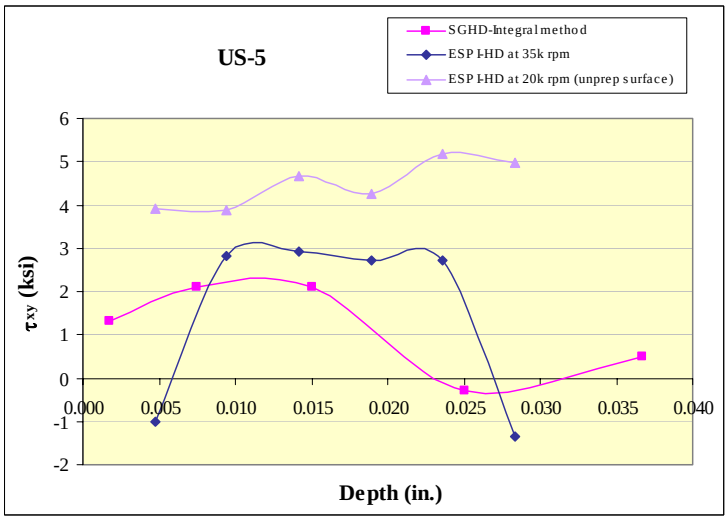

Figure 54: Comparison graphs of US-5.

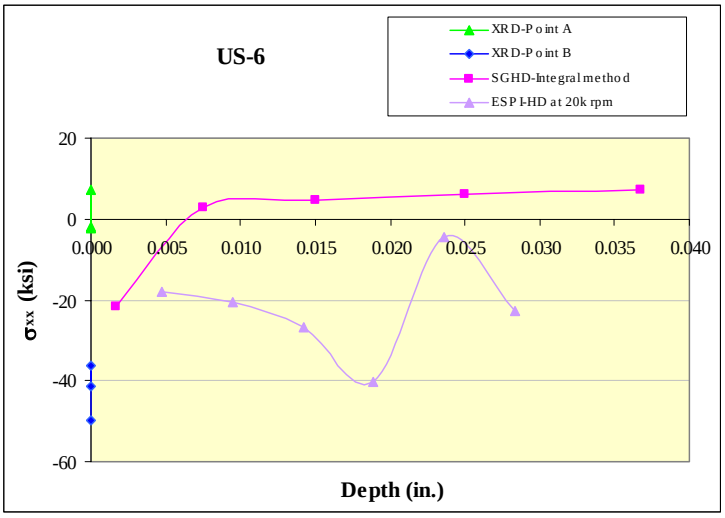

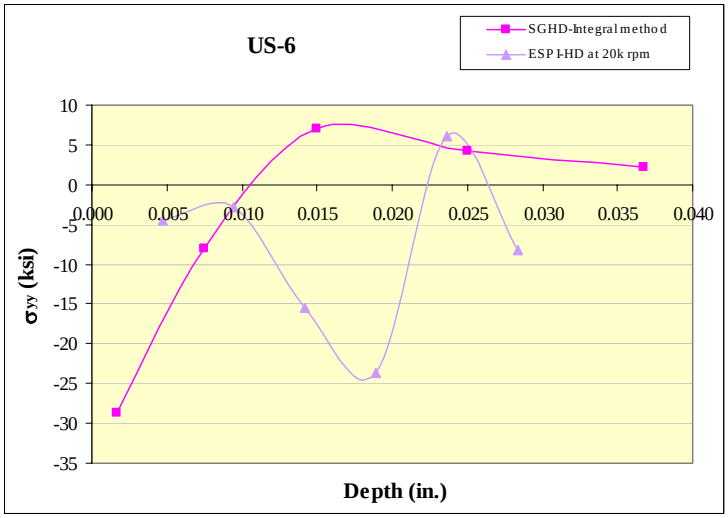

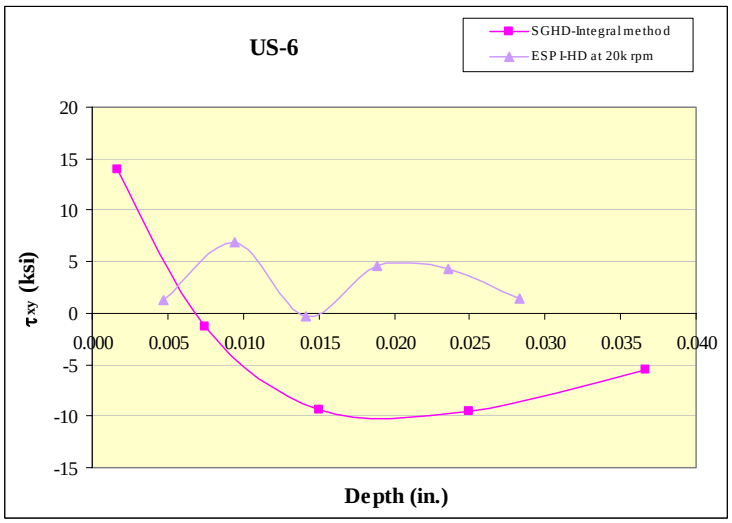

Figure 55: Comparison graphs of US-6.

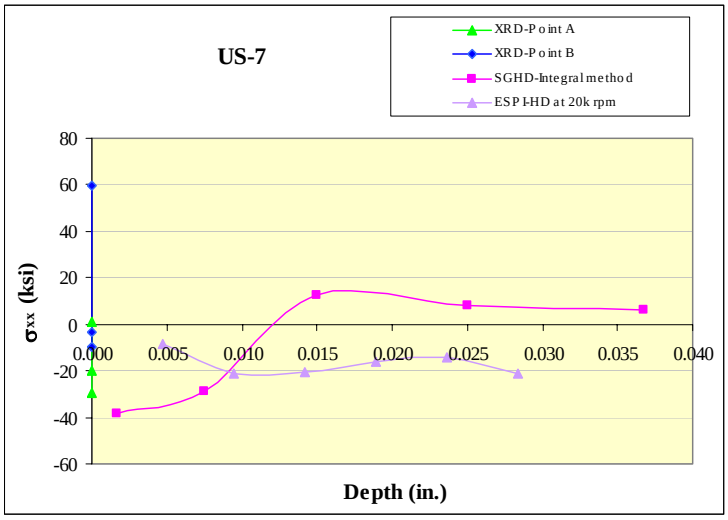

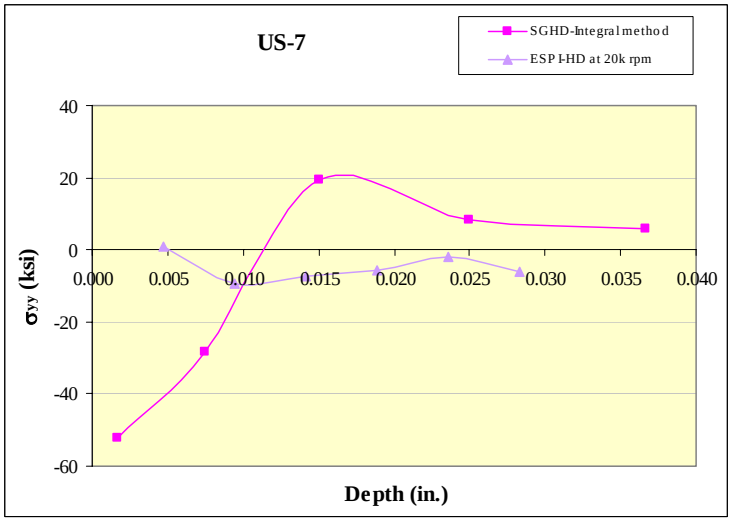

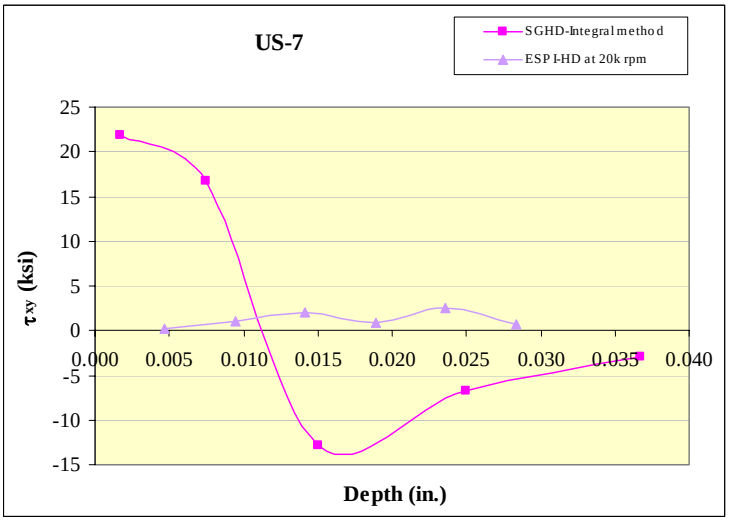

Figure 56: Comparison graphs of US-7.

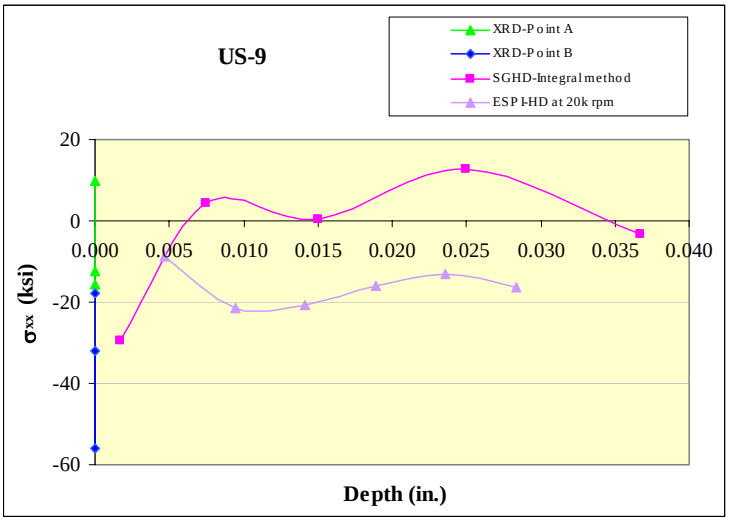

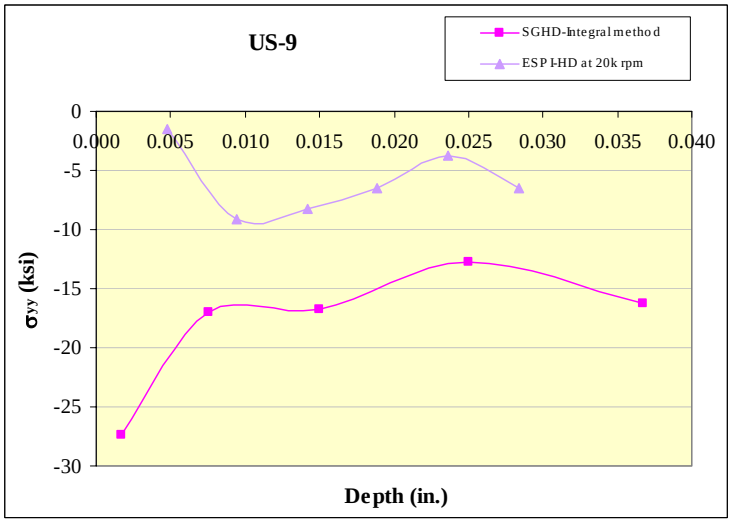

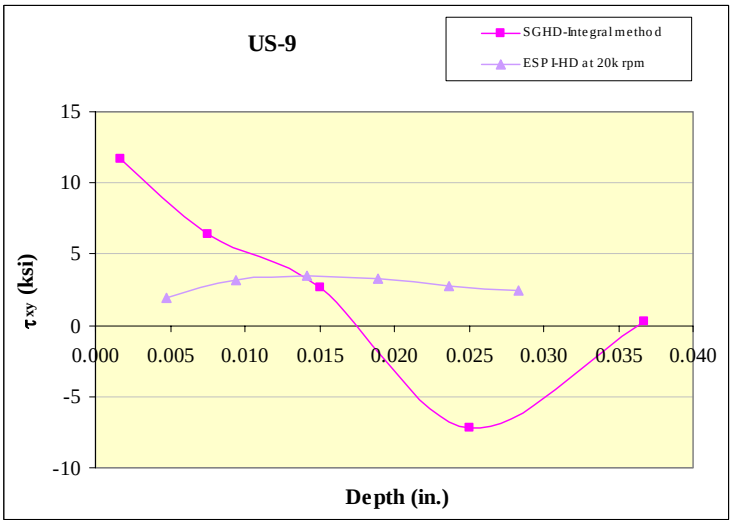

Figure 57: Comparison graphs of US-9.

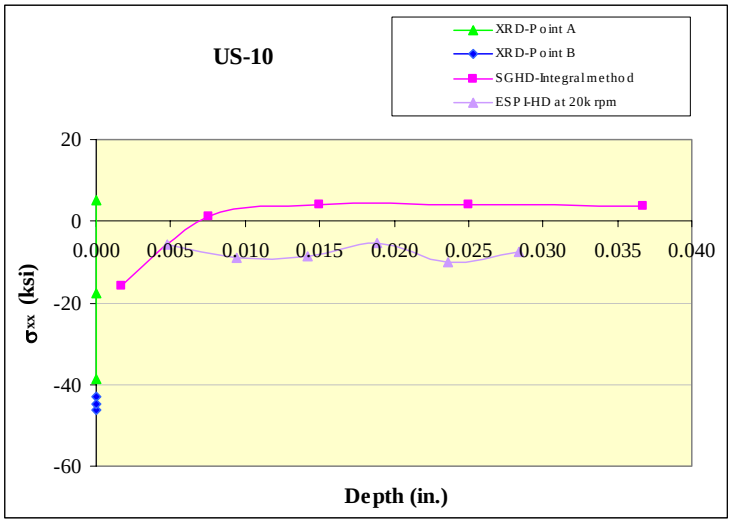

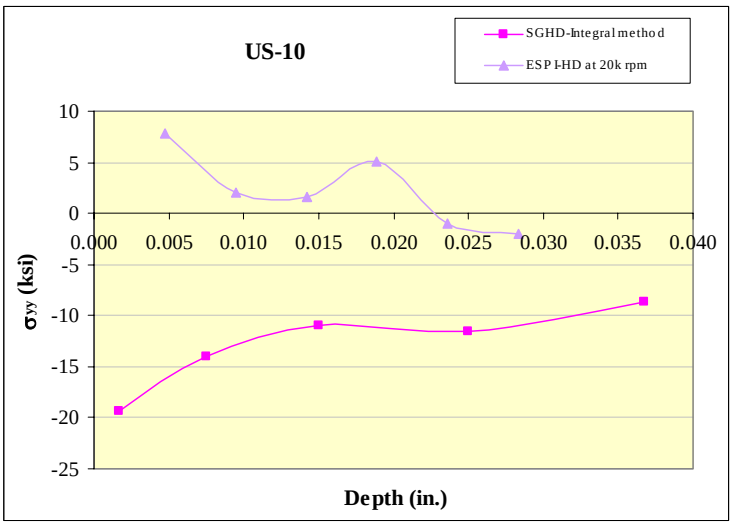

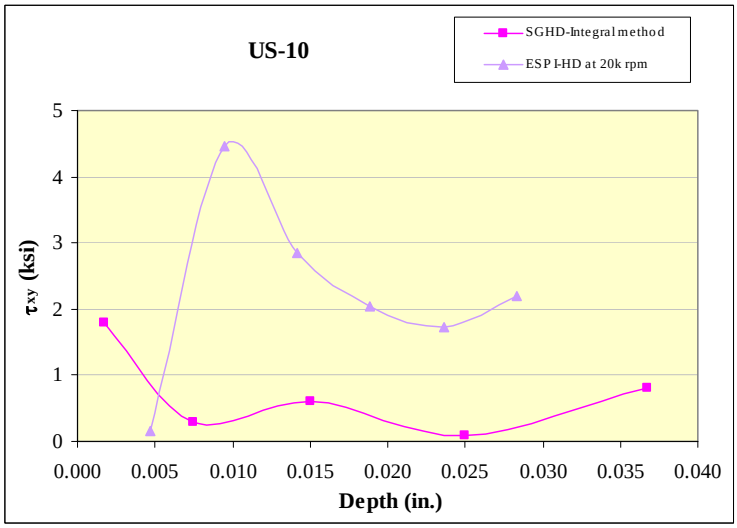

Figure 58: Comparison graphs of US-10.

Figures 50-58 show that the strain-gage hole drilling and ESPI hole drilling results are generally not in good agreement. This may have been caused by one or more of the following test parameters:

1. PRISM-RS beta version software,
2. Difference in surface condition,
3. Type of drill bit used,
4. Drill speed,
5. Drill feed rate, or
6. Different drilling increments.

In general, the X-ray diffraction results show that stress varied along the length of the sample. This was confirmed by the two measurements done using the ESPI hole drilling results on US-2. The first measurement was done at a drill speed of 20k rpm, drill feed rate of 0.05mm/s, and at a location where there had been no surface preparation. The second measurement was done at a drill speed of 20k rpm, drill feed rate of 0.15mm/s, and at a location where there had been no surface preparation. Both measurements also used the same type of drill bit, which is the two-fluted end mill with a diameter of 0.0625 in. It can be observed from Figure 51 that the stress profiles at both locations vary.

Figure 51 also demonstrates that using different type of drill bits on an ESPI system affected the stress results greatly. Using the Vishay drill bit with diameter of 0.062 in. on the ESPI system may generate results that are in better agreement to those of the strain-gage hole drilling method.

The strain-gage hole drilling technique, combined with the integral method for analyses of residual stress measurements that vary with depth, is a proven technology. With this in mind, the unblasted specimens generally had a surface stress σ_{xx} of about -15 ksi, which then dropped to near zero at increasing depth. The σ_{yy} stress near the surface averaged to about -20 ksi and decreased to an average of -10 ksi up to a depth of 0.0075 in., and then increased back to about -20 ksi at increasing depth. Finally, the average shear stress τ_{xy} near the surface was generally very small. Its magnitude tended to stay constant throughout the whole depth.

6.4.2 Sandblasted Samples

Comparison graphs of the sandblasted samples are shown on Figures 59-67. There are three plots for each sample: σ_{xx} versus depth, σ_{yy} versus depth, and τ_{xy} versus depth. Note that the X-ray diffraction results are also plotted on all graphs of σ_{xx} versus depth. However, their presence are not intended for direct comparisons to the strain-gage hole drilling and ESPI hole drilling results. It should be kept in mind that XRD point A corresponds to the SGHD location, while XRD point B corresponds to the ESPI hole drilling at 35k rpm location for samples SS-1 to SS-5, and ESPI hole drilling at 20k rpm location for samples SS-6 to SS-9. Sample SS-10 is excluded here because of unreliable results; some rigid body motions were detected during the measurement.

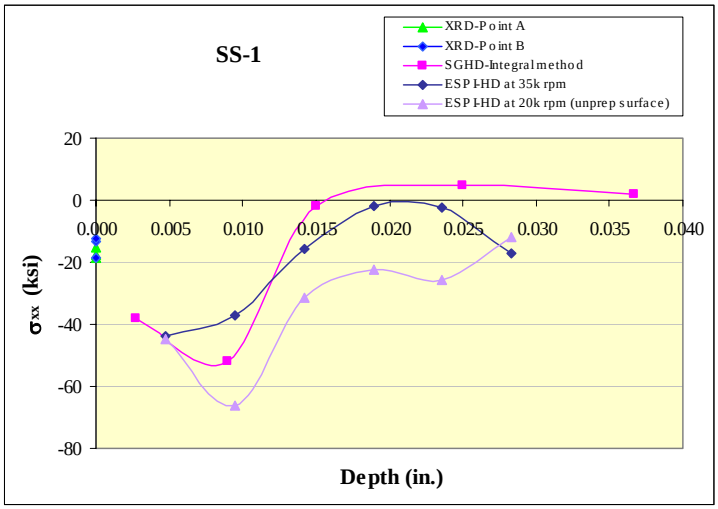

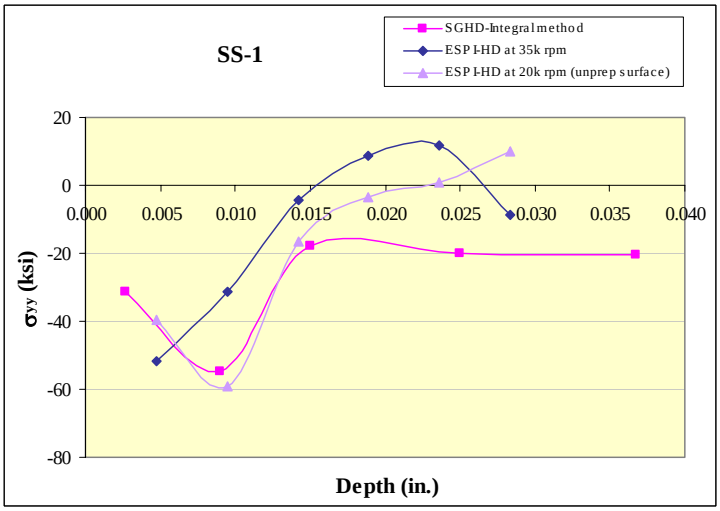

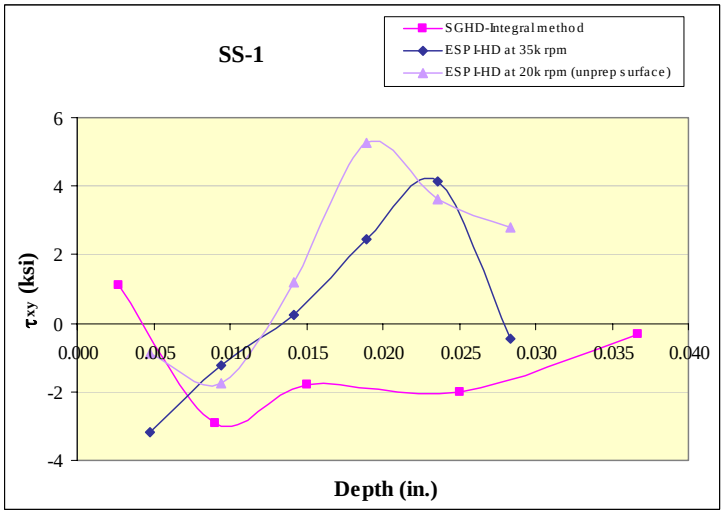

Figure 59: Comparison graphs of SS-1.

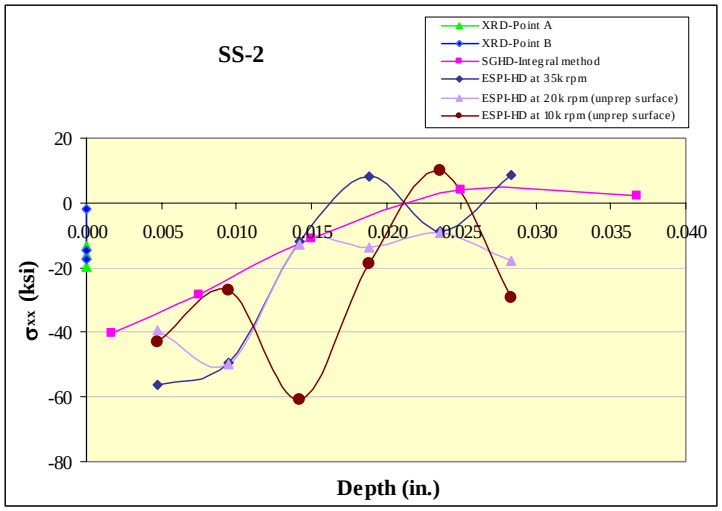
SS-2
XRD-Point A
XRD-Point B
SGHD-Integral method
ESPI-HD at 35k rpm
ESPI-HD at 20k rpm (unprep surface)
ESPI-HD at 10k rpm (unprep surface)
20
0
-20
-40
-60
-80
0.000
0.005
0.010
0.015
0.020
0.025
0.030
0.035
0.040
σxx (ksi)
Depth (in.)

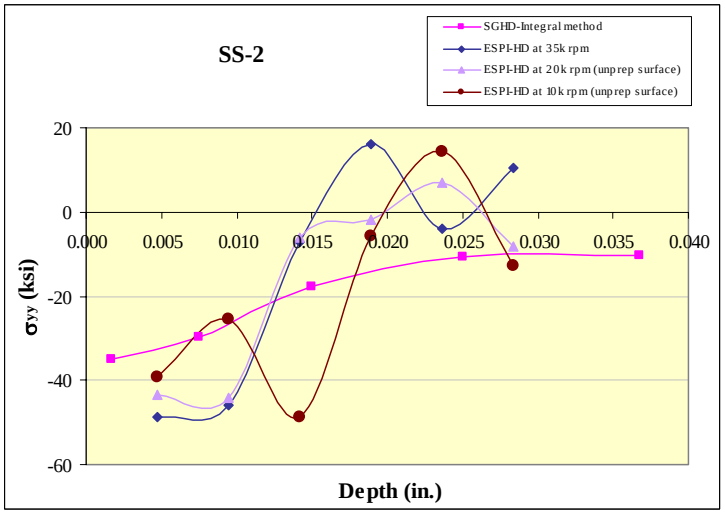
SS-2
SGHD-Integral method
ESPI-HD at 35k rpm
ESPI-HD at 20k rpm (unprep surface)
ESPI-HD at 10k rpm (unprep surface)
20
0
-20
-40
-60
0.000
0.005
0.010
0.015
0.020
0.025
0.030
0.035
0.040
σyy (ksi)
Depth (in.)

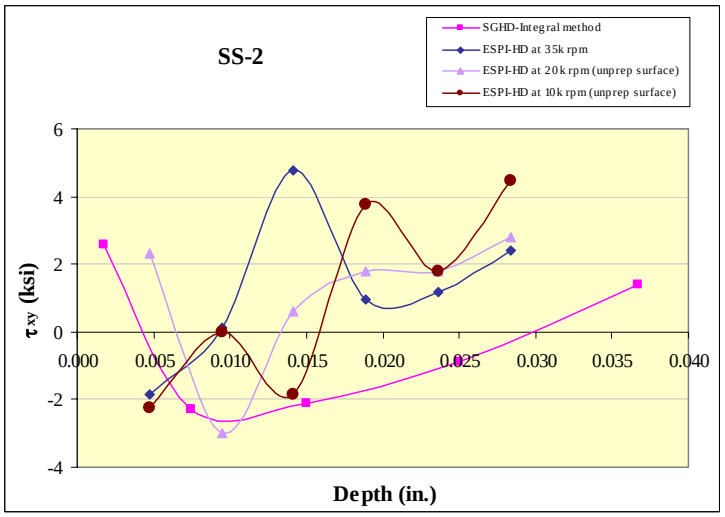
SS-2
SGHD-Integral method
ESPI-HD at 35k rpm
ESPI-HD at 20k rpm (unprep surface)
ESPI-HD at 10k rpm (unprep surface)
6
4
2
0
-2
-4
0.000
0.005
0.010
0.015
0.020
0.025
0.030
0.035
0.040
τxy (ksi)
Depth (in.)

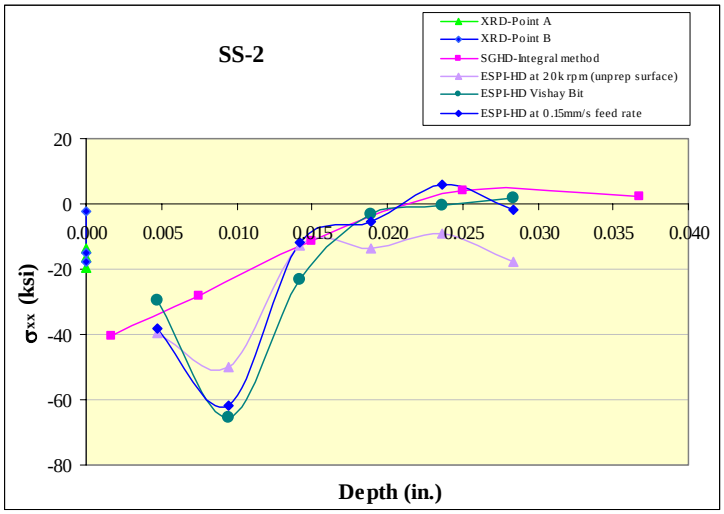

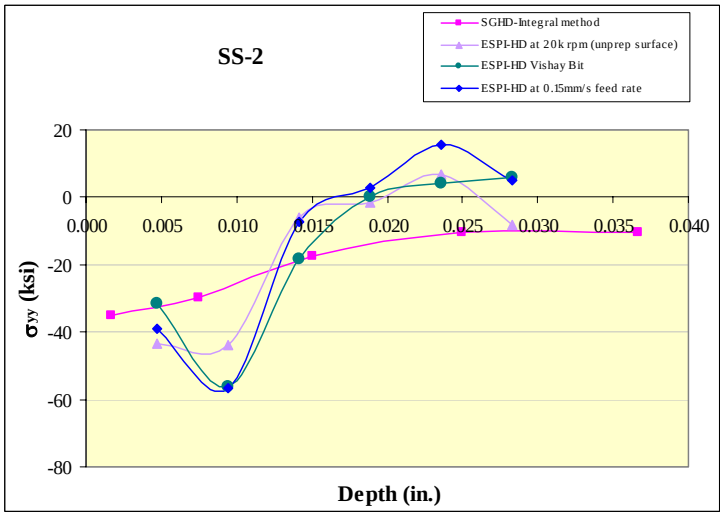

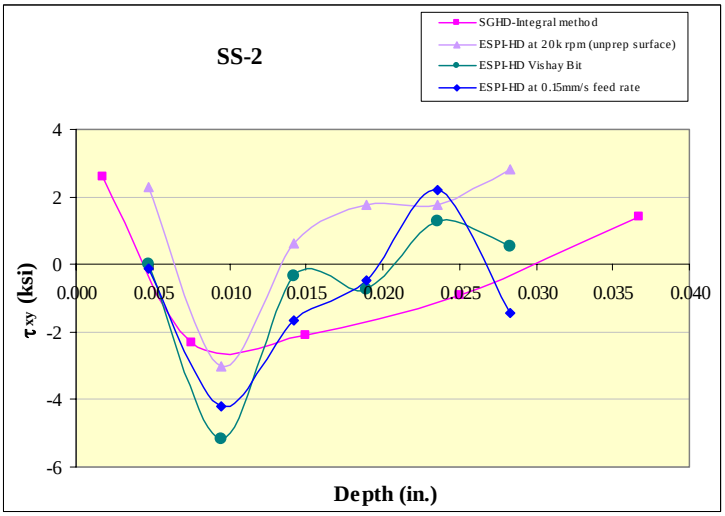

Figure 60: Comparison graphs of SS-2.

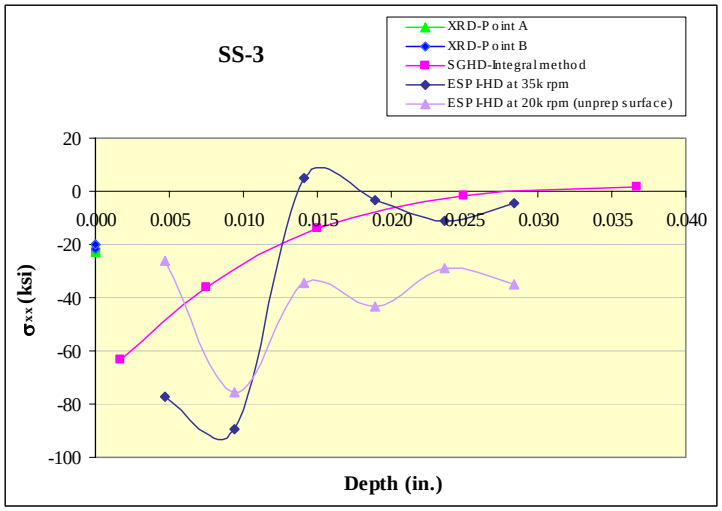

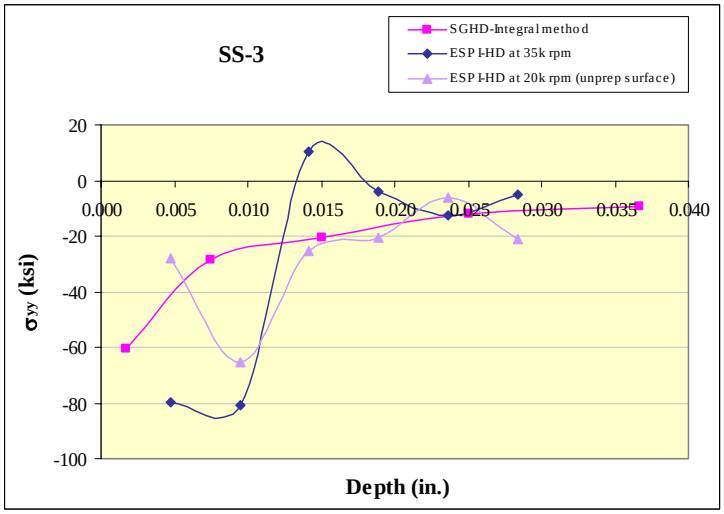

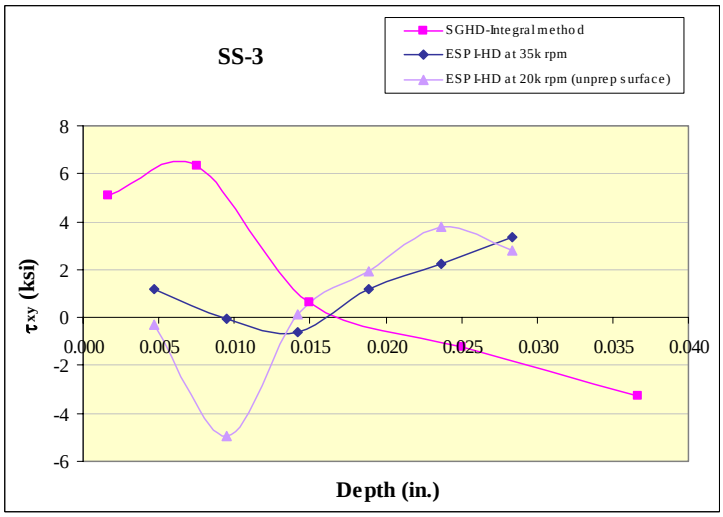

Figure 61: Comparison graphs of SS-3.

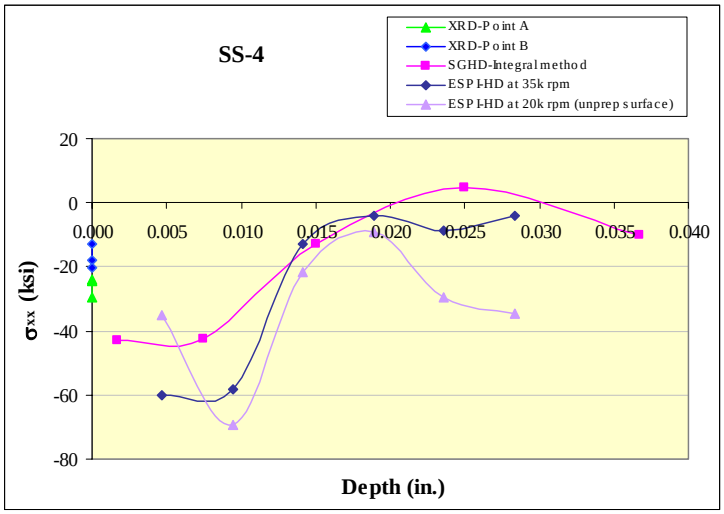

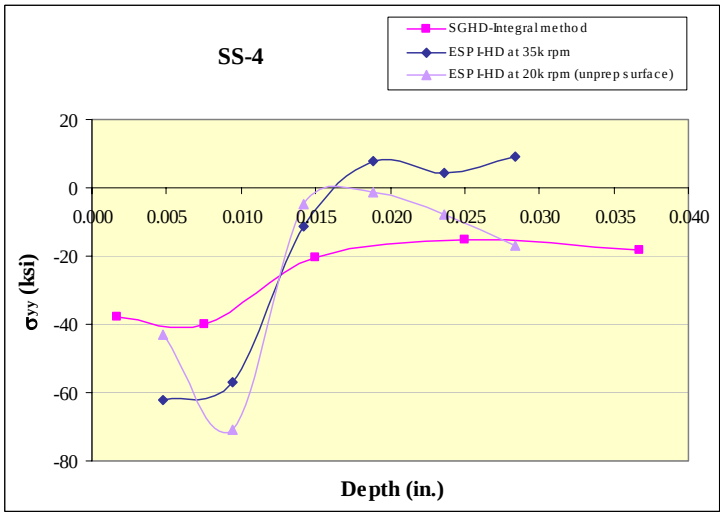

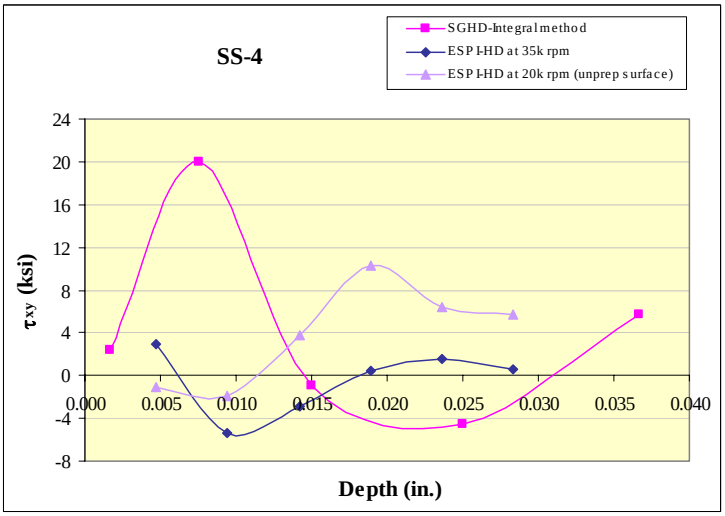

Figure 62: Comparison graphs of SS-4.

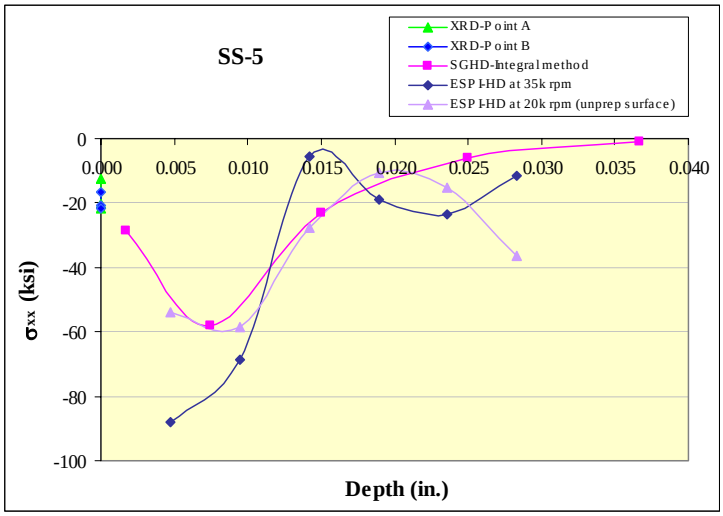

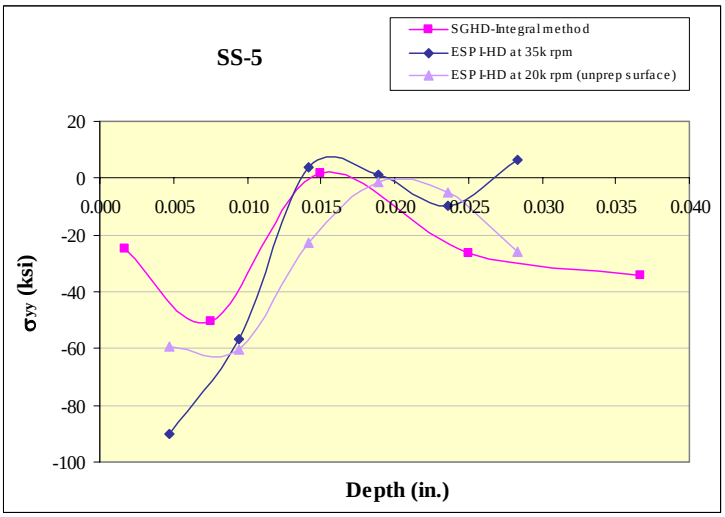

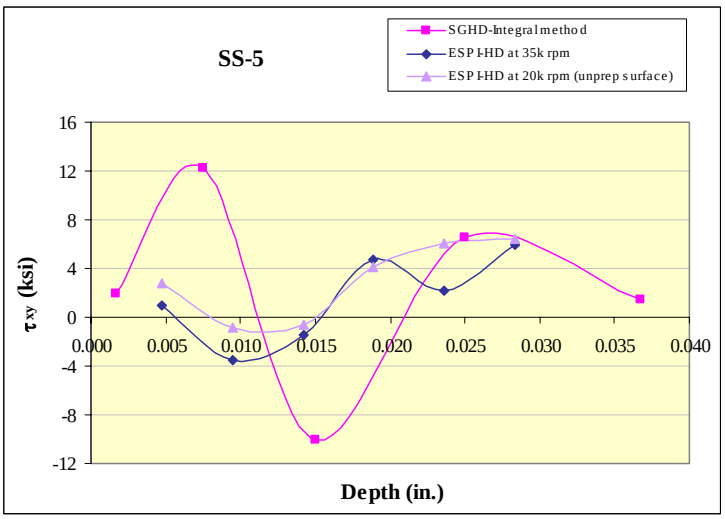

Figure 63: Comparison graphs of SS-5.

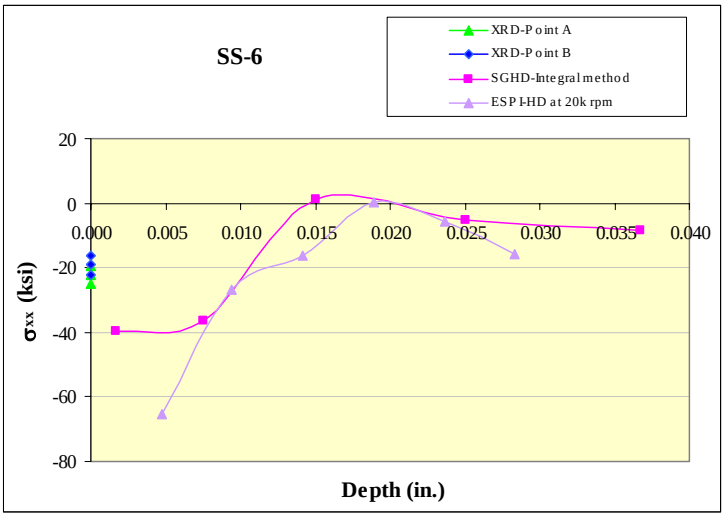

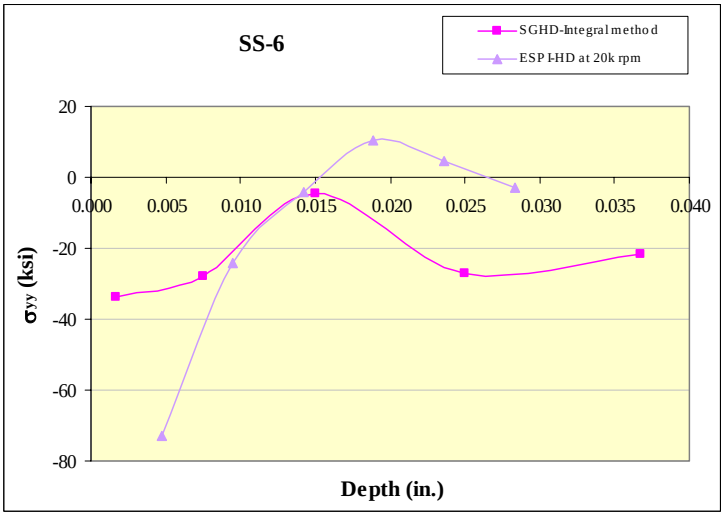

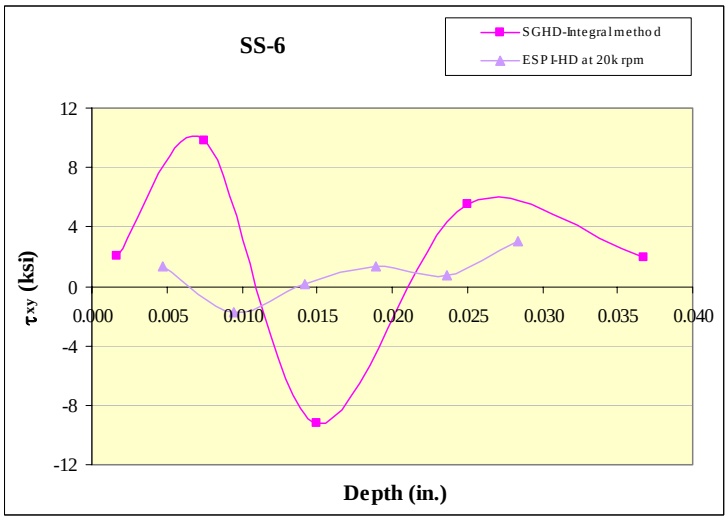

Figure 64: Comparison graphs of SS-6.

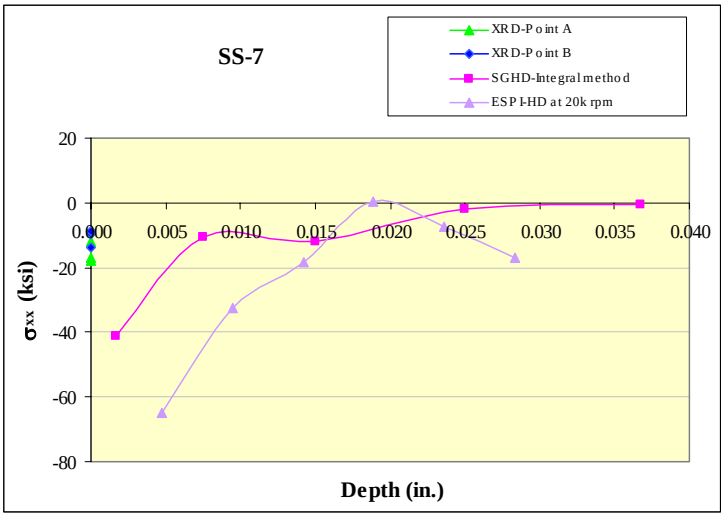

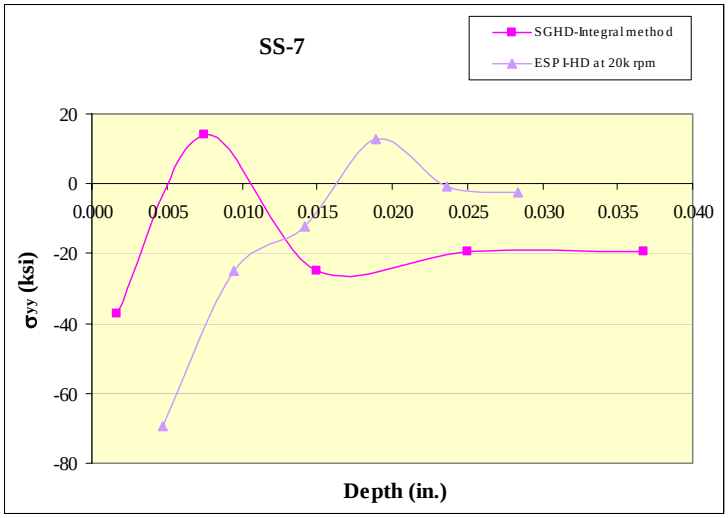

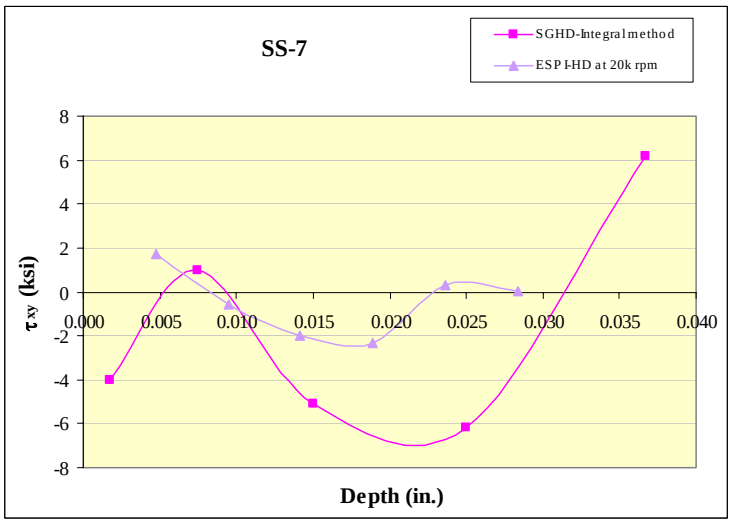

Figure 65: Comparison graphs of SS-7.

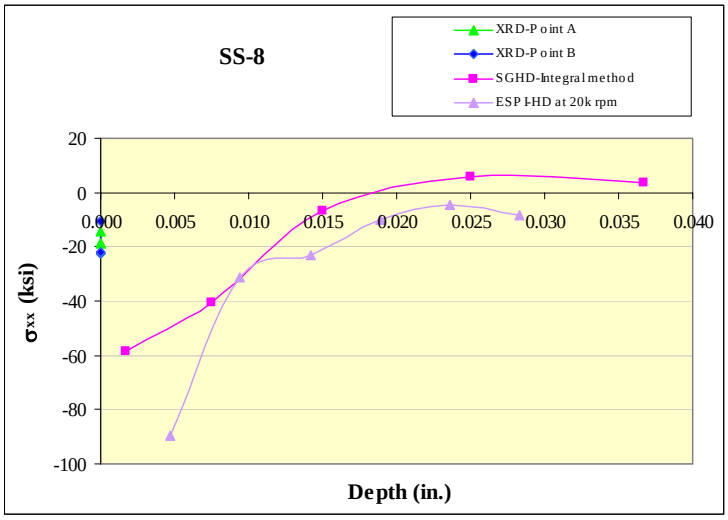

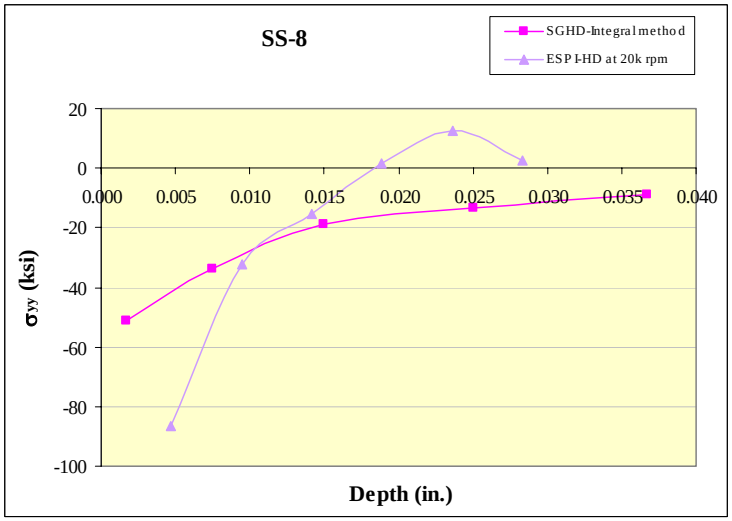

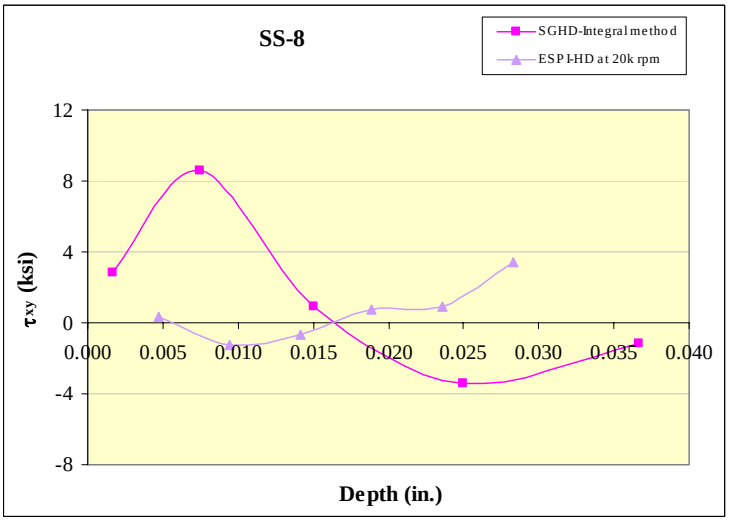

Figure 66: Comparison graphs of SS-8.

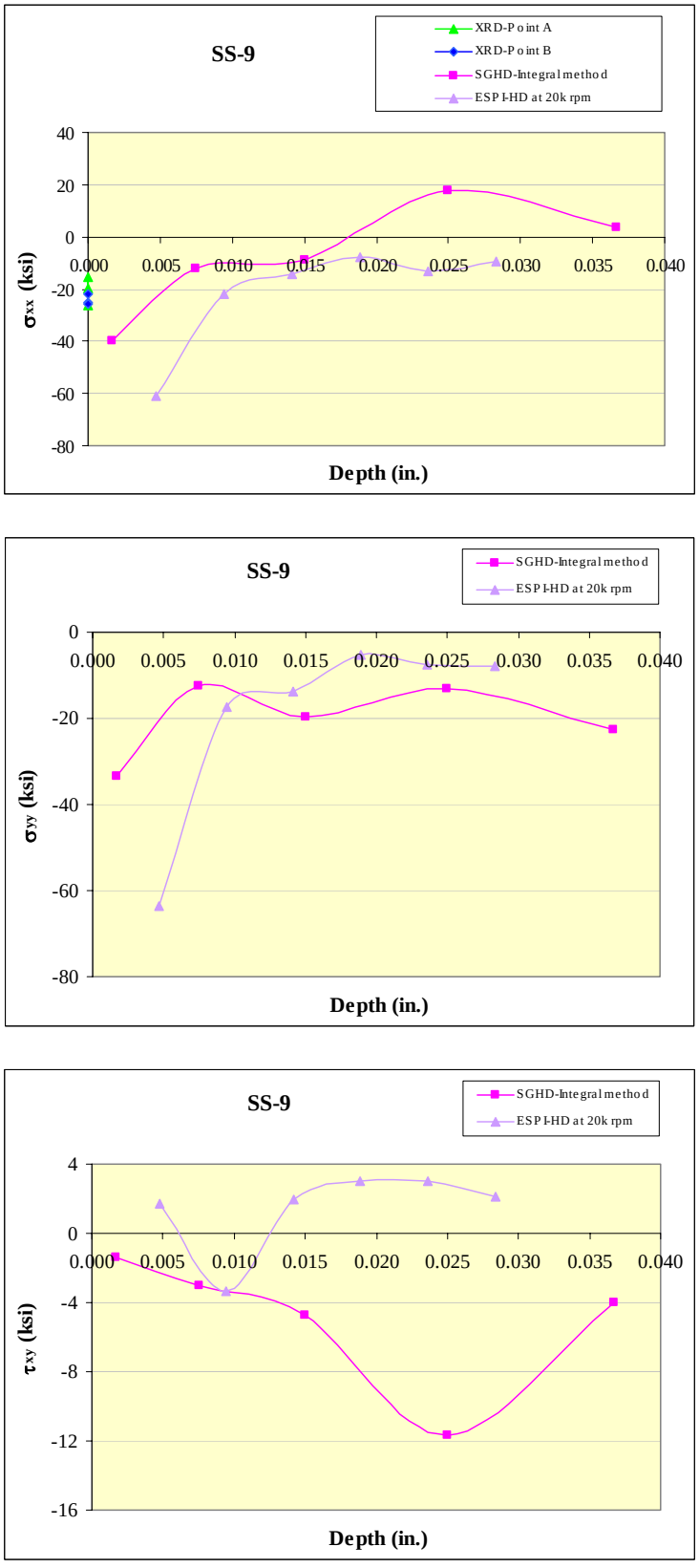

Figure 67: Comparison graphs of SS-9.

Figures 59-67 show that the strain-gage hole drilling and ESPI hole drilling results are generally not in a very good agreement to one another. This may have been caused by one or more of the following test parameters:

1. PRISM-RS beta version software,
2. Difference in surface condition,
3. Type of drill bit used,
4. Drill speed,
5. Drill feed rate, or
6. Different drilling increments.

In general, the X-ray diffraction results show that stresses along the length of the sample were quite uniform. This was confirmed by the two measurements done using the ESPI hole drilling results on SS-2. The first measurement was done at a drill speed of 20k rpm, drill feed rate of 0.05mm/s, and at a location where there had been no surface preparation. The second measurement was done at a drill speed of 20k rpm, drill feed rate of 0.15mm/s, and at a location where there had been no surface preparation. Both measurements also used the same type of drill bit, which is the two-fluted end mill with a diameter of 0.0625 in. It can be observed from Figure 60 that the stress profiles at both locations are somewhat in good agreement to one another.

Figure 60 demonstrates that using different type of drill bits on an ESPI system affected the stress results. Using the Vishay drill bit with diameter of 0.062 in. on the ESPI system may generate results that are in better agreement to those of the strain-gage hole drilling method.

Since the strain-gage hole drilling method analyzed by the integral method is a proven technique, the residual stress measured in the sandblasted samples indicate that there was an average σ_{xx} stress of about -45 ksi near the surface. This stress then dropped to an average of zero as depth increased. The σ_{yy} stress near the surface averaged to about -35 ksi and decreased to an average of -20 ksi at increasing depth. Finally, the shear stress τ_{xy} near the surface averaged about 2 ksi and increased to an average of 7 ksi up to a depth of 0.0075 in., and then decreased back to near zero as depth increased.

7. CONCLUSIONS

Results of the strain-gage hole drilling method show that the unblasted and sandblasted samples had an average σ_{xx} near the surface of -15 ksi and -45 ksi, respectively. For both types of samples, the σ_{xx} decreased to near zero as depth increased. The ESPI hole drilling method results showed that the average σ_{xx} near the surface of the unblasted samples was -16 ksi, and -68 ksi for the sandblasted samples. For the sandblasted samples, σ_{xx} decreased to near zero as depth increased, while the stress profiles for the unblasted samples did not show any similar trend to one another; thus no generalization can be made. The results obtained from the strain-gage hole drilling and ESPI hole drilling methods in this research are not in good agreement. This may have been caused by one of, or the combination of, the following test parameters:

1. PRISM-RS beta version software,
2. Difference in surface condition,
3. Type of drill bit used,
4. Drill speed,
5. Drill feed rate, or
6. Different drilling increments.

Better comparisons between the results of strain-gage hole drilling and ESPI hole drilling methods resulted when the same type of drill bit was used for both methods.

Currently there is no standard available which specifies the appropriate test parameters for the ESPI hole drilling method applied to a particular material.

Results of the X-ray diffraction method (with four points on the d vs. $\sin^2\psi$ curves discarded) showed an average σ_{xx} of -34 ksi for the unblasted samples, and -19 ksi for the sandblasted samples. Since the X-ray diffraction method measures stresses at depths very close to the surface (virtually zero depth), no direct comparisons can be made between the X-ray diffraction and strain-gage hole drilling, as well as between X-ray diffraction and ESPI hole drilling. However, these X-ray diffraction results are inconsistent with the other two methods, since they indicate higher average compressive stresses on the unblasted samples than the sandblasted samples.

X-ray diffraction measurements can be more efficient, and results can be more reliable if a chromium anode is used in place of copper. A chromium anode has a longer wavelength compared to copper and thus its radiation will not have sufficient energy to cause fluorescence.

8. FUTURE STUDIES

Possible future studies include:

1. Further verification of the PRISM-RS beta version software.
2. Study of the effects of surface preparation on residual stress measured using X-ray diffraction, strain-gage hole drilling, and electronic speckle pattern interferometry (ESPI) hole drilling methods.
3. Study of the effects of using different drilling increments in strain-gage hole drilling and ESPI hole drilling methods on the residual stress profile of a material.
4. Study of the effects of different types of drill bits used in an ESPI system on the residual stress profile of a material.
5. An experimental study to find the optimum drill speed, drill feed rate, and number of drilling increments for ESPI hole drilling method (particularly for steel), in order to obtain the most comparable results to other methods.

REFERENCES

1. Juvinall, R.C. 1967. Engineering Considerations of Stress, Strain, and Strength. McGraw-Hill Book Company, New York.
2. James, M.R., J. Lu. 1996. "Chapter 1: Introduction," Handbook of Measurement of Residual Stresses, The Fairmont Press, Inc., Lilburn, Georgia, pp. 1-4.
3. Fitzpatrick, M.E., A.T. Fry, P. Holdway, F.A. Kandil, J. Shackleton, and L. Suominen. March 2002. *Measurement Good Practice Guide No. 52: Determination of Residual Stresses by X-ray Diffraction*. The National Physical Laboratory, Teddington, Middlesex, United Kingdom.
4. Callister, Jr., William D. 1997. Materials Science and Engineering: An Introduction, 4th Ed. John Wiley & Sons, Inc., New York.
5. Shackelford, James F. 1995. Introduction to Materials Science for Engineers, 4th Ed. Prentice Hall, Upper Saddle River, New Jersey.
6. Hammond, Christopher. 2001. The Basics of Crystallography and Diffraction, 2nd Ed. Oxford University Press Inc., New York.
7. Kandil, F.A., J.D. Lord, A.T. Fry, and P.V. Grant. February 2001. "A Review of Residual Stress Measurement Methods – A Guide to Technique Selection," Project CPM4.5: *Measurement of Residual Stress in Components*. NPL Materials Centre, National Physical Laboratory, Teddington, Middlesex, United Kingdom.

8. Fry, A.T. 22 January 2004. "Residual Stress Measurement." E-mail to Norma Jean Mattei, University of New Orleans.

9. Fry, A.T., F.A. Kandil. July 2002. "A Study of Parameters Affecting the Quality of Residual Stress Measurements Using XRD," *ECRS 6: Proceedings of the 6th European Conference on Residual Stresses.* NPL Materials Centre, National Physical Laboratory, Teddington, Middlesex, United Kingdom.

10. François, M., F. Convert, and S. Branchu. December 2000. "French Round-robin Test of X-ray Stress Determination on a Shot-peened Steel," *Experimental Mechanics,* Vol. 40(4), pp. 361-368.

11. Measurements Group. 1993. "Measurement of Residual Stresses by the Hole Drilling Strain Gage Method," *Measurements Group Tech Note (TN-503-5): Residual Stress Measurement.* Measurements Group, Inc., Raleigh, North Carolina.

12. American Society for Testing and Materials. 1992. "ASTM E837-92: Standard Test Method for Determining Residual Stresses by the Hole-Drililng Strain-Gage Method," *Annual Book of ASTM Standards,* Vol 03, No. 01, pp. 747-753.

13. Schajer, G.S. 1981. "Application of Finite Element Calculations to Residual Stress Measurements," *Journal of Engineering Materials and Technology,* Vol 103, pp. 157-163.

14. Lord, J.D., A.T. Fry, and P.V. Grant. May 2002. "A UK Residual Stress Intercomparison Exercise," Project CPM4.5: *Measurement of Residual*

Stress in Components. NPL Materials Centre, National Physical Laboratory, Teddington, Middlesex, United Kingdom.

15. Lord, J.D., P.V. Grant, A.T. Fry, and F.A. Kandil. July 2002. "A UK Residual Stress Intercomparison Exercise – Development of Measurement Good Practice for the XRD and Hole Drilling Techniques," *ECRS 6: Proceedings of the 6th European Conference on Residual Stresses.* NPL Materials Centre, National Physical Laboratory, Teddington, Middlesex, United Kingdom.

16. Grant, Paul. May 2002. "Evaluation of Residual Stress Measurement Uncertainties using X-Ray Diffraction and Hole Drilling via a UK Intercomparison Exercise," *Measurement Note MATC(MN)020.* NPL Materials Centre, National Physical Laboratory, Teddington, Middlesex, United Kingdom.

17. Lord, Jerry. 12 September 2000. "Hole Drilling Techniques," *Residual Stress in Context. How to Choose a Technique*. BCA Structural Materials Workshop, Manchester Materials Science Centre, University of Manchester and UMIST, Manchester, United Kingdom.

18. Prevey, Paul S. March 1988. "Residual-Stress Distributions Produced by Strain-Gage Surface Preparation," *Experimental Mechanics,* Vol XLV, pp. 92-97.

19. Schajer, G.S., M.T. Flaman, G. Roy, and J. Lu. 1996. "Chapter 2: Hole-Drilling and Ring Core Methods," Handbook of Measurement of Residual Stresses, The Fairmont Press, Inc., Lilburn, Georgia, pp. 5-34.

20. Measurements Group. "Surface Preparation for Strain Gage Bonding," *Measurements Group Instruction Bulletins (B-129).* Measurements Group, Inc., Raleigh, North Carolina.

21. Measurements Group. 1992. "Instruction Manual," *MODEL RS-200 Milling Guide*. Measurements Group, Inc., Raleigh, North Carolina.

22. Sasaki, K., M. Kishida, and T. Itoh. September 1997. "The Accuracy of Residual Stress Measurement by the Hole-drilling Method," *Experimental Mechanics*, Vol. 37(3), pp. 250-257.

23. Roy, G. June 1994. "The Effect of Machining Strains on the Accuracy of Residual Stress Determination by the Hole Drilling Method – SEM Study," *Proceedings of the 1994 SEM Spring Conference on Experimental Mechanics*, pp. 444-448.

24. Gibmeier, J., M. Kornmeier, and B. Scholtes. 2000. "Plastic Deformation during Application of the Hole-Drilling Method," *Material Science Forum – ECRS 5: Fifth European Conference on Residual Stresses*, 28-30 September 1999, Delft-Noordwijkerhout, The Netherlands, Vols. 347-349, pp. 131-136.

25. Nobre, J.P., M. Kornmeier, A.M. Dias, and B. Scholtes. September 2000. "Use of the Hole-Drilling Method for Measuring Residual Stresses in Highly Stressed Shot-peened Surfaces," *Experimental Mechanics*, Vol. 40(3), pp. 289-297.

26. Steinzig, M., and E. Ponslet. May/June 2003. "Residual Stress Measurement Using the Hole Drilling Method and Laser Speckle Interferometry: Part I," *Experimental Techniques: Technology Application Series*, pp. 43-46.

27. Nelson, D.V., and J.T. McCrickerd. December 1986. "Residual-Stress Determination Through Combined Use of Holographic Interferometry and Blind-Hole Drilling," *Experimental Mechanics*, Vol. 26(4), pp. 371-378.

28. Nelson, D.V., A. Makino, and E.A. Fuchs. 1997. "The Holographic-Hole Drilling Method for Residual Stress Determination," *Optics and Lasers in Engineering*, Vol. 27, pp. 3-23.

29. Steinzig, M., G.J. Hayman, and M.B. Prime. 2001. "Verification of a Technique for Holographic Residual Stress Measurement," *Proc. of the ASME Pressure Vessel and Piping Conference*, Atlanta, GA, 2001, ASME PVP-429, pp. 65-70.

30. Ponslet, E. and M. Steinzig. July/August 2003. "Residual Stress Measurement Using the Hole Drilling Method and Laser Speckle Interferometry – Part II: Analysis Technique," *Experimental Techniques: Technology Application Series*, pp. 1-5.

31. Ponslet, E. and M. Steinzig. September/October 2003. "Residual Stress Measurement Using the Hole Drilling Method and Laser Speckle Interferometry – Part III: Analysis Technique," *Experimental Techniques: Technology Application Series*, pp. 45-48.

32. Steinzig, M., and A. Ponchione. August 2002. "Effect of Hole Drilling Parameters on the Accuracy of Residual Stress Measurement for ESPI

Hole Drilling," *2002 BSSM International Conference on Advances in Experimental Mechanics*, 27-29 August 2002, Stratford upon Avon, United Kingdom.

33. Diaz, F.V., G.H. Kaufmann, and G.E. Galizzi. February 2000. "Determination of Residual Stresses using Hole Drilling and Digital Speckle Pattern Interferometry with Automated Data Analysis," *Optics and Lasers in Engineering*, Vol. 33, pp. 39-48.

VITA

Saskia Indah Lestari was born on August 4, 1980 in Tembagapura, Indonesia. She graduated from the Gailer School in Middlebury, Vermont, in June 1998. She then attended the University of New Orleans, where she received her Bachelor of Science degree in Civil Engineering in May 2002. She expects to receive her Master of Science degree in Engineering, with a concentration in Civil Engineering, in May 2004.